

Astronomical Spectroscopy with Electron Multiplying CCDs

Simon Tulloch

Department of Physics & Astronomy

The University of Sheffield

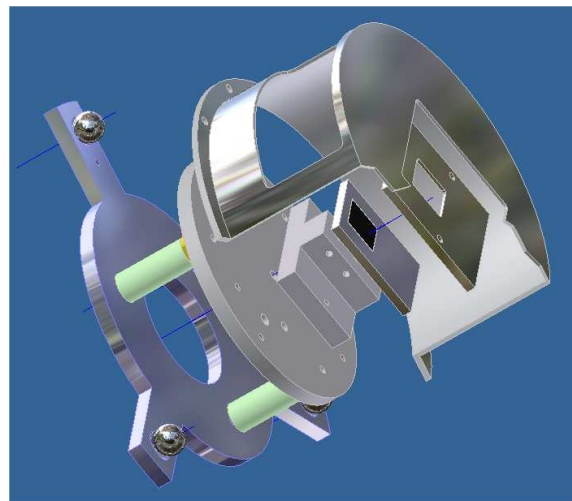
*A dissertation submitted in candidature for the degree of
Doctor of Philosophy of the University of Sheffield*

15th March 2010

Declaration

I declare that no part of this thesis has been accepted, or is currently being submitted, for any degree or diploma or certificate or any other qualification in this University or elsewhere.

This thesis is the result of my own work unless otherwise stated.



Summary

This thesis describes a project to build an electron-multiplying CCD camera for astronomy, starting with its initial conception, design and manufacture and culminating with its use on-sky for a novel astronomical observation. In Chapter 1 some key CCD concepts are introduced and the differences between an EMCCD and a conventional CCD are described. In Chapter 2 the mechanical and electronic design of the camera are described and pictures of its assembly are presented. Chapter 3 describes the initial characterisation and optimisation of the camera's performance immediately prior to its being used on-sky for the first time. In Chapter 4 the camera was then further optimised in order to obtain the very-best noise performance. In Chapter 5 the camera was modeled using a Monte-Carlo technique to predict its performance and the expected performance of future lower-noise cameras. In Chapter 6 the subject of cataclysmic variable (CV) stars is introduced with a description of their evolution. In Chapter 7 an observation of the CV SDSS J143317.78+101123.3 with an EMCCD camera is described. Conclusions and suggestions for future work in the area of EMCCD camera development are presented in Chapter 8.

Acknowledgements

I would like to thank the Isaac Newton Group for giving me the flexibility and resources to pursue this doctorate. Thanks to Kevin Dee for arranging the manufacture of the second QUCAM and for providing some excellent graphics. Derek Ives and Olivier Daigle have been very helpful in providing me with data from their own cameras and for making me feel part of the EMCCD community despite my location here on a small island off the coast of Africa. Thanks to Pablo Rodríguez-Gil for performing the majority of the observations with QUCAM and for teaching me much about binary stars. Thanks to Jure ‘el cerebro’ Skvarc for his expert mathematical advice and Dan Bramich for rescuing me from some statistical difficulties. The analysis of the astronomical data was made much easier thanks to Tom Marsh’s freely available **MOLLY** package. Finally thanks to my supervisor Professor Vik Dhillon for his tremendous enthusiasm in my work, for his financial support and for introducing me to the fascinating and beautiful world of cataclysmic variables.

Contents

I An EMCCD Camera for Spectroscopy	18
1 Introduction	19
1.1 History of CCD development	19
1.2 Key CCD concepts	20
1.2.1 Photoelectric effect	20
1.2.2 Structure of a CCD	21
1.2.3 Quantum efficiency	23
1.2.4 Charge transport	24
1.2.5 Full-well capacity	25
1.2.6 Frame-transfer CCDs	25
1.2.7 Dark current	27
1.2.8 Read-noise	28
1.2.9 Photon noise	29
1.3 Key EMCCD concepts	29
1.3.1 EMCCD structure	29
1.3.2 System gain and multiplication gain	31
1.3.3 Output signal distribution from EM register . .	32

1.3.4	Clock-induced charge	33
1.3.5	Multiplication noise	34
1.3.6	Normal or Conventional mode	36
1.3.7	Proportional or Linear mode	36
1.3.8	Photon counting mode	36
1.4	Underscan and overscan regions	39
1.5	The QUCAM	40
2	Design of the Camera	43
2.1	Mechanical and thermal design of the camera	43
2.2	The camera electronics	47
2.2.1	The camera controller	47
2.2.2	Cabling and head board	49
2.2.3	Generation of the high-voltage clock	50
2.3	Camera control software	51
2.3.1	Embedded controller software	52
3	Initial characterisation of camera	54
3.1	Serial clocking in an EMCCD	54
3.2	Measuring the system gain of an EMCCD	55
3.3	Measurement of quantum efficiency	58
3.4	Measurement of charge transfer efficiency	59
3.4.1	High-level CTE	61

3.4.2	Low-level CTE	62
3.4.3	Ultra low-level CTE	64
3.5	Dark current and operating temperature	65
3.5.1	The transition to non-inverted mode	66
3.5.2	Measurement of ultra-low dark currents	66
3.5.3	The cosmic ray background	68
3.5.4	Settling time after camera reset	68
3.5.5	The manufacturer's dark current model	70
3.5.6	Dark current suppression using 'Dither'	71
3.5.7	Residual image	73
3.6	Charge-handling capacity and dynamic range	75
3.7	Amplifier linearity	78
3.8	Measurement of CIC	79
3.8.1	Inverted mode CIC	79
3.8.2	Non-inverted mode CIC	80
3.9	High and low-level flat fields	80
3.10	Summary of initial setup conditions	81
4	Fine tuning of camera performance	83
4.1	Reduction of the clock induced charge	83
4.1.1	Use of non-inverted mode	84
4.1.2	Tuning of serial clock waveforms	84
4.1.3	Measurement of parallel CIC	91

4.1.4	Tuning of EM register clock waveforms	95
4.1.5	Reduction of EM-register CIC using high gain . .	95
4.2	Confirmation of EM-register charge capacity	98
4.3	Confirmation of system linearity	99
4.4	Photon counting with EMCCDs	100
4.4.1	Optimisation of the PC threshold	101
4.4.2	Summary of the camera noise sources	103
4.5	Final performance of camera	103
4.6	Comparison with other cameras	106
5	Modeling of an EMCCD	109
5.0.1	Basic model of the multiplication process	109
5.0.2	Advanced model of the CCD201 EMCCD	109
5.1	Engineering applications of the model	110
5.1.1	Single-electron CTE	110
5.1.2	Origin of the CIC	111
5.1.3	Effect of imperfect CTE on the CIC	113
5.1.4	Visualisation of multiplication noise	113
5.2	Modeling of PC operation	114
5.2.1	Statistics of photons	115
5.2.2	Statistics of CIC	116
5.2.3	The problem of threshold optimisation	117
5.2.4	Generation of model signal frames	118

5.2.5	Generation of model CIC noise frames	119
5.2.6	Effect of Gaussian read-noise	120
5.2.7	Detected fraction of photoelectrons.	123
5.2.8	Detected fraction of CIC events.	124
5.2.9	Calculating photon-counting SNR	126
5.2.10	Calculating linear-mode SNR	126
5.2.11	Photon-counting performance of QUCAM2 . .	127
5.2.12	Practical photon counting	129
5.2.13	Photon counting: conclusions.	131
II	EMCCD Spectroscopic Observations	135
6	The Nature of Cataclysmic Variables (CVs)	136
6.1	Introduction to CV systems	136
6.2	Origin of CVs	137
6.3	The common envelope phase	137
6.4	Magnetic braking	138
6.5	Mass transfer and the Roche lobe	138
6.6	Emissions of CVs	140
6.7	Orbital evolution and the period gap	141
6.8	Degenerate secondaries and the period bounce	142
6.9	CVs as supernovae progenitors	143
6.10	Magnetic CVs	144
6.11	Eclipsing CVs	144

7	EMCCD observations of SDSS J1433	146
7.1	What is known already about SDSS J1433	147
7.2	Observations and reduction	148
7.2.1	The average spectrum	150
7.2.2	Continuum and H α light curves	151
7.2.3	Trailed spectra and Doppler tomogram	151
7.2.4	The diagnostic diagram	154
7.2.5	The light centre method	156
7.2.6	Eclipse phase as a function of accretion disc radial velocity	157
7.3	Conclusions drawn from observations	158
7.4	The SNR advantage gained by use of an EMCCD . . .	159
8	Conclusions and future work	161
Appendices		169

List of Figures

1.1	Photoelectric effect	21
1.2	CCD analogy	22
1.3	Structure of CCD	23
1.4	CCD blooming	25
1.5	Geometry of frame transfer CCD	26
1.6	Frame transfer CCD	26
1.7	Potential gradients within a CCD	27
1.8	CCD201-20 format.	30
1.9	Serial-clock geometry of an EMCCD.	30
1.10	Output of EM register	33
1.11	Appearance of clock induced charge	34
1.12	Excess noise	35
1.13	Basic SNR graph	37
1.14	Photon counting	37
1.15	Photon counting demonstration	39
1.16	Underscan and overscan regions	40
2.1	The empty cryostat	44

2.2	Camera components ready for assembly	45
2.3	The ‘spider’ and the thermal braids.	46
2.4	Camera baseplate	47
2.5	The detector and its PCB	48
2.6	Radiation shield	48
2.7	Camera cool-down.	49
2.8	High-voltage clock board	50
3.1	Serial-clock phasing in an EMCCD	55
3.2	Gain calculation histogram	57
3.3	The temperature dependance of EM gain	58
3.4	The quantum efficiency measurement rig.	59
3.5	Quantum efficiency plots.	60
3.6	The Fe ⁵⁵ X-ray source mounted on the camera.	61
3.7	Horizontal CTE as measured using Fe ⁵⁵ X-rays.	62
3.8	Spot-image profiles using the normal output	63
3.9	Autocorrelation of single-electron events	66
3.10	Measurement of the inversion point	67
3.11	Cosmic-ray image	69
3.12	Dark current after reset	69
3.13	Inverted and non-inverted dark current	71
3.14	Non-inverted mode dark current	72
3.15	Inverted-mode dark current	73

3.16 Remnance dark current	74
3.17 Non-inverted full well	76
3.18 Inverted-mode blooming	76
3.19 Non-inverted mode blooming	76
3.20 Spot profiles	77
3.21 Horizontal blooming	78
3.22 Linearity of the normal output.	78
3.23 Flat fields	81
4.1 Parallel clock phases in inverted mode.	85
4.2 Parallel clock phases in non-inverted mode.	86
4.3 Effect of dump gate on CIC distribution.	87
4.4 Use of the dump gate to measure serial generated CIC	88
4.5 Optimised serial-clock waveforms: zoomed in view . . .	90
4.6 Optimised serial-clock waveforms over 3 pixel periods .	91
4.7 Use of the dump gate to measure serial-generated CIC	92
4.8 Monitoring of CTE using image autocorrelation	93
4.9 Parallel CIC visible in inverted mode.	94
4.10 Parallel CIC in non-inverted mode.	95
4.11 High gain to reduce effective CIC	97
4.12 Rechecking of EM register capacity	99
4.13 Post-optimisation normal-output linearity	100
4.14 Post-optimisation EM output linearity	100

4.15	Detected fraction of photons versus threshold	104
4.16	Noise versus photon-counting threshold	104
4.17	SNR gains using photon counting	105
4.18	The University of Montréal EMCCD camera	107
5.1	Modeling of the CIC	112
5.2	Fitting the CIC model to the real data	112
5.3	Growth of charge packets within the EM register	114
5.4	Poisson distribution	115
5.5	Binomial distribution	116
5.6	Cumulative distribution function C_P of photoelectrons	119
5.7	Cumulative distribution function C_C of CIC	120
5.8	Read-noise in photon-counting mode.	122
5.9	False triggers from read-noise	123
5.10	Detected fraction of photons	124
5.11	Detected fraction of CIC	125
5.12	Photon-counting SNR	128
5.13	Optimum PC threshold	129
5.14	PC SNR with large blocking factors versus an ideal detector	132
5.15	PC SNR with large blocking factors versus an EMCCD in linear mode	133
5.16	PC SNR with large blocking factors versus a conven- tional CCD	134

6.1	Artists impression of a CV	137
6.2	The Roche lobe	139
6.3	The 1 st Lagrangian point.	140
6.4	The period gap	142
6.5	The accretion disc	145
7.1	Spectrum of SDSS J1433	148
7.2	SDSS J1433 finding chart	148
7.3	QUCAM2 mounted on the telescope	149
7.4	The average spectrum of SDSSJ1433	151
7.5	Eclipse light curves	152
7.6	Trailed spectrum and Doppler map	153
7.7	Diagnostic diagram	155
7.8	Light centre diagram	157
7.9	Radial velocity curve	158
7.10	Eclipse phase	159
7.11	The SNR advantage from using an EMCCD	160

Symbols used in thesis

M	Mean photo-charge per pixel
n	Actual pixel charge
g_A	EM, avalanche or multiplication gain
g_S	gain or system gain (e^-/ADU)
g_{S0}	system gain through EM amplifier in absence of EM gain
N	Stages in EM register
ν_{CS}	Mean per-pixel CIC charge originating in serial register
ν_{CEM}	Mean per-pixel CIC charge originating in EM register
ν_C	Mean per-pixel CIC charge in total
B_C	Mean number of in-EM-register CIC events in a pixel
p_{CS}	Probability of CIC generation per transfer in the serial register
p_{CEM}	Probability of CIC generation per transfer in the EM register
\bar{q}_I	Mean effective charge of a CIC electron originating in the EM register
p	Probability of multiplication gain per stage of the EM register
q_O	Instantaneous size of a charge packet within the EM register
P_d	Probability of detection of a single photoelectron when photon-counting
σ	Gaussian read-noise e^- (RMS)
T	Photon-counting threshold, referenced to the output of the EM register
t	Photon-counting threshold, referenced to the input of the EM register
C_P	Fraction of pixels containing n photoelectrons that lie above threshold t
C_C	Fraction of pixels containing n CIC electrons that lie above threshold t
C_G	Fraction of pixels containing only read-noise that lie above threshold t
F_P	Detected fraction of photoelectrons as a function of M and t
F_C	Detected fraction of in-EM-register CIC electrons as function of B_C and t
D	Photon-counted frames that are added together to produce an analysable image
SNR_{PC}	Signal-to-noise ratio of a pixel in an EMCCD operated in photon-counting mode
SNR_L	Signal-to-noise ratio of a pixel in an EMCCD operated in linear mode
SNR_N	Signal-to-noise ratio of a pixel in a conventional CCD
SNR_{IDEAL}	Signal-to-noise ratio of a pixel in an ideal imaging system

Φ	Total potential of a test particle
a	Separation of the stars in a CV system
P_{orb}	Orbital period of the stars in a CV system
K_W	Radial velocity semi-amplitude of the white dwarf in a CV system
γ	Systemic velocity of a CV system
M_1	Mass of the primary in a CV system
M_2	Mass of the secondary in a CV system
M_\odot	Mass of the sun
R_\odot	Radius of the sun

Part I

An EMCCD Camera for Spectroscopy

Chapter 1

Introduction

In this chapter the key concepts of charge coupled device (CCD) design are introduced together with a historical perspective of astronomical detector development. The differences between conventional and electron multiplying charge coupled devices (EMCCDs) are then described.

1.1 History of CCD development

Up until the 1970s astronomical images were recorded on photographic plates. In the absence of alternatives astronomers had to content themselves with throwing away up to 95% of the photons collected by their telescopes, the maximum quantum efficiency (QE) of a photographic plate being in the region of 5%. The detector revolution began in 1970 in Bell labs where W. Boyle and G. Smith invented the charge coupled device (Boyle & Smith 1970). For this they were awarded the Nobel prize for physics in 2009. It was initially conceived of as a memory storage device but its potential as an imager was quickly recognised. The technology has matured incredibly quickly, driven mainly by the needs of the military and consumer camera market. Now, less than 40 years since their invention, CCDs are approaching the theoretical limits of their performance. QEs of greater than 90% are now easily obtained, meaning that a 1m diameter telescope with a CCD can perform more or less the same science as a 4m telescope equipped with only a chemical-emulsion camera.

In terms of detection threshold a CCD camera is limited by the electronic noise in its readout amplifier. For a conventional CCD this has now reached approximately $2e^-$ root mean square (RMS), not quite enough to resolve a single photon but still impressively and surprisingly low. CCDs have also grown steadily larger during their

development. The first astronomical CCD measured 100x100 pixels. The current record is now held by Semiconductor Technology Associates who have manufactured a 111 Megapixel device, the worlds largest integrated circuit (Zacharias et al. 2007). In 2001 a new type of detector was announced: the electron multiplying CCD or EMCCD. This was first described by Jerram et al. (2001) at E2V Technologies and Hynecek (2001) at Texas Instruments. These devices incorporate an avalanche gain mechanism that renders the electronic noise in their readout amplifiers negligible and permits the detection of single photoelectrons. Whilst this has been possible for some time with image tube detectors such as the IPCS (Boksenberg & Burgess 1972, Jenkins 1987), this technology has never been available with the pixel count, convenience of use, relatively low cost and high quantum efficiency of a CCD. The EMCCD thus combines many useful properties that are sought by astronomers working in photon-starved regimes and whilst currently somewhat under-exploited they have the promise to make a large contribution to astronomy in the near future. In this thesis the application to the study of short-period variable stars (see Chapter 7) has already been demonstrated.

1.2 Key CCD concepts

1.2.1 Photoelectric effect

The photoelectric effect lies at the heart of CCD operation. To understand it one has to consider the energy bands in the silicon from which the CCD is constructed. Atoms normally have narrow, discrete energy levels at which electrons are stable. In crystalline solids such as silicon these levels are smeared out into wider bands due to the perturbing influence of each atom on its neighbours. Most electrons are to be found in the so-called valence band where they are bound to a specific silicon atom and unable to move around. A small fraction of electrons are to be found, however, in the conduction band situated above the valence band. The separation of these two bands is known as the band-gap. These electrons have absorbed sufficient energy, either from an incident photon or from thermal excitation, to reach the conduction band from where they are then free to move throughout the silicon and contribute to its conductivity. The band-gap in silicon is approximately 1.26eV so any photon with an energy more than this will be able to excite a valence electron into the conduction band (see Figure 1.1). Below this energy, which corresponds to that of a $1\mu\text{m}$ infra-red photon, the silicon becomes transparent since the photons are unable to interact with the electrons through the photoelectric effect. It is a lucky coincidence that silicon, so readily usable for the manufacture of micro-electronic

devices, has a band-gap so nicely matched to the energy of photons in the visible part of the spectrum.

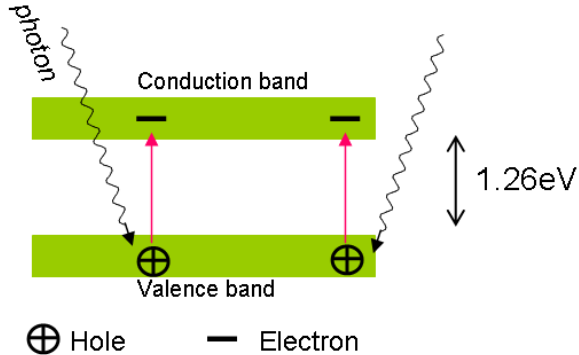


Figure 1.1: The photoelectric effect. The band-gap of the silicon is 1.26eV, approximately equal to the energy of a near-infrared photon. An electron excited into the conduction band leaves a hole in the valence band. Both are then free to move throughout the silicon and contribute to its conductivity.

1.2.2 Structure of a CCD

There is a useful analogy (see Figure 1.2) that can be used to describe how a CCD works. One can imagine a series of parallel conveyor belts arranged in columns on which are placed a series of buckets. With the conveyor belts stationary the buckets are exposed to a shower of rain. At the end of the exposure the conveyor belts then start up, transferring the collected rain towards a single measuring cylinder where the contents of each bucket is recorded. Each bucket corresponds to a pixel in this model, the measuring cylinder is the output amplifier and the rain corresponds to photons (or rather the photoelectrons that they generate). So collected charge packets are transported physically through a CCD device during readout.

Figure 1.3 shows how the geometry introduced using the analogy of a conveyor belt is actually implemented in the silicon. This figure considers only the imaging area of the CCD, also known as the parallel area, where the photoelectrons are collected. In cross-section the CCD consists of two layers of silicon one of n-type and the other of p-type. This constitutes a p-n diode and therefore has an intrinsic electric field perpendicular to the junction between the layers. On top of the silicon is deposited an insulating layer of SiO_2 and above this are deposited a series of transparent electrodes formed of polysilicon. These electrodes are generally grouped into three alternating sets known as ‘phases’ and termed ϕ_1 , ϕ_2 etc. During integration of the image, one of these phases is held at a low voltage whereas the other two are held high. This induces an electric field in the underlying silicon that defines a series of

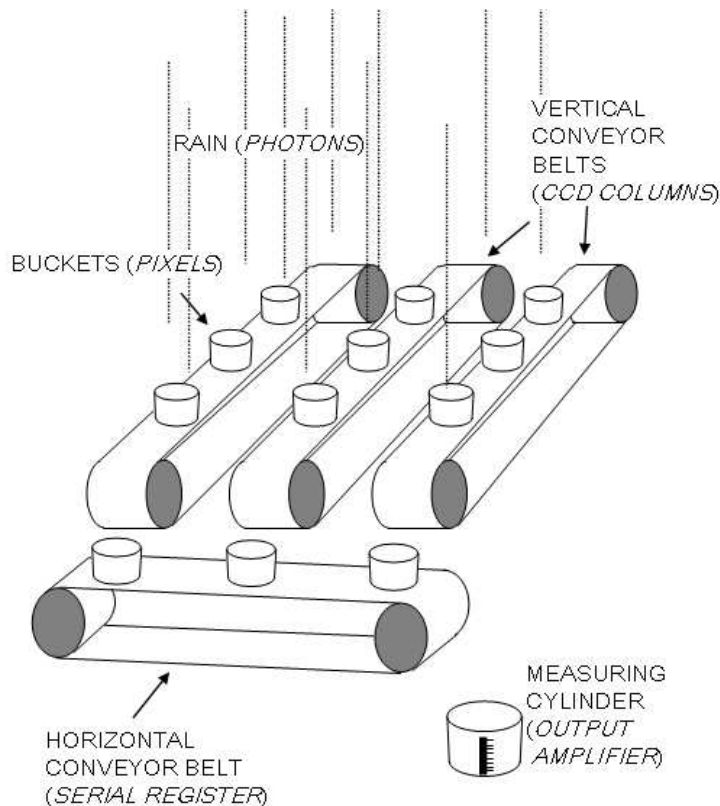


Figure 1.2: A CCD analogy. Here the rain drops are analogous to photons, the buckets can be considered as pixels and the measuring cylinder corresponds to the readout amplifier. Once the rain stops (i.e. the shutter closes) the conveyor belts starts up and transports the collected charge to the output amplifier one pixel at a time.

potential wells into which photoelectrons are attracted. Each potential well then constitutes a picture element or ‘pixel’. Note that the electrodes only define the extent of each pixel in the axis parallel to the pixel columns. Pixels have to be defined in the orthogonal axis by an additional structure in the silicon known as a channel stop.

The above is only an approximate description and there are several variants on this theme. For example, some CCDs have 2 or 4 parallel phases whereas others function with all phases held low during integration. The CCD201-20¹ that was investigated in this thesis is of 2 phase design whereas another E2V device the CCD42-90² is of 3 phase design.

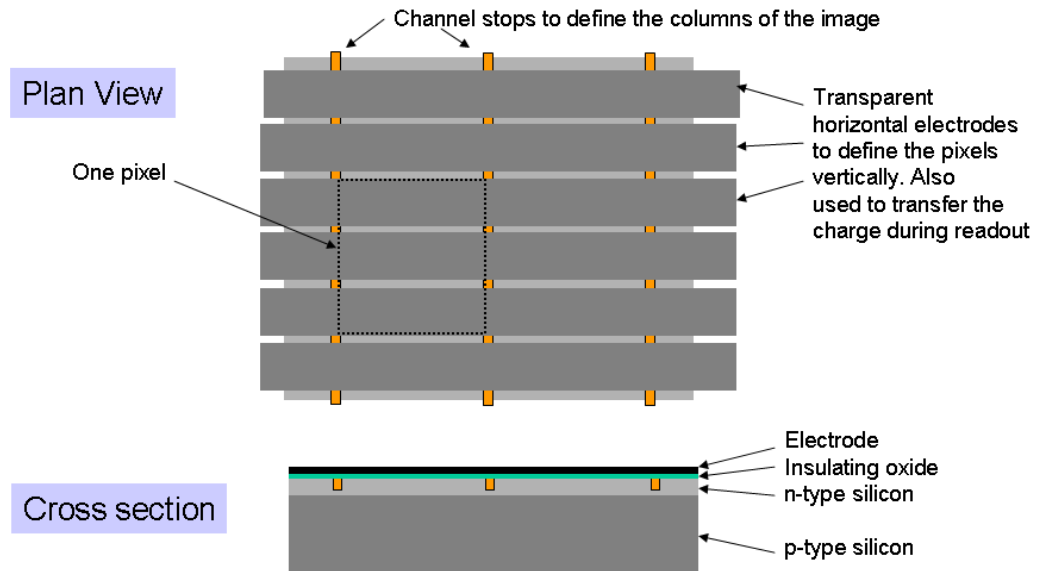


Figure 1.3: Structure of a CCD. A small part of the imaging area is shown. Pixels are defined horizontally by the channel stops and vertically by the potential wells induced by the voltages on the electrodes.

1.2.3 Quantum efficiency

The QE is one of the most important parameters that describe a CCD. It shows what fraction of the incident photons produce a measured photoelectron in the device. QEs in excess of 95% are possible. Silicon has a refractive index of almost 4, which requires the use of an anti-reflective (AR) coating to avoid most photons simply being lost through reflection at the surface of the CCD. Since AR coatings have to be tuned to a certain wavelength it is usual to optimise them either for the red or

¹E2V CCD201 data sheet http://www.e2v.com/assets/media/files/documents/imaging-space-and-scientific-sensors/A1A-100013_2.v1.pdf

²E2V CCD4290 data sheet <http://www.e2v.com/assets/media/files/documents/imaging-space-and-scientific-sensors/13-42-90-BI-NIMO-ButtablePkg.pdf>

blue ends of the spectrum. Broader-band coatings are available but they tend to have a lower peak efficiency. Other losses in QE can occur through ‘recombination’. When a photoelectron is generated it leaves behind a hole in the valence band. If this electron-hole pair is not rapidly separated, for example by an electric field, it will tend to recombine and be lost. It is therefore important to ensure that there are no field-free regions within a pixel that might permit this to happen. This is normally done by thinning the CCD during manufacture using an etching process (Janesick 2001). Additionally the CCD is packaged in such a way that the light enters the device from the surface opposite to the electrode structure. This allows not only a clearer path for the photons (no electrode structure to traverse) but offers a better substrate on which to deposit the AR coating. A CCD processed in this way is known as a thinned backside-illuminated CCD and is the norm for astronomical applications. QE curves for the CCD201-20, a thinned backside-illuminated CCD investigated in some depth in this thesis, are shown in Figure 3.5.

1.2.4 Charge transport

The same structures that are used to collect the photo-charge during integration are also used to transport that charge to the output amplifier at the start of readout. The electrons will always seek the region of lowest potential energy (highest +ve electrical potential). They are therefore attracted to the region beneath the most +ve electrode. By alternating the voltages on the electrode phases in a precise sequence it is possible to push the photoelectrons through the CCD. By decreasing the voltage on the phase under which the photo-charge is stored, and at the same time (with a small overlap), increasing the voltage on the adjacent phase, we move the charge by one step. This is the implementation of the conveyor belt shown in Figure 1.2. This can be repeated as many times as necessary until the charge reaches the output amplifier where it is measured. During the transfer of charge from one phase to its neighbour the voltage on the third phase must be held low so as to maintain the potential barrier between adjacent pixels. A serial transfer is illustrated in Figure 1.9.

Charge transport is typically very efficient with 0.999999 of the photo-charge being transferred at each stage. This fraction is known as the ‘charge transfer efficiency’ or CTE and is another important CCD parameter. The amount of charge not transferred (known as the ‘deferred charge’) can increase, however, if the clock voltages are not properly optimised. This can give rise to trailed images where stars appear elongated in the direction of charge transfer.

1.2.5 Full-well capacity

There is a limit to how much photo-charge a pixel can contain. If this limit, known as the ‘full-well’, is exceeded then any additional charge leaks into neighbouring pixels. Since the channel stops provide a very effective isolation between pixels in adjacent columns, this charge leaks out preferentially along the columns as the potential barrier between pixels is lower along this axis. The result is that overexposed stars appear to have bright streaks extending above and below them. The general term for this effect is ‘blooming’ and it is illustrated in Figure 1.4.



Figure 1.4: CCD blooming. When a pixel becomes saturated, additional photo-charge will then spill out into neighbouring pixels. Image courtesy of Nik Szymanek.

1.2.6 Frame-transfer CCDs

A frame-transfer (FT) CCD has its parallel-clock area sub-divided into two equal parts that can be independently clocked. One of these areas has an opaque aluminium layer deposited on its surface that renders it insensitive to light. This insensitive area can then be used as a temporary frame store and is termed the ‘store area’. This is shown schematically in Figure 1.5. Sacrificing 50% of the area of the CCD in this way may seem somewhat wasteful (with CCD real-estate costing approximately $4k\text{€ cm}^{-2}$) but it permits much higher observing efficiencies in fast frame-rate applications.

Normal astronomical CCDs are used in conjunction with a mechanical shutter that typically operates in a few tens of milliseconds. To avoid image smear the shutter must be closed prior to the commencement of readout. Whilst shut, the CCD is

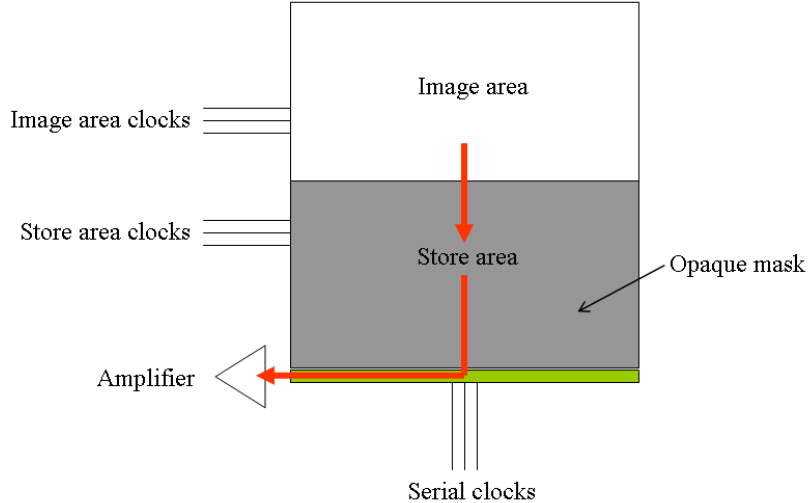


Figure 1.5: Geometry of a frame transfer CCD. The image and store areas have independent clocks.

clearly blind and photons are wasted. Another drawback is that mechanical shutters are not fully reliable, especially if operated repeatedly at high frequency. CCDs intended for TV rate applications (25Hz) will be of FT design. At the end of one exposure the image is rapidly transferred under the opaque shield of the store area. This can be an extremely rapid process, just a few milliseconds. Once in the store, the image can then be read out concurrently with the integration of the subsequent frame. The CCD is therefore almost continuously exposing and gains are made not just in efficiency but also in reliability (due to the absence of a mechanical shutter). Almost all EMCCDs are of this design, one of which (CCD201-20) is shown in Figure 1.6.

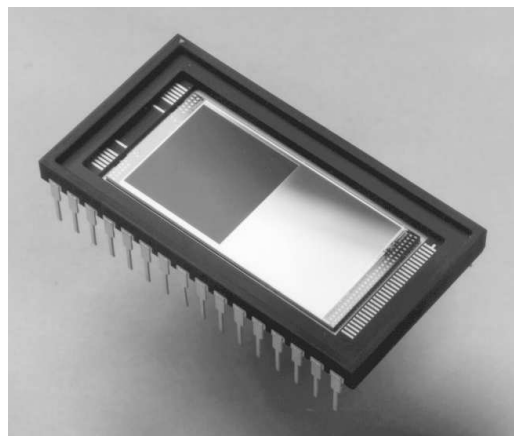


Figure 1.6: A frame transfer CCD. The image area is visible as a dark square offset from the centre of the device. The store area is immediately adjacent and of equal size but hidden under the aluminium light shield. This image is from the E2V web page.

1.2.7 Dark current

As described in Section 1.2.1, electron-hole pairs are generated in a CCD when a photon is absorbed. The photon provides the energy required to excite an electron from the valence into the conduction band where it has a good chance of being collected in the potential well of a pixel. This energy can, however, also be provided by the thermal motion of the atoms in the CCD material. At room temperature these thermally generated electrons, which constitute a ‘dark current’, can saturate a CCD pixel in a second or so. For optimum noise performance it is therefore necessary to cool the CCD to around -100°C . The CCD201 used in this study was intended for higher temperature (around -40°C) Peltier-cooled operation. In this regime special measures have to be taken to ensure low dark current. One of these is to design the device for ‘inverted mode’ operation. Here, the parallel clock phases (those present in the image and store areas) are all maintained in their low states during image integration. This is in contrast to the non-inverted mode, used by most cryogenically-cooled detectors, where one of the parallel phases is maintained in the high state so as to provide a potential barrier between adjacent pixels. Figure 1.7

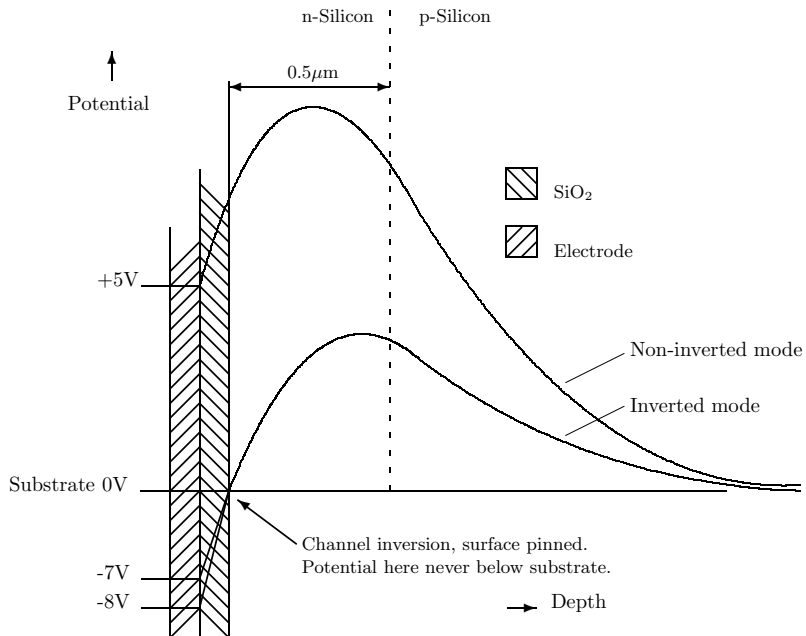


Figure 1.7: Potential gradients within a CCD when both inverted and non-inverted.

shows a cross-section through the image area of a CCD and indicates the electrical potential through the device in each of these modes. In both cases the electric fields generated by the externally applied electrode potential and the intrinsic field generated by carrier diffusion across the p-n junction maintain a potential maximum within which the photo-charge accumulates. As the externally applied electrode voltage is reduced the potential at the surface of the CCD, i.e. the interface between the silicon and the SiO₂ insulating layer that underlies the electrodes, also falls and

the device approaches ever more closely its inversion point. At inversion this surface potential becomes equal to that of the substrate and an interesting phenomenon occurs. Holes flow out from the channel stops (which define the columns of the CCD) and populate the surface region. Any further reduction of electrode potential then has no further effect on the potential of this interface: it becomes locked, or ‘pinned’, to the substrate potential. These holes have an important effect on the dark current of the device. The major dark current contribution comes from mid-band interface states ³ at the surface and these holes effectively mop-up this charge greatly reducing the dark current. For this reason inverted mode operation is preferred for Peltier cooled devices with their higher operational temperature compared to cryogenically cooled devices.

1.2.8 Read-noise

This is what limits the performance of a conventional CCD at the low-signal end of its dynamic range. The on-chip output amplifier of a CCD consists of at least two metal-oxide-semiconductor field effect transistors (MOSFETS). One of these acts as a buffer amplifier transforming the pixel charge, stored on a capacitive measuring node, into a voltage. Once the measurement is performed this node is then reset through the second transistor. Both transistors contribute noise but through clever processing of the video signal it is possible to remove almost entirely that produced by the reset transistor. The noise on the buffer amplifier, however, is much more problematic. It consists of Johnson noise which originates in the thermal motion of the electrons in the channel of the transistor. It has a white (i.e. flat) noise spectrum and its effects can only be removed by reducing the measurement bandwidth or by extreme cooling. Reducing the measurement bandwidth means increasing the time taken to readout the CCD image so there is an inevitable trade-off to be made. Fast readout inevitably means high read-noise. For example, operating a CCD at 10 Mpix s^{-1} may incur a read-noise of 50e^- RMS, whereas to reach $2-3\text{e}^-$ read-noise may require readout at around 50 kpix s^{-1} . One further noise source caused by thermally induced variations in the carrier concentration in the FET channel, known as ‘flicker noise’, imposes an ultimate noise floor. The spectrum of flicker noise has a 1/frequency distribution so further reductions in readout speed can, whilst reducing the Johnson component, actually increase the total read-noise.

³Mid-band interface states are defects in the crystalline structure of the silicon. These are found at the interface between the silicon and the SiO_2 insulating layer. The exact periodicity of the silicon crystal is disturbed in these regions and the band gap is modified. This can make it easier for an electron to jump into the conduction band.

1.2.9 Photon noise

The arrival of photons in a detector is described by Poissonian statistics (see Section 5.2.1). The Poissonian distribution has the property that its variance is equal to its mean. What this means is that the number of observed photons fluctuates about its mean M with a standard deviation \sqrt{M} . So, if we detect 100 photons from a faint astronomical object, the noise in our photometry will be 10 photons; we are unable to decide on its true brightness to any better than 10% accuracy. This is one consequence of the discrete nature of photons and the random way in which they are generated in astronomical sources.

1.3 Key EMCCD concepts

EMCCDs have an effective read-noise that is so low as to be negligible. The QU-CAM2 camera described in this thesis has a read-noise of 0.025e^- and could have been made much lower if necessary. The output MOSFET amplifier of an EMCCD is, however, actually quite noisy: 2 or 3 times that of a conventional CCD. The reason that EMCCDs manage to achieve such low noise is that the photo-charge of each pixel is hugely amplified prior to being measured by this amplifier. A single photoelectron may have been amplified to 1000e^- prior to being measured. In that case the *effective* noise of the amplifier is reduced by a factor of 1000.

1.3.1 EMCCD structure

The structure of an EMCCD is actually very similar to that of a conventional CCD in terms of how the photo-charge is collected and transported. It is when the photo-charge arrives at the serial register that the main difference appears. In an EMCCD the serial register is greatly extended to include extra stages in which the multiplication gain occurs. These extra stages are known as the ‘EM register’. This register is connected to the same serial clock phases $\phi\text{H}1$ and $\phi\text{H}3$ as drive the conventional part of the serial register. The EM register, however, shown as a shaded section in Figure 1.8. contains in place of $\phi\text{H}2$ an extra serial phase known as $\text{R}\phi\text{2HV}$. Additionally there is an extra DC phase, called $\text{R}\phi\text{DC}$ inserted between $\phi\text{H}1$ and $\text{R}\phi\text{2HV}$. This is shown in Figure 1.9. In the course of the readout, photo-charge transfers from $\phi\text{H}1$, passing through the small potential step produced by $\text{R}\phi\text{DC}$ and then falls into the deep potential well beneath $\text{R}\phi\text{2HV}$. In doing so it gains considerable energy and has a small probability of generating additional electrons through impact ionisation. This probability rises steeply with the voltage on $\text{R}\phi\text{2HV}$.

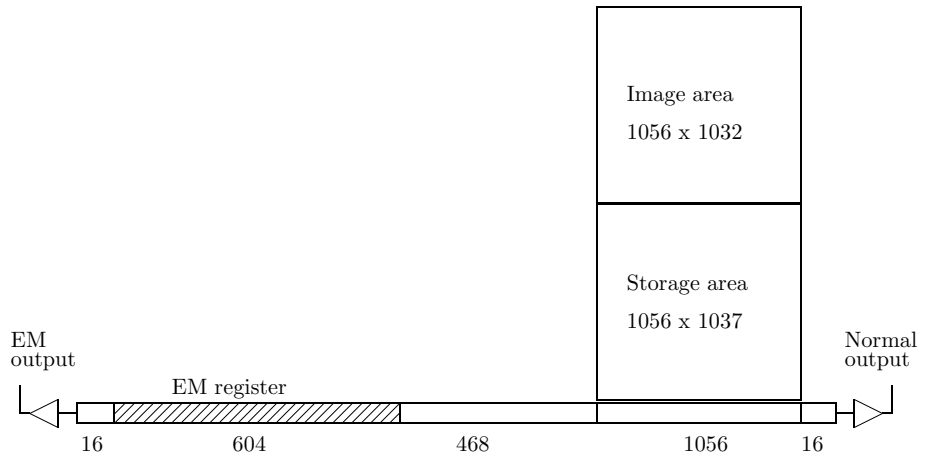


Figure 1.8: CCD201-20 format. In the case of this EMCCD, the EM register takes the form of an extended serial register which contains 604 stages.

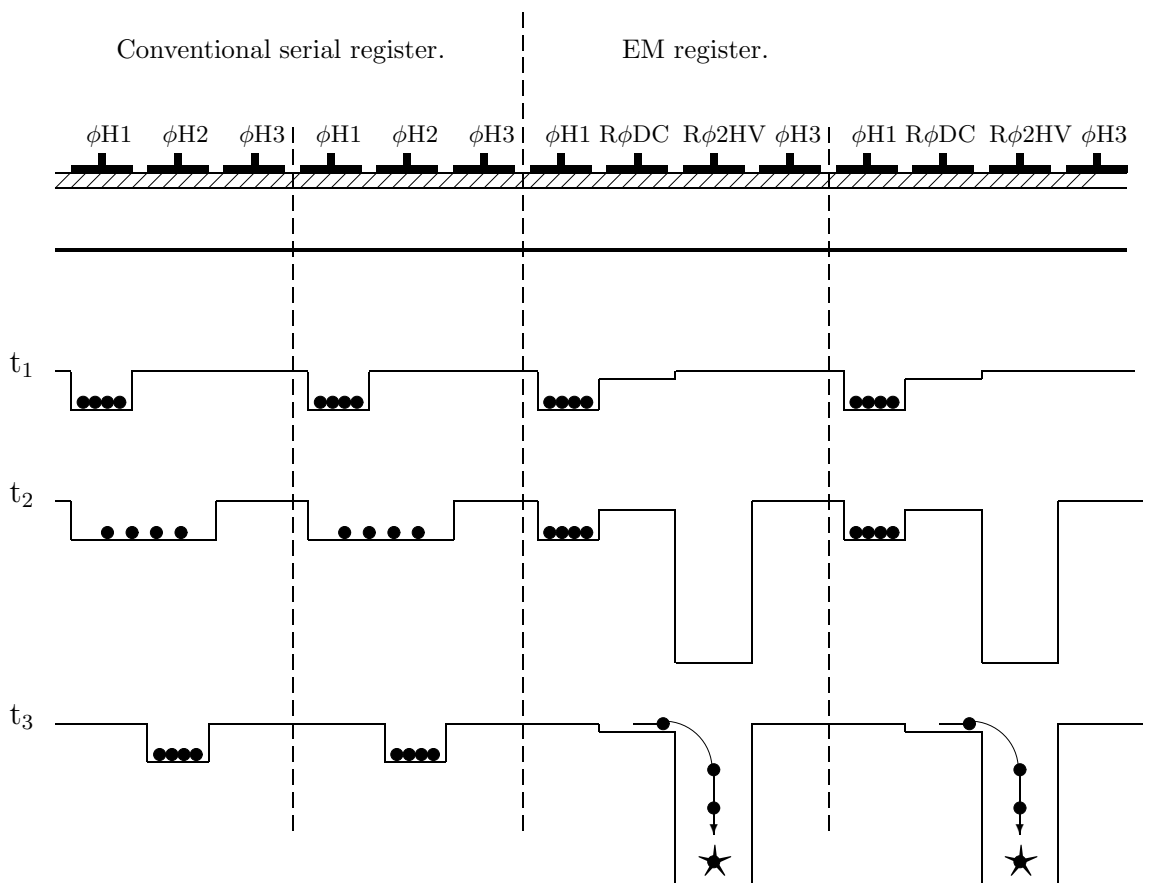


Figure 1.9: Serial-clock geometry of an EMCCD. Four consecutive register elements are shown straddling the join between the EM register and conventional part of the serial register. The graphs indicate the potential wells lying beneath the electrodes in which the photo-charge sits. Three consecutive clock states are displayed (t_1, t_2, t_3). Multiplication occurs when the voltage on $\phi H1$ goes low and the charge falls into the deep potential well under $R\phi 2HV$. At the very end of the serial register, separating it from the output amplifier, is one additional electrode called the output gate (OG). The $R\phi DC$ electrode is not clocked but instead held at constant bias voltage. See Section 1.3.1 for a more detailed explanation.

1.3.2 System gain and multiplication gain

The raw output of the CCD consists of a low level video waveform (i.e. a waveform with a multi-MHz bandwidth) that first needs to be boosted in amplitude using a video amplifier within the controller. This amplifier forms part of a circuit block known as the video processor and is typically located on its own circuit board so as to improve its noise performance. The video processor also contains an important element called a correlated double sampler (CDS) that allows lower read-noise to be achieved through a complex waveform sampling technique. Astronomers typically refer to gain (or strictly speaking system gain) of a CCD camera as meaning the number of photoelectrons represented by 1 analogue-to-digital unit (ADU) in the raw image and therefore it has units of e^-/ADU . This can be somewhat confusing since if the numerical gain of the video amplifier of the CCD in the camera controller is increased, the e^-/ADU in the output image actually *decreases*. However, the use of e^-/ADU units is so ingrained (even amongst CCD engineers who should know better!) that it was thought best to stay with this convention in this thesis. The system gain (units of e^-/ADU) is from now on given the symbol g_S .

System gain has to be well chosen so that at the low-signal end of the camera's dynamic range the size of a single ADU is small compared to the read-noise. Typically the gain is adjusted such that the read-noise is around 3 ADU. This prevents the quantisation noise of the analogue-to-digital converter (ADC) from degrading the signal-to-noise ratio (SNR) of the system. In a well designed camera the upper end of the dynamic range, ultimately limited by the range of the ADC, should then match the range of illumination over which the CCD will be linear before blooming sets in. A typical value for the gain would be $1e^-/\text{ADU}$ for a CCD with $3e^-$ read-noise. With a 16-bit ADC, which is the standard, the upper end of the dynamic range would then be $65535 e^-$, i.e. $2^{16} - 1$. This is rather less than the blooming limit of most scientific CCDs. In order to be able to extend the camera operation to the high-signal regime most systems therefore allow switchable gain: low gain for faint objects and high gain for brighter objects. Most video processors contain an integrator. Conveniently, these give more e^-/ADU if they are operated at higher speeds. They also give more noise. The gain switch mechanism therefore normally just involves changing the integrator speed: the faster the integration the higher the gain in e^-/ADU and the higher the read-noise. The overall effect is that the image noise measured in ADU stays reasonably constant. Since the higher gains are generally used for measuring bright signals, the fact that they are noisier is of little consequence: the images will be photon-noise dominated anyway.

An EMCCD camera has yet another gain parameter that we need to describe; that of the avalanche multiplication gain factor g_A , (also referred to as the EM gain) and

there is a risk of confusion here with the system gain g_S . g_A is simply a unitless multiplication factor equal to the mean number of electrons that exit the multiplication register in response to a single electron input.

If we measure the system gain of an EM camera (see Sections 3.2, 3.4.1) then the value we arrive at will be a combination of gain in the video processor and gain in the EM register. Our measurement of g_S will not tell us directly what g_A is. It is clearly important to separate out these two factors. Generally the gain of the video processor is quite a stable parameter provided we do not make changes to the integrator speed. Conversely the EM multiplication gain can be quite volatile and freely variable by the user. In order to measure g_A (clearly a key parameter in the performance of the camera) we therefore need to first turn off the EM gain by reducing the HV clock amplitude to 20V. At this level the EM register will then behave as a conventional register i.e. 1 electron in, 1 electron out. We now measure the system gain (there are various methods, see Section 3.4.1 for one of these) of the EM output and assign it the symbol g_{S0} . The units will be e^-/ADU . As long as we do not make any subsequent changes to the operation of the video processor, g_{S0} will be a constant parameter that will allow us to calculate the EM gain g_A from a measure of the system gain g_S . The relationship is simply $g_A = g_{S0}/g_S$. So in summary :

- g_S : gain or system gain (e^-/ADU)
- g_A : avalanche, multiplication or EM gain (unitless)
- g_{S0} : system gain of EM amplifier with EM gain=1 (e^-/ADU)

1.3.3 Output signal distribution from EM register

This has been studied in some depth by Tubbs (2003). He obtained the following result, showing that the probability of an output signal of n electrons resulting from a single input electron traversing the EM gain register with overall gain g_A was :

$$P(n) \begin{cases} = \left(\exp\left(\frac{1}{g_A - 1/2}\right) - 1 \right) \exp\left(-\frac{n}{g_A - 1/2}\right) & \text{if } n \geq 1 \\ = 0 & \text{otherwise.} \end{cases} \quad (1.1)$$

As long as $g_A \gg 1$, then for the case of a single electron input we can approximate the output signal distribution by :

$$P(n) \begin{cases} = \frac{1}{g} \exp\left(-\frac{n}{g}\right) & \text{if } n \geq 1 \\ = 0 & \text{otherwise.} \end{cases} \quad (1.2)$$

If we plot a histogram of pixel values from a faintly illuminated EMCCD it should therefore have this form. Conveniently, if we plot the natural logarithm of the number of pixels in each histogram bin along the ordinate, the histogram will then have a large linear region whose gradient is equal to $-1 \times$ the system gain g_S in e^-/ADU . This useful property was exploited as a simple method of measuring the system gain during the optimisation of the camera (see Chapter 3 for further details).

Tubbs (2003) then extends his equation to a more general form to show the probability of an output signal n arising from an input of m electrons to the EM register :

$$P(n, m) \begin{cases} = \frac{(n - m + 1)^{m-1}}{(m - 1)! (g_A - 1 + \frac{1}{m})^m} \exp\left(-\frac{n - m + 1}{g_A - 1 + \frac{1}{m}}\right) & \text{if } n \geq m \\ = 0 & \text{otherwise.} \end{cases} \quad (1.3)$$

This relation is illustrated graphically in Figure 1.10 for inputs of 1, 2, 3, 4 and $5e^-$ to the EM register.

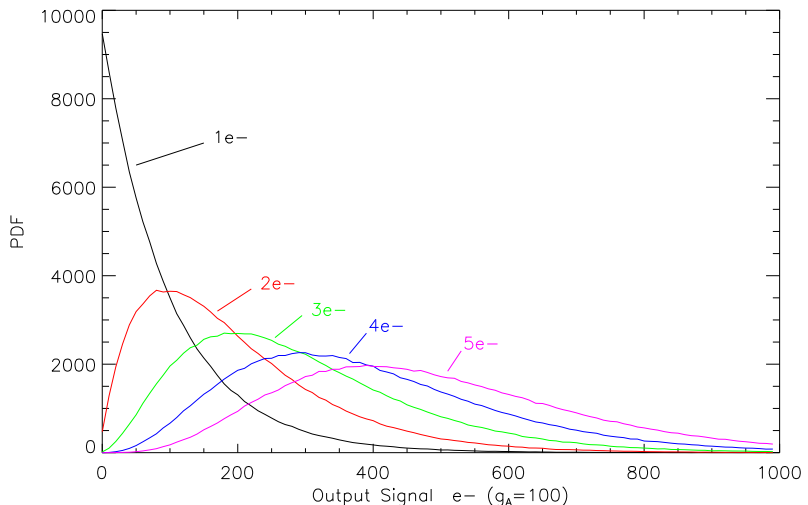


Figure 1.10: Output of EM register with $g_A = 100$ in response to a range of inputs from 1 to $5e^-$. The y -axis shows the probability density function (PDF) of the output signal, i.e. the number of pixels lying within a histogram bin.

1.3.4 Clock-induced charge

In an inverted CCD the holes present in the surface layer clearly have an important role to play in reducing the dark current. Unfortunately, during the readout phase the presence of these holes has a drawback. During readout the parallel electrodes make fast transitions to their high states. This repels the holes that have previously populated the surface back into the channel stops at high velocity where they

generate stray electrons through impact ionisation (Janesick 2001). These electrons constitute ‘clock induced charge’ (CIC). In a conventional CCD the CIC is barely noticed since it is swamped by the generally much higher read-noise. In an EM-CCD, the CIC can become the dominant noise source due to the effective absence of read-noise. Figure 1.11 shows the appearance of bias frames at three different levels of CIC. The CCD in question had a very high gain and the individual CIC electrons are clearly visible as discrete events. Note that these events have a large spread in height. The reason for this spread is ‘multiplication noise’ which is explained in the next section.

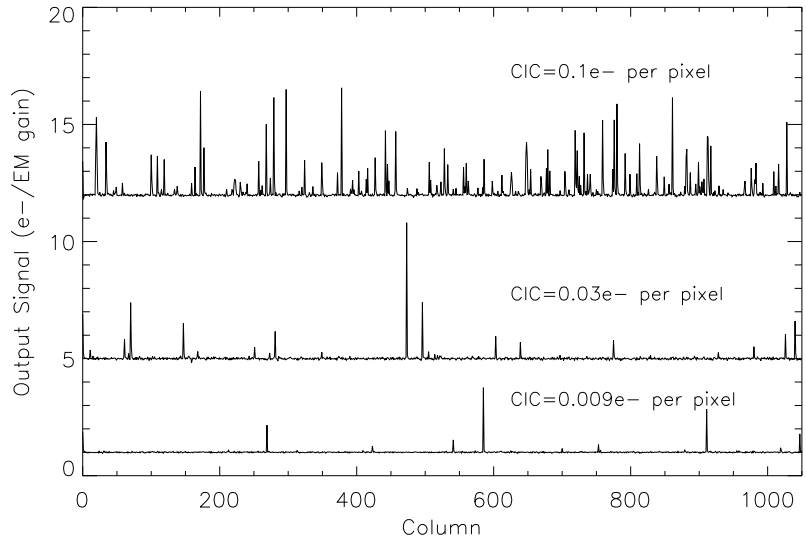


Figure 1.11: Appearance of CIC in cross-sections through an image. Three profiles are shown from 3 cameras experiencing a range of CIC levels.

1.3.5 Multiplication noise

The multiplication process in an EMCCD has a low probability of actually producing gain. In moving from one element in the EM register to the next, an electron has approximately a 1% chance of creating an additional electron. The high gains ($g_A = 1000$) that are sometimes used are only achievable if we use EM registers containing several hundred stages. This distribution of gain throughout many stages has the effect of producing a large variance in the output signals resulting from single electrons entering the EM register. This uncertainty in the gain experienced by a photoelectron constitutes an additional noise source in an EMCCD and is known as multiplication noise.

Multiplication noise source has been studied in some depth by Robbins & Hadwen (2003). They introduce a noise factor F . This is related to the standard deviation of

the input signal σ_{in} , the output signal σ_{out} and the multiplication gain g_A as follows:

$$F = \frac{\sigma_{out}}{\sigma_{in} g_A}. \quad (1.4)$$

They then go on to derive :

$$F^2 = \frac{1}{g_A} + 2(g_A - 1)g_A^{-\left(\frac{N+1}{N}\right)}, \quad (1.5)$$

where N is the number of stages within the EM register. It can be shown that as N and g_A become very large (as they do in a practical camera system), F tends to $\sqrt{2}$. This has the effect of multiplying the noise in the input image by $g_A\sqrt{2}$. Since the signal will only be multiplied by g_A , the overall effect is to reduce the signal-to-noise ratio in the image by a factor of $\sqrt{2}$. Statistically this is equivalent to a halving of the quantum efficiency of the camera.

This important result was tested in the laboratory by using an EMCCD camera to take a series of flat-field frames of increasing intensity. At each signal level the mean and the variance of the flat fields were measured. The sequences were repeated at a total of three different EM gain levels. The results are shown in Figure 1.12. As can be seen, the variance in the EM frames was equal to $2 \times$ their mean, thus confirming the earlier theoretical result. The effects of multiplication noise have in fact already

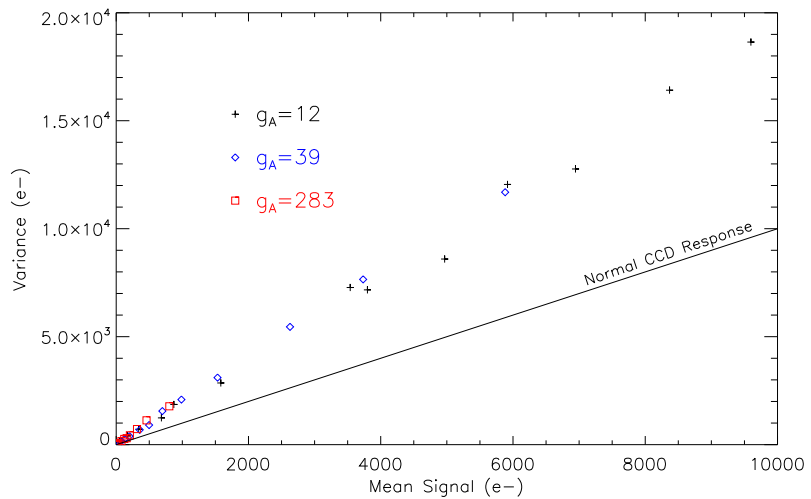


Figure 1.12: Variance as a function of mean signal level for an EMCCD as opposed to a conventional CCD. Three distinct EM gains were investigated. The variance in the EM frames is higher by a factor of 2 due to the effects of multiplication noise.

been shown earlier in Figure 1.10 which demonstrates that for an output signal of 300 e⁻ and an EM gain of 100 the input signal could have been either 3 or 4e⁻ with almost equal probability.

1.3.6 Normal or Conventional mode

If the CCD has a normal output in addition to the EM output, as is the case with the CCD201-20, then we can use the device with great flexibility. If the signal is high, and therefore not read-noise dominated, then we can use the normal output to improve our signal-to-noise ratio (SNR). The detector then behaves as a normal scientific CCD. As there is no EM gain, neither is there any multiplication noise. The equation for calculating the SNR for the normal output is shown in Equation 1.6:

$$\text{SNR}_N = \frac{M}{\sqrt{(M + \nu_C) + \sigma^2}}, \quad (1.6)$$

where M =mean photo-charge per-pixel, ν_C =mean CIC-charge per-pixel and σ =read-noise in the output amplifier expressed in e^- . This formula ignores any contribution from sky background and dark current.

1.3.7 Proportional or Linear mode

Proportional or linear mode is the mode where the amount of photo-charge collected by a pixel is taken as being proportional to the signal in ADUs.

If we then switch to the EM output of the CCD we add multiplication noise and at the same time reduce the read-noise by the EM multiplication factor g_A . The achievable SNR is shown in Equation 1.7. The factor of 2 in the denominator accounts for the multiplication noise (see Section 1.3.5).

$$\text{SNR}_L = \frac{M}{\sqrt{2(M + \nu_C) + (\sigma/g_A)^2}}. \quad (1.7)$$

There is therefore a cross-over point above which the SNR is higher with a conventional detector. This is shown in Figure 1.13.

1.3.8 Photon counting mode

Photon-counting mode is the mode where the amount of photo-charge collected by a pixel is no longer proportional to the signal in ADUs. Instead, a threshold is applied to every pixel and if the ADU value of that pixel exceeds the threshold then the pixel is interpreted as containing 1 photoelectron. All pixels below the threshold are then interpreted as having no signal. The process is shown in Figure 1.14.

Since a pixel is either equal to one or zero photoelectrons, the effects of multiplication noise are eliminated. The relevant SNR equation is shown in simplified form in

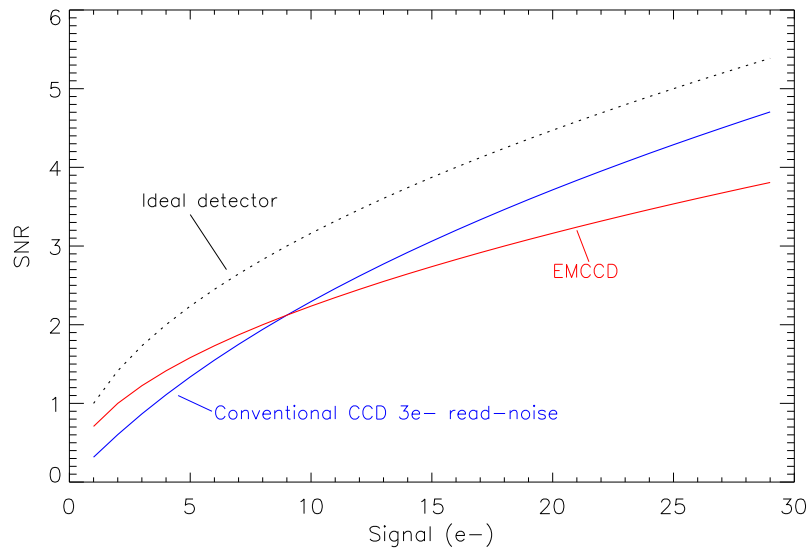


Figure 1.13: Signal-to-noise ratio as a function of signal level. The SNR of an EMCCD is compared with a conventional low noise CCD and an ideal detector. The amplifier read-noise is $3e^-$.

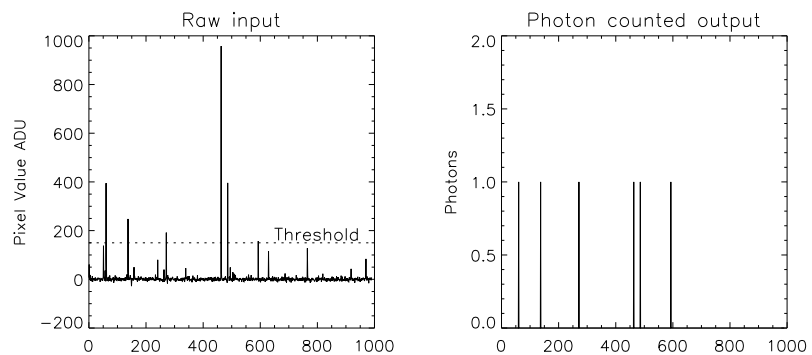


Figure 1.14: Photon counting method using a pixel value threshold. The x-axis shows the column number of the pixels.

Equation 1.8.

$$\text{SNR}_{PC} = \frac{M}{\sqrt{(M + B_C)}}. \quad (1.8)$$

It is assumed that all the events are counted (i.e. the threshold is low enough to lie below all genuine photoelectron events) and that the amplifier noise is negligible. Note that a CIC term is included but its units are different to those used in Equations 1.6 and 1.7; the CIC, B_C , now needs to be quoted in units of mean CIC counts per pixel rather than the mean CIC charge per pixel used earlier. This is because a mean CIC charge of, for example, $0.1\text{e}^- \text{ pix}^{-1}$ is not the same as a mean CIC count rate of $0.1 \text{ counts pix}^{-1}$. See Section 4.1.5 for a more detailed explanation of why this is. Given the fact that single photoelectron events have a distribution heavily skewed to lower values it is necessary to set the threshold as low as possible whilst at the same time ensuring that it does not go so low as to produce false triggers from pixels containing just the Gaussian read-noise. As the threshold rises the proportion of ‘lost’ photoelectrons steadily rises and the effective QE of the photon-counting system falls. We can calculate this effect by integrating Equation 1.2. The probability of a photoelectron being counted $P_d(T)$, where T =threshold in electrons at the output of the EM register, is then given by:

$$P_d(T) = \frac{1}{g_A} \int_{n=T}^{\infty} \exp\left(-\frac{n}{g_A}\right) dn = \exp\left(-\frac{T}{g_A}\right). \quad (1.9)$$

It is perhaps easier if we express the threshold as a fraction of the mean size of a photoelectron:

$$P_d(t) = \exp(-t) \text{ where } t = T/g_A. \quad (1.10)$$

So if a threshold of 0.1e^- is chosen then the probability of a photoelectron event being counted is 0.905.

Photon-counting will only work in the low signal regime. If there is a significant probability of a pixel receiving two photons within a single exposure then only one of these will be photon-counted. This effective loss of sensitivity is called coincidence loss and is described by the following equation (e.g. Daigle et al. 2008) :

$$F(M) = \frac{1 - \exp(-M)}{M}. \quad (1.11)$$

Here, $F(M)$ is the detected fraction of photons and M the mean number of photons per pixel expected during the integration. So for $M=0.1$ the equation shows us that we will count at most 95% of the photons. Basden et al. (2003) have investigated the use of multiple thresholds as a way of partially overcoming coincidence losses.

An interesting example of photon counting is shown in Figure 1.15. The EM camera was set up in the laboratory with a $50\mu\text{m}$ pinhole placed a small distance in front

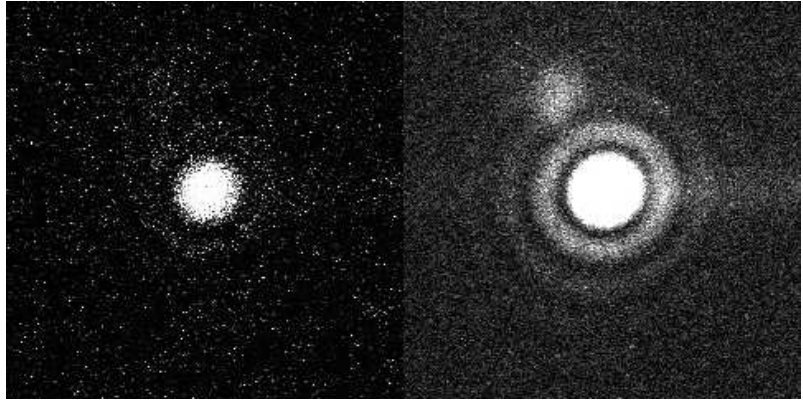


Figure 1.15: Demonstration of the wave/particle nature of photons. The panel on the left shows a single input frame. Shown on the right is the sum of 50 thresholded input frames. The Airy rings, a wave phenomena, are shown composed of discrete photon events.

of the CCD. This pinhole was illuminated by a very faint LED approximately 50cm distant. No lens was required in the setup. Diffraction through the small pinhole then projected an Airy diffraction pattern onto the EMCCD. The LED intensity was varied, along with the exposure time, so that the brightness of the Airy rings was suitable for a photon counting analysis of the images, i.e. the mean intensity was $<0.1e^-$ so as to avoid significant coincidence losses. A series of 50 frames were then taken and their photon-counted sum combined into a single image. This is shown in the right-hand panel of the figure. On the left is one of the 50 raw input frames. This gives a nice demonstration of the dual nature of the photons: wave-like when passing through the pinhole but particle-like when detected by the CCD.

1.4 Underscan and overscan regions

The CCD201 has a total of 1056 physical columns of which the central 1024 are sensitive to light. This light sensitive region is bordered on either side by two groups of 16 dark-reference columns that are shielded from light by an aluminium overcoat. When the EMCCD is read out through the EM amplifier (see Figure 1.8) the natural width of the image is 1080 columns. This is the width of an image that will fit exactly twice into the length of the combined serial and EM registers (the full extent of which is known as the serial pipeline). Reading out an image of this width will result in extra image columns appearing that do not correspond to physical columns. Pixels in these extra columns, although not containing photo-charge or image area CIC and dark current will still contain CIC and dark current generated in the serial and EM registers. They will thus lie very close to the bias level of the EMCCD. These extra ‘bias columns’ to the left of the image area are known as the

serial underscan, those to the right are known as the serial overscan. This is shown in Figure 1.16.

We now look at the vertical organisation of the EMCCD image area. It has a total of 1024 light sensitive rows again bordered at top and bottom by additional physical rows that are shielded from light by an aluminium overcoat. Above the image area there are 6 of these rows, below it there are 2. The total number of physical rows is therefore 1032. With this camera a total of 1050 rows are read out which means that there are an additional 18 rows above the image which do not correspond to physical image rows. These are known as the vertical or parallel overscan rows. Although not containing any photo-charge or image-area dark current they will still contain any CIC and dark current generated in the parallel transfer as well as any CIC generated in the serial and EM registers. The examination and comparison of

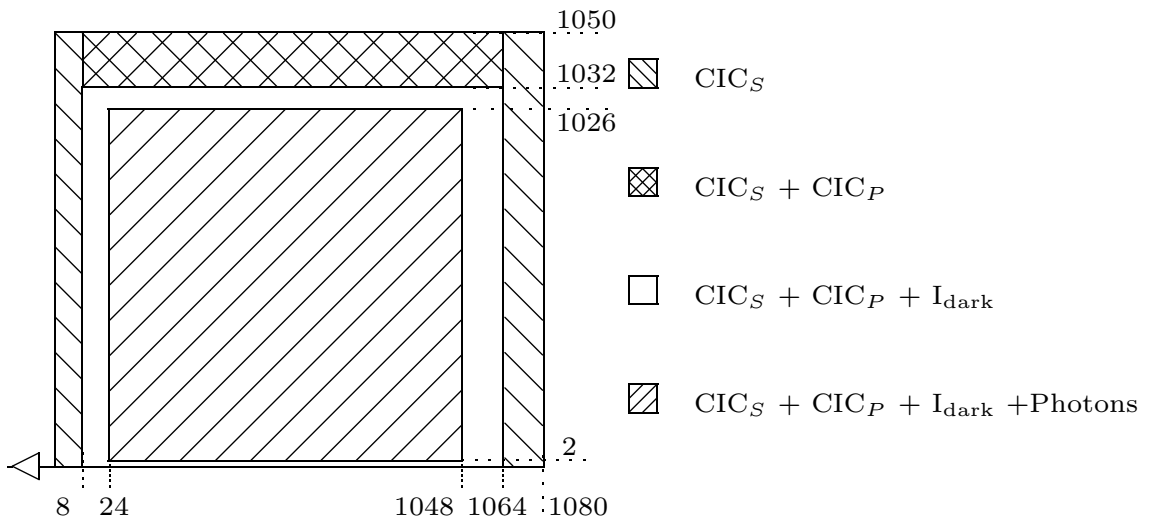


Figure 1.16: Underscan and overscan regions of the CCD201 showing the various noise/signal sources present in each. CIC_S refers to CIC generated in the serial and EM registers, CIC_P refers to that generated in the image areas and I_{dark} refers to the dark current generated in the image area.

these various image/bias areas can yield valuable clues to the levels of the various noise sources present in the EMCCD (see Chapter 4).

1.5 The QUCAM

When it was first announced it was clear that EMCCD technology was a solution looking for a problem. They were first intended for military and security imaging applications where moonlight and even starlight could provide sufficient illumination to yield a useful image. At an astronomical observatory, astronomers frequently complain that the read-noise of their detectors is too high. A noiseless detector

should surely be of interest even with the presence of multiplication noise. In the 1980s the IPCS system remained in demand long after CCD detectors with their vastly superior QE were made available. The fact that IPCS had zero read-noise (due to an internal avalanche gain mechanism) more than made up for its 5% QE (it was based on vacuum tube technology. Read-noise dominated regimes are encountered, for example, when faint sources are observed at high spectroscopic resolution in the absence of moonlight. Here, an already faint signal is spread out by the spectrograph over many pixels on the detector and the signal can easily be just a few photons per-pixel or less. EMCCDs are greatly superior to the IPCS but the situation is the same in that certain astronomical observations are completely dominated by read-noise and a 50% drop in effective QE due to multiplication noise in exchange for approximately zero read-noise is a price that many astronomers are willing to pay.

The first people to start exploiting EMCCDs in astronomy were Craig Mackay's group at the University of Cambridge. They used a 512 x 512 pixel CCD97⁴ on the Nordic Optical Telescope for high-speed imaging. Their technique, called 'lucky imaging' (Law et al. 2006) used the high speed capabilities of EMCCDs to produce high spatial resolution (in some cases diffraction limited) images during periods of low atmospheric turbulence. These occur in a random fashion and for short periods only, interspersed with longer periods of poorer atmospheric conditions. By taking many images at high speed (25Hz) and then adding together only those images that had the highest resolution, they were able to offer a way of removing to a large extent the blurring effects of atmospheric turbulence. A few years later the European Southern Observatory (ESO) decided to use EMCCD technology for their future high-speed wavefront sensor cameras (Downing et al. 2008). These cameras will be used to measure at high speed ($>1\text{kHz}$) the wavefront distortions induced by the atmosphere on the light of a faint star. These measurements will then be used to control, in real time, the shape of a deformable mirror that compensates for these distortions. At least two other groups have subsequently built EMCCD cameras intended for astronomy: Olivier Daigle's at the Université de Montréal (Daigle et al. 2008) and Derek Ives at the UKATC (Ives et al. 2008).

At the Isaac Newton Group (ING) where I was working at the time that it first became available there was little interest in EMCCD technology so I decided to build a series of cameras in an attempt to stimulate interest. The first of these used a small format 128 x 128 pixel CCD60⁵ and the camera was eventually incorporated into an adaptive optics system as a wavefront sensor (Tulloch 2006). I then designed

⁴E2V CCD97 data sheet: <http://www.e2v.com/assets/media/files/documents/imaging-l3vision/CCD97.pdf>

⁵E2V CCD60 data sheet: <http://www.e2v.com/assets/media/files/documents/imaging-l3vision/CCD60.pdf>

and built another camera, QUCAM1, using a CCD97 to gain experience with larger format detectors. This required the design and construction of a high-voltage clock generator board which I also did myself. Funding was eventually obtained from the ING to build a further EMCCD for use on the ISIS⁶ intermediate dispersion spectrograph. This camera, called QUCAM2, containing a 1k x 1k pixel CCD201-20⁷ was also designed and built in-house. Later, additional funding was obtained to buy a spare EMCCD and rather than let it languish on the shelf it was decided to incorporate it into a further EMCCD camera: QUCAM3. The two QUCAMs could then be used together on the red and blue arms of the ISIS spectrograph on the 4.2m William Herschel Telescope (WHT⁸). The first scientific application of QUCAM2 is described in Chapter 7 of this thesis. At the time of writing there have been two further requests from external observers to use these cameras, so the original aim of generating interest has been successful.

⁶ISIS: <http://www.ing.iac.es/Astronomy/instruments/isis/index.html>

⁷E2V CCD201 data sheet: http://www.e2v.com/assets/media/files/documents/imaging-space-and-scientific-sensors/A1A-100013_2_v1.pdf

⁸WHT: <http://www.ing.iac.es/Astronomy/telescopes/wht/>

Chapter 2

Design of the Camera

A camera was built to house an E2V technologies CCD201 EMCCD for use on the ISIS spectrograph of the WHT. The CCD201 has an image area containing 1024x1024 pixels each measuring $13\mu\text{m}$ square. It is of frame transfer design and so contains a similarly sized storage area. The camera is of cryogenic design so as to give the best low-noise performance. The camera was named ‘QUCAM2’.

In this chapter the key elements of the mechanical, electronic and software design of the camera are described. I did the mechanical design for the internal cryostat parts used to mount the CCD at the required position in the cryostat. I also designed the cabling and the high-voltage clock board. The software design was based heavily on existing code supplied by the manufacturers of the CCD controller. All code modifications were done by myself.

2.1 Mechanical and thermal design of the camera

The camera was built inside a 2.5 litre Oxford Instruments liquid nitrogen (LN_2) cryostat. A 25mm pump port ensures efficient pumping and an activated charcoal getter attached to the nitrogen tank is used to maintain the vacuum. Viton ‘O’ rings and Fomblin vacuum grease were used to seal the vacuum ports. These materials have exceptionally low vapour pressure, important for good vacuum maintenance. The camera faceplate is of a standard design allowing interface to any ING instrument. The faceplate contains a 4mm thick fused silica window which is AR coated on both sides. This material was chosen not just for its strength (it must support atmospheric pressure) and optical transmission but also for its low radioactivity. Optical materials containing, for example, potassium can emit charged particles that can raise the noise level of the CCD. Electrical connections to the inside of

the cryostat were made through two Amphenol vacuum feed-throughs. One carries all of the CCD signals, the other the temperature sensor, heater and pre-flash LED signals. This LED, mounted close to the CCD, proved extremely useful for verifying camera operation.

The following figures show how the camera was assembled. The empty cryostat with the faceplate removed is shown in Figure 2.1. The vacuum-side components

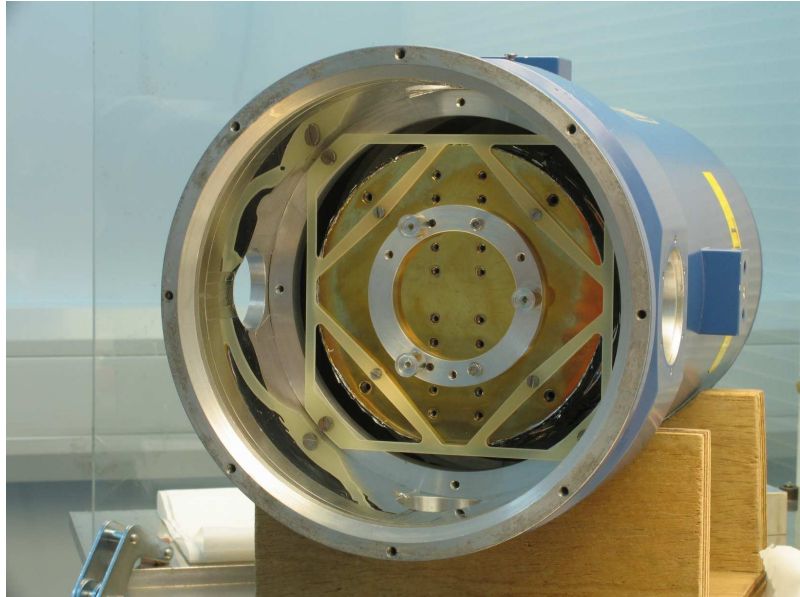


Figure 2.1: Empty cryostat. The top of the LN₂ tank is visible.

of the camera were all degreased, ultrasonically cleaned and vacuum baked in an oven for several hours prior to assembly. Figure 2.2 shows these freshly cleaned parts. Further handling was done using latex gloves in a laminar flow work bench to ensure the parts were not subsequently contaminated. The assembly began with the attachment of the ‘spider’ to the LN₂ can. This structure provided a base on which to assemble the rest of the focal plane components. The spider rested on three captive compression springs that only loosely held it in position. Later, when assembly was complete, these springs forced the CCD assembly, via three ball bearings positioned at the ends of the spider arms, into contact with three kinematic mounts on the rear side of the faceplate. The mechanical position of the CCD was thus referenced to the faceplate and *not* the LN₂ can. This improves mechanical stability since the can is a poor reference surface, suffering both flexure and thermal contraction. The faceplate, in contrast, is a very solid structure and is in turn directly clamped to the spectrograph. Figure 2.3 shows the spider attached. Additionally, four flexible thermal braids can be seen near the centre of the figure. One of these is used to directly cool the spider, the others make contact with copper caps positioned on top of three G10 glass reinforced plastic (GRP) pillars. These pillars, which are hollow and have very low thermal conductivity, act to thermally isolate the spider from



Figure 2.2: Camera components ready for assembly. The CCD itself is visible at top left, top centre is the radiation shield and top right is the spider. Immediately below the CCD can be seen the baseplate with two heater resistors and the Pt100 temperature sensor attached. At bottom centre is the detector printed circuit board (PCB) and its vacuum-side wiring harness.

the rest of the camera assembly. The pillars are perforated at their bases to avoid trapped volumes that could prevent efficient vacuum pumping.

The next stage was to mount the CCD baseplate atop the pillars as shown in Figure 2.4. A Pt100 temperature sensor and a 100Ω heater resistor were then attached to the baseplate. This sensor is a standard type of thermistor demonstrating a linear relation between temperature and resistance over a large temperature range. It is composed of a fine coil of platinum wire embedded within a ceramic package and has a resistance of 100Ω at 0°C . The sensor and heaters were mounted close to each other to minimise the possibility of temperature servo oscillations. Three small nylon pillars protrude from the baseplate and were used to mount the detector head board. Figure 2.5 shows this board, already mounted with an engineering grade detector. CCDs designed primarily for cryogenic operation usually come with a metallic package containing tapped holes and multi-way connectors. This makes both the electronic and thermal connections easy to arrange. The CCD201 used in this camera, in contrast, used a rather unfortunate ceramic design with connector pins protruding from its rear surface. To ensure efficient cooling, the package had to be held against the baseplate using a pressure clamp that pulled down on its top surface. A piece of indium foil between the CCD and baseplate provided some compliance and improved the thermal contact. The thermal resistance between the baseplate and detector were not measured. Comparison of the manufacturer's models with actual detector dark current, however, suggest a 10 degree thermal gradient across the mounting interface.

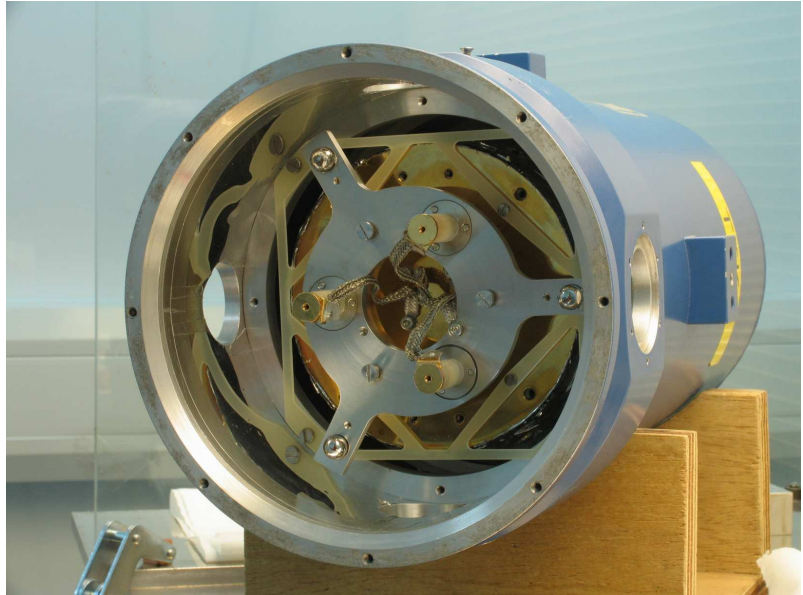


Figure 2.3: The ‘spider’ and the thermal braids.

The final step was then to attach a radiation shield over the assembly. This was bolted on to the spider at three points. This caused the shield to be cooled to an intermediate temperature. Figure 2.6 shows the radiation shield in place. Note its polished low-emissivity finish. On the first cool-down it was clear that the thermal resistance between the CCD and LN₂ can was too low. Ideally the bottoming-out temperature of the CCD with the servo heater switched off should be about 20 degrees below operating temperature so as to ensure low servo heater power and good liquid nitrogen hold-time. Based on previous experience with the QUCAM1 camera the operating temperature was initially chosen to be 180K. During the fine tuning phases of the camera development (see Section 3) this was actually found to be an excellent choice. It was therefore necessary to remove one of the thermal braids. Figure 2.7 shows the behavior before and after the removal of the braid. The operating temperature of 180K was reached in about 3 hours, after the braid removal, which is convenient for observatory operations. The radiative load on the CCD originates almost entirely from the rear surface of the cryostat window which is at ambient temperature and of high emissivity in the thermal infrared. In other directions the detector is shielded by cooled low-emissivity surfaces. The load was estimated at 70mW. The conductive load is almost entirely due to the CCD signal-wires and temperature servo connections. This load was estimated at 400mW. The total thermal load was easily handled by the 2.5l capacity cryostat which demonstrated a hold time, with no heater servo power and the cryostat in the vertical position, of about 22 hours. With the heater active there would have been some reduction in hold-time but this was not accurately measured. Hold time was nevertheless more than sufficient to maintain temperature between the 8 hour LN₂ fill cycles used at the WHT.

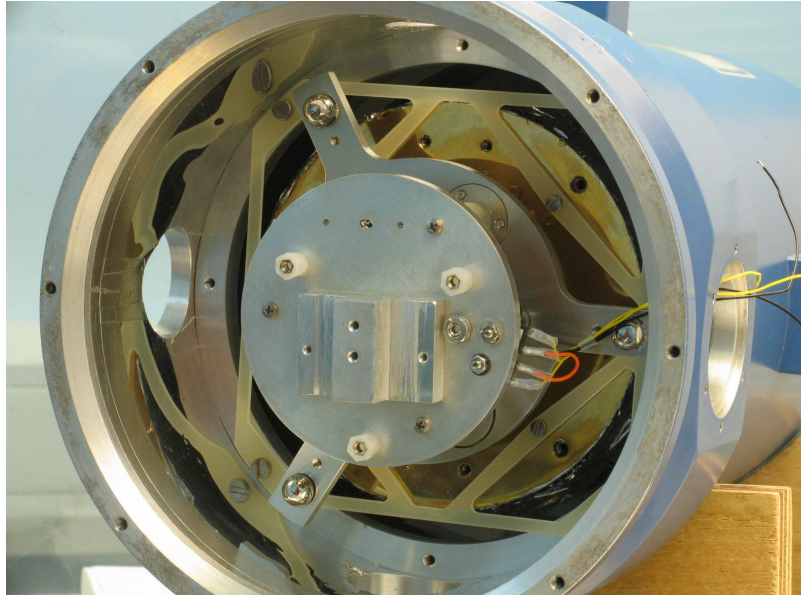


Figure 2.4: Baseplate shown attached to the GRP pillars. Below the baseplate the spider is partially visible. Protruding from the baseplate can be seen the three nylon pillars used to mount the detector PCB. The CCD itself is fitted atop the rectangular block at the lower centre of the baseplate.

2.2 The camera electronics

The camera was operated using a standard Astronomical Research Cameras Generation 3 controller also known as a Leach or SDSU (San Diego State University) controller. An additional board was needed, however, to generate the high-voltage (HV) multiplication clock required by the EM register. I designed and built this in-house (see Section 2.2.3).

2.2.1 The camera controller

This contains 6 electronic boards. These consist of a timing board, a standard clock generator board, the custom HV clock generator board, a video processor board, a utility board and a power control board. The heart of the controller is a DSP (digital signal processor) based timing board that performs the clock sequencing and fibre optic communication with the host computer. The DSP, a Freescale DSP56300, is programmed using assembler language. Its program code is downloaded over the fibre optic interface, which is convenient since many code changes were required during the development of the camera. The processing of the video signals and bias generation is carried out by the video board. This contains two 16-bit video channels, one of which is used by the conventional CCD output, the other by the electron multiplying output. The maximum pixel rate through each channel is 1Mpix s^{-1} , limited by the ADC conversion time. CCD clock generation is carried out by

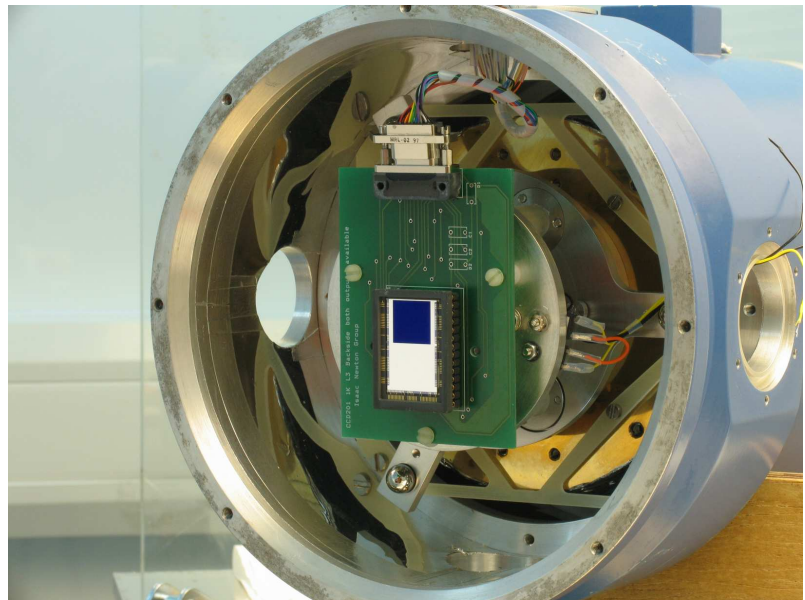


Figure 2.5: The detector and its printed circuit board. The detector cabling is already connected in this image whereas the temperatures servo connections (shown as loose wires protruding from the right-hand orifice) still require soldering to their vacuum feedthrough connector.

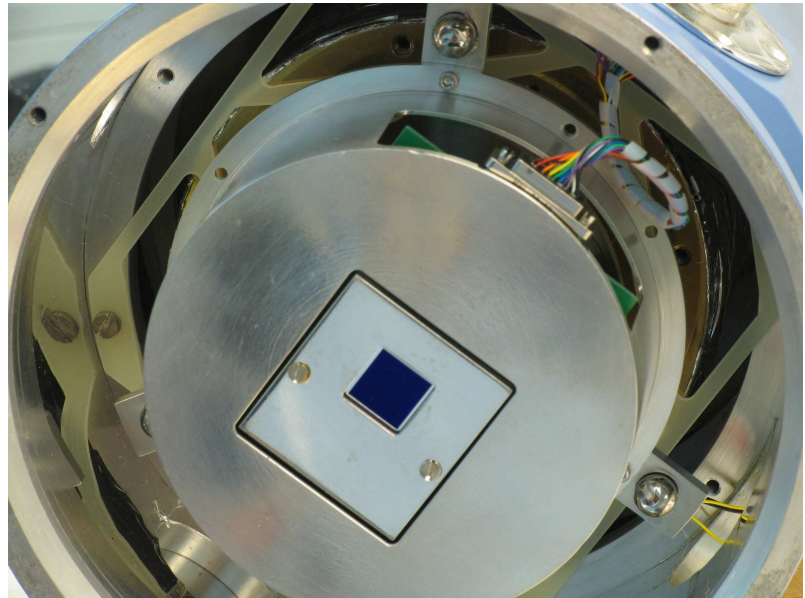


Figure 2.6: Radiation shield in place. The clamping plate that holds the CCD package against the cold-finger is also visible within the radiation shield aperture.

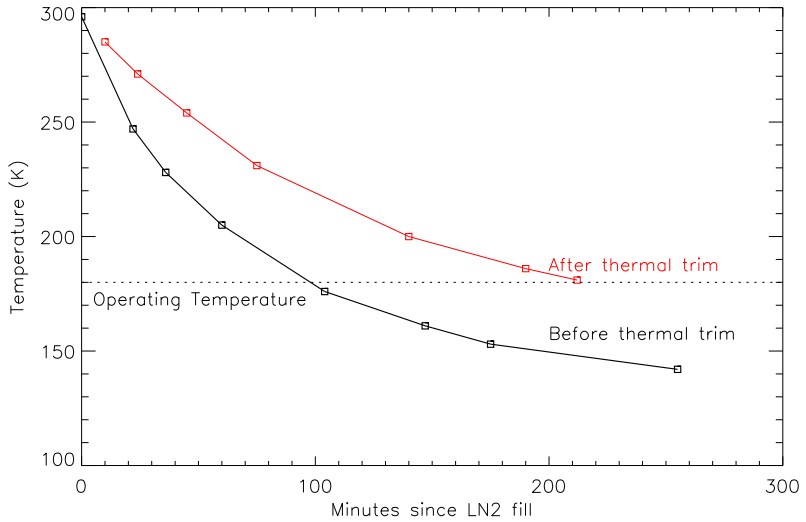


Figure 2.7: Camera cool-down following the initial LN_2 fill using two thermal braids (top curve) and three thermal braids (bottom curve).

the standard clock card. The minimum time between consecutive clock transitions is 40ns which proved to be rather slow. The high voltage clock board supplies only a single clock and is described in detail in Section 2.2.3. Temperature servoing and shutter control are performed by the utility card which contains the necessary digital-to-analogue-converters (DACs) and power transistors. This utility card has a separate DSP processor on which the temperature servo control code runs. A simple proportional algorithm was found to be adequate given the fairly constant thermal load on the detector. The utility board communicates with the timing board over a fast serial link through the controller backplane. Commands between the host computer and the utility board are routed via the timing board. The power control board ensures that the DC supply voltages to the controller are within specification so as to protect the delicate CCD from possible damage due to a faulty power supply unit (PSU).

2.2.2 Cabling and head board

The electrical contacts to the CCD were made via a small custom-designed printed circuit board: the ‘head board’. This board has locations for the inclusion of an over-voltage protection diode and some decoupling capacitors for the bias voltages, but in the end they were not used since there was a suspicion that they contributed to a bias gradient problem during the CCD optimisation process. The board provides a convenient way of connecting the CCD pins to a micro-D connector. The connector harness from vacuum feed-through to the board consists of twenty two 28-gauge copper wires insulated with polytetrafluoroethylene (PTFE). The narrow gauge ensures low thermal leak and the PTFE ensures low outgassing. No shielding



Figure 2.8: A view inside the SDSU controller showing the high-voltage clock board.

is used on any of these wires so as to minimise the conductive load. The cryostat itself provides an efficient Faraday cage and cross talk between signals was not found to be a problem. The board itself was manufactured from normal epoxy/glassfibre material. Its outgassing behaviour was minimised by an extended vacuum bake. The CCD signal wires use an Amphenol 41-way military circular connector brazed to a vacuum flange in order to connect with the outside world. This connector assembly was helium leak tested prior to the assembly of the harness, since brazed joints are prone to low-level leaks. A chain-mounted metal dust cover is mounted over this connector when not in use, so as to guard against electrostatic damage to the detector. Four other wires lead from a second 12-way vacuum feed-through to the cold parts of the camera. The first pair carry heater current to the 100Ω TO220-packaged power resistor, the second pair connect to the Pt100 resistance thermometer. This thermometer was constructed by drilling along the long axis of an M4 bolt and gluing a Pt100 element within the hole using Thorseal vacuum epoxy. Attachment to the detector baseplate then just required a nut and compression washer, thus permitting easy replacement.

2.2.3 Generation of the high-voltage clock

The standard SDSU controller can only produce clock waveforms with an amplitude of $\pm 10V$. The E2V EMCCDs require a multiplication clock of up to $50V$ amplitude, so it was necessary to design and build a custom HV clock board. The finished board is shown in Figure 2.8. The board has the same dimensions as a normal SDSU card and is attached to the backplane in the normal way. No signals are obtained from the backplane, only $5V$ and $\pm 16V$ power as well as ground. Signals are fed to-and-from the card via a 9-way D-connector on its front edge. There is

also the option to make the ground connection through this connector, instead of the backplane, by swapping a link. This flexibility was included in the design in case any earthing/ground-loop problems were later encountered. The first stage of the circuit generates a stable 60V bus using two series-connected commercial 30V DC:DC converter units. This bus voltage is then regulated down using a standard textbook-design programmable power regulator containing an op-amp and power transistor. The regulator produces a stable output of between 20 and 49.4 volts. The output clock driver consists of two high speed bipolar transistors connected in the standard push-pull configuration that allows rapid switching of the output clock line between ground and the regulator output voltage. The base drive waveforms for this transistor pair are derived from an input transistor-transistor logic (TTL) signal supplied from one of the spare clock lines on the standard SDSU clock card. This input signal was buffered using two 74HCT04 series inverters, connected in parallel for extra drive current. Resistor-capacitor (RC) filters on the transistor bases softened the edges of the output high-voltage waveform. Further output filtering came from a 100Ω series-connected resistor which, together with the CCD input capacitance, formed a low-pass filter that removed ringing and cleaned up the waveform. The slew rate of the HV clock was $+65V/\mu s$ and $-36V/\mu s$.

The avalanche multiplication gain of an EMCCD is critically dependent on the phase of the HV clock. In particular, the HV clock must be at its maximum value at the moment that clock $\phi H1$ goes low (see Figure 4.5). Small phasing errors between these two clocks can give huge changes in gain. For this reason four test points were included at the edge of the board, carrying all the serial clock phases. With the HV board mounted uppermost within the SDSU controller it was then possible to remove the side cover of the controller and access with oscilloscope probes all of the relevant clock pins during the optimisation process. A further connection to the board is made from a digital-to-analogue converter (DAC) output on the SDSU video board. This signal varies between 0 and 5V and provides the programming input to the HV regulator. Changes in this DAC voltage (which were under full software control) then act as an EM gain control signal. A chain of 3 precision op-amps is required to amplify and invert this signal prior to reaching the regulator circuit. Precision metal film resistors are used throughout to minimise any temperature coefficients. The output of the clock card is shown in Figure 4.5. As can be seen, the waveform is clean with no ringing at the edges.

2.3 Camera control software

It was important that the camera integrated seamlessly into the existing UltraDAS (Rixon et al. 2000) observatory data acquisition system (uDAS). For the most part

this was straightforward, requiring that the camera respond to a few simple commands such as changing readout speed, performing a clear, a readout, switching to idle mode or setting up a window. The camera did, however, operate in fundamentally different ways to a standard ING science camera and I had to develop some additional software to cope with this. The first of these differences was that the camera had two operational outputs: the EM output and normal output, each of which might be required during a night's observations. Some other ING cameras do have multiple outputs but they are unused and serve merely as spares should the primary output fail. Configuring a new output then requires a recompilation of the controller software and a reconfiguration of the observing system. A second important difference is the need to make long sequences of short exposures with a low frame-timing jitter. uDAS does permit such long sequences but their timing is easily perturbed by other tasks running on the (non-real-time) operating system. In order to remove this jitter (which can be several hundred milliseconds) the frame timing operation was delegated from the uDAS Sparc computer to the internal quartz oscillator of the SDSU controller. This oscillator was specified to have a stability of 100 ppm over its full operating temperature range. If, for example, we then use this to sequence a series of exposures lasting in total 30 minutes then it would correspond to an accumulated error of approximately 180ms in the start time of the final frame in the sequence. In reality this accumulated error should be much less since the actual operating temperature range is much smaller than the range specified in the oscillator data sheet. uDAS time stamps the first frame in the sequence using a network time signal. This has a claimed absolute accuracy of 1ms although this claim has never been rigourously tested.

2.3.1 Embedded controller software

Almost all of my programming effort went into the optimisation of the controller voltages and the phasing of the clocks. The basic code-framework was derived from previously existing camera control software used with other ING cameras. This code was written in Freescale DSP56300 assembler and compiled on a SPARC workstation. It was downloaded over an optical fibre into the controller prior to powering up the camera. A bootstrap electrically-erasable programmable read-only memory (EEPROM) resident in the controller provides all the basic commands for receiving and then running the downloaded code. This EEPROM code is the factory default as supplied by SDSU. One important feature of the camera control code is that the HV multiplication clock is only applied during readout and not when idling. This provided some protection since EMCCDs can fail if operated with high gain

under high illumination for long periods¹. Gain should only be applied when required in order to reduce the chances of this happening.

¹E2V L3 sensor ageing technical note 5: http://www.e2v.com/assets/media/files/documents/imaging-space-and-scientific-sensors/Papers/low-light_TN5.pdf

Chapter 3

Initial characterisation of camera

This chapter describes the first iteration of the tuning of the camera's performance. The fundamental characteristics were measured and any potential problems highlighted so that later work could then concentrate on bringing improvements to those areas.

The manufacturer's data sheet¹ provided the starting point for the optimisation work. It gave the recommended setup voltages and waveforms. Each CCD, however, is different and will almost always benefit from a degree of fine tuning. This is particularly the case with EMCCDs where the optimisation parameter space is expanded to include factors such as temperature dependance of the gain, the presence of CIC, the need for a high voltage clock etc. These parameters are closely cross-coupled so that, for example, a decision to change the operating temperature due to excessive dark current may force a re-measurement of almost all other performance characteristics. Due to these complications it is estimated that the effort required to optimise an EMCCD is an order of magnitude greater than for a conventional CCD.

3.1 Serial clocking in an EMCCD

The temporal phasing between $\phi H1$ and $R\phi 2HV$ (see Section 1.3.1) is of critical importance. As $\phi H1$ goes low the charge falls under the high voltage phase $R\phi 2HV$. If the high voltage phase has not settled at its high state at this point then full multiplication will not occur. If this is the case then any clock jitter will give huge modulations in the EM gain. The phasing needs to be designed very carefully and checked with an oscilloscope. Figure 3.1 shows how the serial clock phases should

¹E2V CCD201 data sheet: http://www.e2v.com/assets/media/files/documents/imaging-space-and-scientific-sensors/A1A-100013_2_v1.pdf

appear during a pixel cycle. This figure also shows the position of two windows used by the video processor within the controller to measure the video waveform. The first of these windows, known as the reference window, is immediately prior to $\phi H3$ going low. The second, known as the signal window, lies immediately after. $\phi H3$ is the ultimate phase in the serial register and lies close to the output amplifier measurement node. There is actually an additional electrode called the output gate (OG) between this node and $\phi H3$ that is used to reduce capacitive coupling between clock phases and output amplifier. As $\phi H3$ goes low the charge that it contains is then dumped onto the node. The difference in the CCD MOSFET output voltage in these two windows is proportional to the pixel photo-charge. Using the two windows in this way reduces the read-noise considerably. These idealised waveforms can be compared with the actual camera waveforms shown in Figure 4.5.

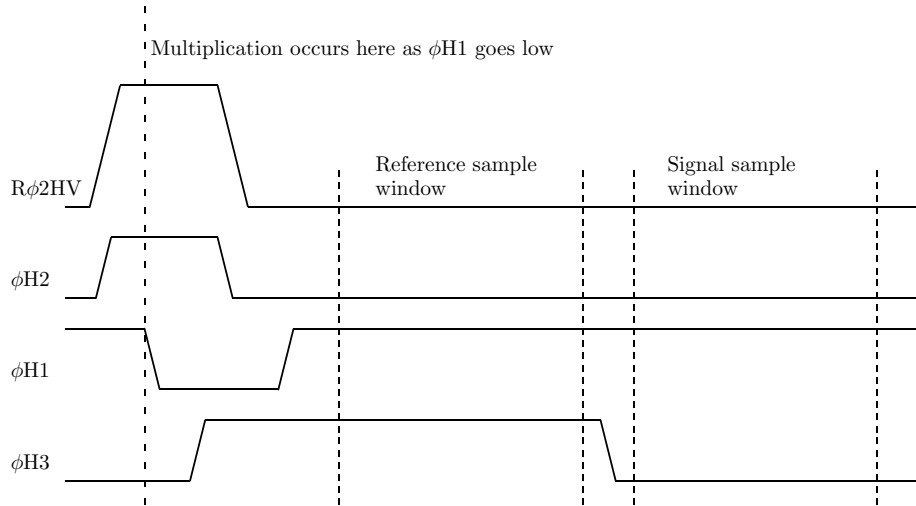


Figure 3.1: Serial-clock phasing in an EMCCD. The phasing between $\phi H1$ and $R\phi 2HV$ is of critical importance.

3.2 Measuring the system gain of an EMCCD

Counter-intuitively, it is possible to determine the system gain g_S of an EMCCD (defined in Section 1.3.2) without ever exposing the camera to light: a set of bias frames contains all the information needed. Ideally a stack of tens or even hundreds of bias frames are used since this improves the statistics of the measurements. Bias frames taken within a few tens of minutes of power-on will have large numbers of pixels affected by dark current (this takes several hours to finally settle to operational levels, see Section 3.5.4). These dark-current affected pixels will occupy a range of values dependent on the system gain. A small system gain will give a large spread in dark-current pixel values, a large system gain will give a correspondingly smaller range (remember that g_S is inversely proportional to g_A). The clearest way to

demonstrate this is by making a histogram of a dark-current contaminated bias frame. If a \log_e vertical axis is used, the dark current events will be seen to lie along a straight line of negative gradient. It can be shown mathematically that the value of this gradient is identical to $-1 \times$ the system gain in e^- per ADU, a useful result (Tulloch, 2004). In Chapter 1 the following equation was introduced:

$$P(n) = \frac{1}{g_A} \exp\left(-\frac{n}{g_A}\right), \quad (3.1)$$

where P = probability of the output signal being equal to n electrons and g_A is the EM avalanche multiplication gain. Taking logs of both sides:

$$\ln[P(n)] = \ln(1/g_A) - \frac{n}{g_A}. \quad (3.2)$$

If we then plot $\ln[P(n)]$ versus n the slope is given by $-1/g_A$.

At low ADU values things are complicated by the CIC events generated inside the EM-register. These do not lie neatly along a straight line on our histogram but instead show a large excess of low-value events. These are due to CIC events generated at intermediate positions within the EM register which experience less than full EM amplification. At the very low end the statistics are further complicated by the contribution of the read noise. However, if we restrict our analysis to the higher-value events we can still obtain an accurate result.

Knowledge of the system gain g_S was so important during camera development that a robust IDL² procedure was developed to automatically calculate it with minimal input from the user. This procedure took a user-selected group of input bias frames and used the histogram method described above to calculate the system gain. The user was prompted to select the linear range of the histogram over which the least squares fit was performed so as to exclude low level events affected by the read-noise and the in-EM register CIC events. Figure 3.2 shows the graphical output of this program. Note the clear excess at the low signal end and the way that the user selected fit region has avoided these events.

This gain measurement technique is very powerful since any EMCCD frame, as long as it contains a bias region or an image region with very-low illumination, will have information about the system gain g_S encoded within its pixel values. In camera systems that are very sensitive to gain stability it is therefore possible to continuously monitor the system gain. This gain technique will only work for weakly illuminated pixels. If the mean illumination exceeds approximately $0.1e^- \text{ pixel}^{-1}$, then

²IDL web page: <http://www.ittvis.com>

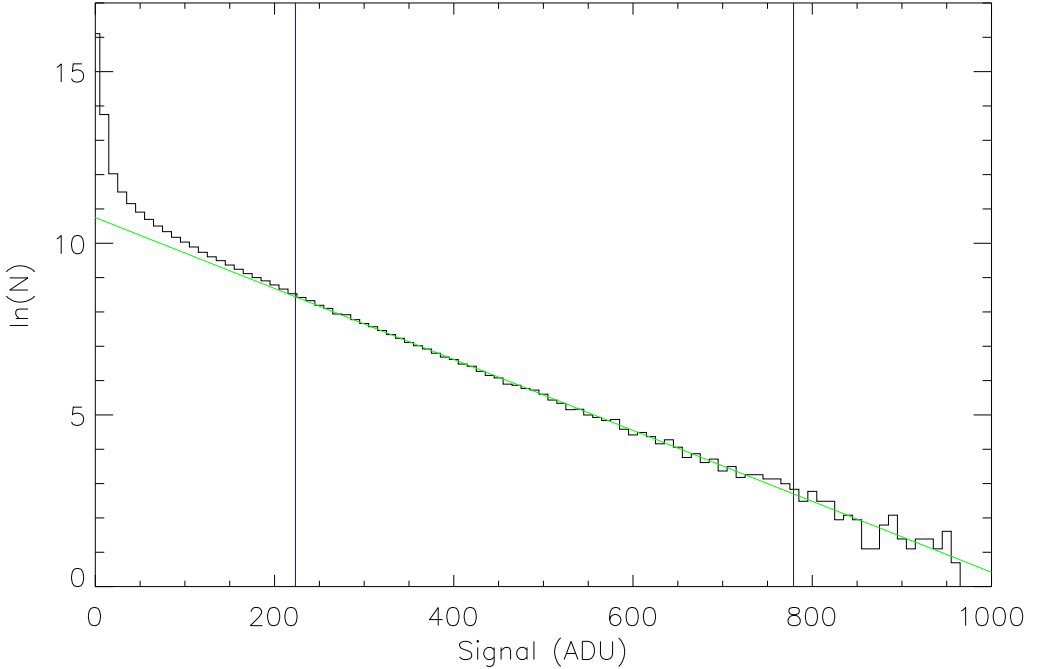


Figure 3.2: Image area dark current histogram used for gain calculation. The y -axis shows the \log_e of the pixel value histogram. The green line is a least square fit to the data between the user selected vertical blue lines. The gradient of the green line is equal to $-1 \times$ the system gain g_s in units of e^-/ADU . The source images had been bias-subtracted prior to the histogram.

the presence of pixels containing more than one electron will disturb the statistics. The method has been thoroughly tested using synthetic EMCCD bias frames (see Chapter 5) and gives results accurate to better than 1% for CIC/illumination levels below $0.02e^- \text{ pixel}^{-1}$. If the mean signal reaches $0.2e^- \text{ pixel}^{-1}$ the system gain will be underestimated by 10 percent. Imperfect serial charge transfer efficiency will also disturb the event histogram and lead to an overestimate of the true system gain g_s . One should therefore be cautious in applying this method to images that contain obvious charge transfer problems.

Unfortunately this method did not prove as useful as first thought. It was good for quick-and-dirty gain measurements but in later stages of development, where really accurate gain values were required, it was not sufficient. Here a photometric technique was used instead whereby a stable source (the LED mounted within the camera cryostat) was imaged and readout through the normal output (whose gain was already known from the photon transfer technique, Janesick 2001) and then, under identical conditions, through the EM output. A graph of signal versus exposure time was obtained using each output and the ratio of the gradients then gave the ratio of the system gains.

It was known from the CCD201 data sheet³ that EM avalanche multiplication gain rises steeply with decreasing temperature. Figure 3.3 shows the gain over a small range of temperatures close to the chosen operating point. This shows the importance of maintaining a stable temperature when operating an EMCCD camera.

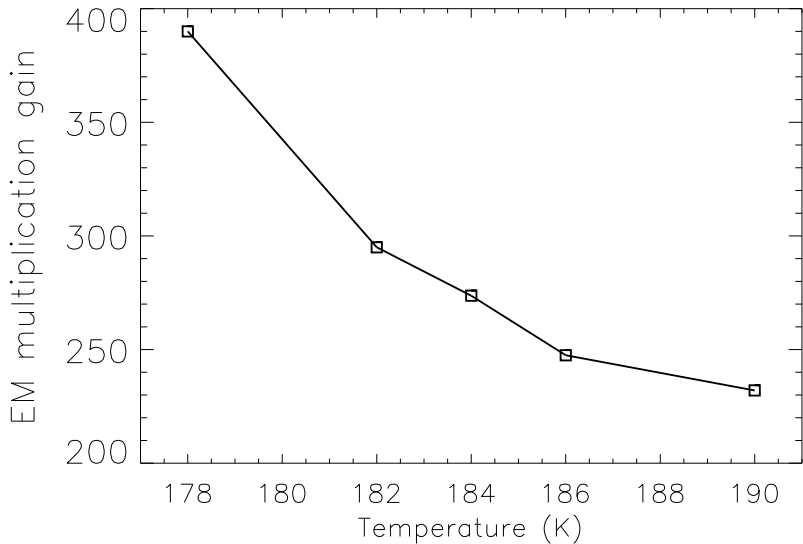


Figure 3.3: The temperature dependance of EM gain. The HV clock in this case had an amplitude of 41V.

3.3 Measurement of quantum efficiency

The quantum efficiency of the camera was measured at several temperatures using a stable light source. This source, shown in Figure 3.4, consisted of a tungsten-halogen lamp that projected a 5mm beam through a six-position filter wheel onto the CCD. The beam was defined by two apertures, one close to the lamp, the other close to the CCD. This approximately collimated beam was entirely intercepted by the CCD and also by a small 1cm² calibration photodiode that could be positioned in place of the CCD. The filter wheel contained interference filters with 10nm pass-bands.

One useful property of CCDs is that they are essentially large photodiodes and if a pico-Ammeter (a very sensitive current meter) is connected between the substrate pin and the dump-drain pin (the reset drain pin can also be used with some CCDs), then they will produce a photo-current proportional to the level of illumination. Operating a CCD in this ‘diode mode’ is extremely convenient since high-accuracy QE data can be obtained by simply ratioing the current produced by the CCD and the calibration diode and then multiplying by the QE of the calibration photodiode. This of course will only work if all of the light intercepted by the CCD is

³E2V CCD201 data sheet: http://www.e2v.com/assets/media/files/documents/imaging-space-and-scientific-sensors/A1A-100013_2_v1.pdf

also intercepted by the photodiode once the CCD is removed and the photodiode mounted in its place. It is therefore important that the illuminating beam has a small diameter. This is probably the simplest and most accurate method for measuring QE and has given data with other CCDs that is within a few percent of the manufacturer's models (Jorden et al. 2004). Alternative methods that use the CCD in imaging mode introduce additional variables into the measurement process. For example they require an accurate knowledge of the system gain of the camera. The light source has a very poor UV output, so the data points at 350nm are not very trustworthy since at this wavelength the detector dark current was comparable with the photo-current.



Figure 3.4: The quantum efficiency measurement rig. At the extreme left is a tungsten light source. The camera cryostat is shown mounted on the right. The black box between them contains a 6-position filter wheel.

The data obtained are shown in Figure 3.5. The CCD has a mid-band optimised coating that gives a peak-QE in excess of 90% at 600nm. The red response has a strong temperature dependance due to the fact that silicon becomes more transparent as it gets colder. At the chosen operating temperature of 180K the QE at H α is 85% and at H β it is 67%. There does not seem to be any compelling reason for selecting the operating temperature on the basis of optimising the QE.

3.4 Measurement of charge transfer efficiency

The charge transfer efficiency (CTE) proved rather difficult to measure with the CCD201. A normal science CCD has a sharp edge to the image area. Pixels beyond this edge will contain bias values. Examination of this edge for charge trailing can

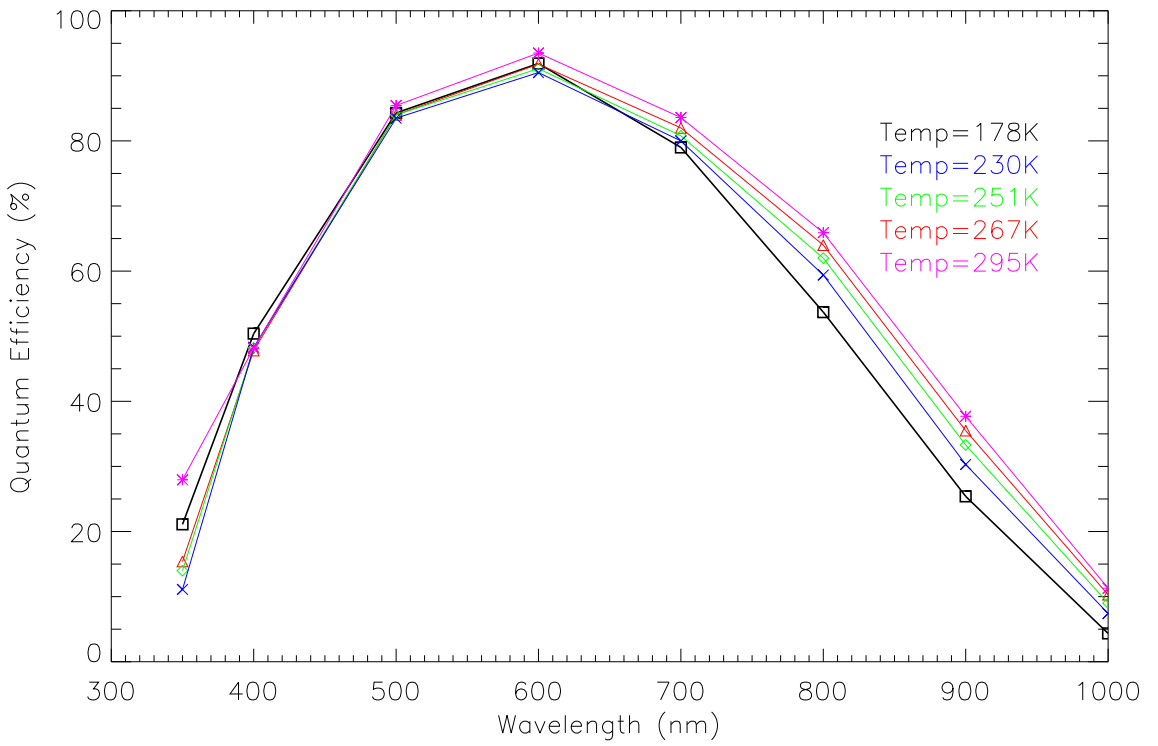


Figure 3.5: Quantum efficiency plots at various operating temperatures.

then yield the charge transfer efficiency. This is the so called extended pixel edge response (EPER, Janesick 2001) test. Unfortunately this cannot easily be used for the CCD201 since it contains masked areas around the image periphery that can be used for measuring the dark current. The CCD was clearly designed with Peltier cooling in mind and such reference areas are needed to stabilise the video processor in response to varying-temperature environments. The mask is an opaque layer of aluminium deposited on top of the CCD. It gives a soft edge to the image, since light can diffuse under its edge. This light-diffusion effect can be minimised by illuminating with only blue light (which has a shorter path length in silicon) but there is no manufacturer's information on the registration between the mask edge and pixel boundaries so we were unable to perform the EPER test for this CCD. Another CTE measurement method is to use Fe^{55} X-rays. When absorbed in silicon these produce charge packets of 1620e^- . By examining the height of these events as a function of image column number we can probe rather accurately the serial CTE. Likewise, by measuring how their height varies with row number we can probe the vertical CTE. As a bonus we also get to measure the system gain in e^-/ADU (defined in Section 1.3.2). CTE can vary depending on the signal level so it was thought best to measure in three regimes: high and low signals as well as the single electron level.

3.4.1 High-level CTE

A 1MBq Fe⁵⁵ source was introduced into the camera cryostat at the end of a rotary arm that allowed the X-rays to be pointed towards and away from the CCD so as to regulate the exposure level. This is shown in Figure 3.6. The source was manu-

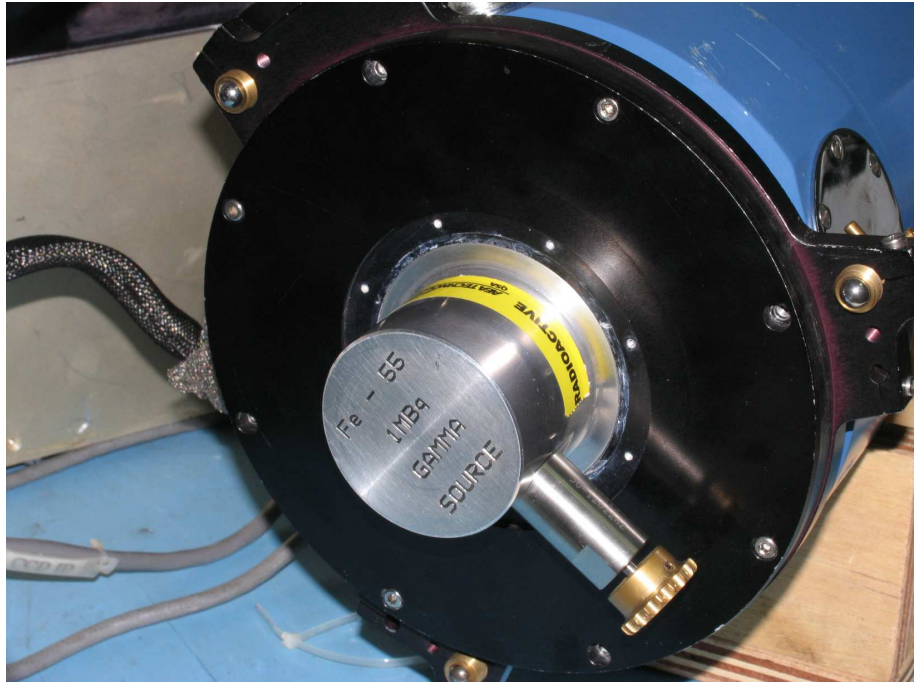


Figure 3.6: The Fe⁵⁵ X-ray source mounted on the camera.

factured in 2001 and although somewhat decayed due to its 2.7 year half-life, gave a respectable (several hundred per second) scattering of events in a 30s exposure. Most X-ray events are distributed over several pixels and are not diagnostically useful. Figure 3.7 shows the distribution of pixel values in an X-ray exposed image (readout through the normal output), plotted as a function of column number. The broad concentration of events at around 1600 ADU corresponds to X-rays that have delivered their charge in a single pixel. Since the X-ray source is not monochromatic, but instead emits X-rays of several other energies (although at much lower intensities), it is just possible to make out two other concentrations of events at around 1120 and 1760 ADU. The remaining scatter of pixel values in this diagram correspond to X-rays that have fallen close to a boundary and shared their charge amongst more than one pixel.

A line fit through the single pixel events (shown in red on the graph) can be used to determine the CTE. If the line is perfectly horizontal then the CTE =1.0. Any gradient in this line will indicate that the events on one side of the CCD will have lost charge during the transfer process due to a CTE < 1. The line fit is almost perfectly horizontal, corresponding to a CTE of > 0.999999 per transfer. A second

plot, not shown here, with event values plotted as a function of row number showed similarly excellent vertical CTE.

The system gain can also be measured from these plots. Since the Fe⁵⁵ X-rays gave a primary peak at 1600 ADU and we know that these must have contained 1620e⁻, we can then tell that the system gain is very close to 1 e⁻/ADU.

The Fe⁵⁵ method can be considered a ‘Gold standard’ since it unambiguously demonstrates any CTE problems. Note that this method could only be used to

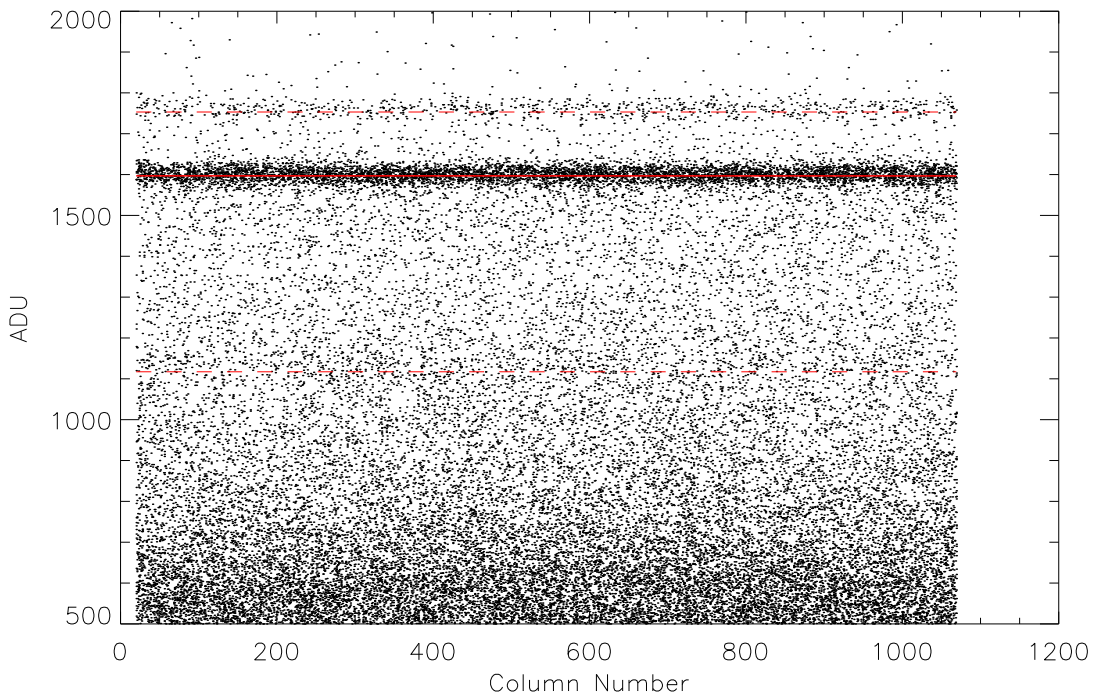


Figure 3.7: Horizontal CTE as measured using Fe⁵⁵ X-rays. The plot shows the pixel values as a function of column number. Each point represents a pixel containing charge generated by an incident X-ray.

calibrate the normal output of the CCD since 1620e⁻ exceeded the capacity of the EM register at the typical multiplication gain used with this camera. Since the EM output is only ever used for the lowest level exposures, knowledge of its high-level behavior is not really of interest anyway. A lower-energy X-ray source, generating smaller charge packets in silicon would be useful for the calibration of EMCCDs.

3.4.2 Low-level CTE

Unfortunately no lower-energy X-ray source was available, so low-level CTE was instead measured using a well focussed (FWHM <3 pixels) pinhole image. The

X-ray measurement had already established that the CTE was excellent in the high-signal regime, at least for readouts using the normal output. Any changes in the measured FWHM of this spot image, as its intensity was adjusted down from the Fe⁵⁵ level to the low-signal regime, would therefore be indicative of low-level CTE problems. The spot had the minimum size possible using the available optics. Its relatively small size ensured that any elongations induced by poor CTE would be more readily visible.

Using the normal output, multiple images were taken at peak exposure levels of 4620, 1620 (the signal produced by the X-rays), 100 and 10e⁻. Blocks of ten images were averaged together at each of these exposure levels in order to improve the signal to noise ratio. The spot images were then extracted, a Gaussian-profile fitted to them in both the horizontal and vertical axes and the FWHM of the spot images calculated.

Horizontal and vertical cuts through these illuminated spot images are shown in Figure 3.8. No degradation could be seen to levels above 1% (corresponding to a CTE in excess of 0.99999), thus confirming good low-level CTE for exposure levels down to 10e⁻ when using the normal output. Having established the good CTE

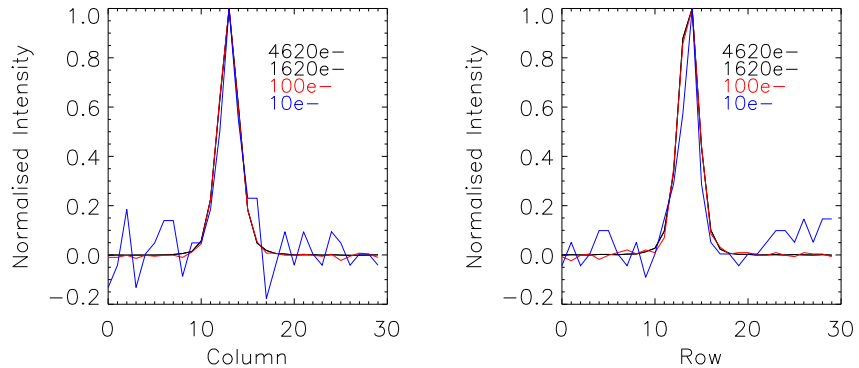


Figure 3.8: Spot-image profiles obtained using the normal output.

of the normal output, we then proceeded to measure the CTE for images obtained using the EM output. This was done by making a cross comparison of the spot profile whilst alternating between images read out through each of the two outputs. This removed any uncertainty that could arise from an intrinsically asymmetric spot profile (for example due to some aberration in the optics that causes an elongated image). Since the EM output cannot cope with large input signals, lower peak spot intensities of 10, 100 and 250e⁻ were used. The 10e⁻ spot-image readout using the normal output was observed at very low SNR since only ten frames were averaged prior to the analysis. More should have been used and no firm conclusions could be drawn from its profile. At the higher signal levels (100e⁻ and 250e⁻), though, the

Table 3.1: Spot profile parameters measured using the normal output.

Peak Exposure	FWHM_x	FWHM_y
4620e ⁻	2.61	2.53
1620e ⁻	2.59	2.52
100e ⁻	2.57	2.52
10e ⁻	2.63	2.00

Table 3.2: Spot profile parameters measured using the EM output.

Peak Exposure	FWHM_x	FWHM_y
250e ⁻	2.60	2.48
100e ⁻	2.60	2.59
10e ⁻	2.53	2.46

EM output clearly gave excellent CTE, with the spot profiles as narrow as those measured through the normal output.

Even though the pinhole image was not elongated horizontally when readout through the EM output, at least according to the Gaussian profile fits, there was some very low-level degradation of the image since a tail was clearly visible extending upstream (i.e. away from the readout amplifier) from even very faint spot images.

It can be easy to confuse poor CTE with the onset of blooming from a cursory examination of an EMCCD image. If the charge in a pixel exceeds its capacity or ‘blooming full well’ (see Section 1.2.5) then it will spill into neighbouring pixels. In an EMCCD this can easily be caused by cosmic rays or bright stellar images. A typical charge dose from a cosmic ray is 1500e⁻. A conventional CCD will have no problems transferring this quantity of charge, both vertically and horizontally. In an EMCCD, however, as the charge packet is amplified using typical gains of several hundred then it will eventually exceed the register capacity and produce image tails extending through many columns. Astronomers are quite familiar with vertical blooming from bright field stars: a conventional CCD will generally bloom vertically long before the serial register charge handling capacity is exceeded. In an EMCCD the situation is reversed: horizontal blooming commences long before vertical blooming.

3.4.3 Ultra low-level CTE

If we take a very weak flat field at a mean exposure level of 0.05 e⁻/pixel then the image will consist almost entirely of single-electron events that we can then analyse to determine the ultra-low-level CTE, at least in the horizontal axis of the image. As

an alternative to a weak flat field we can also take a bias frame shortly after a power-on reset of the chip that will contain an elevated level of image area dark current (this is generally more convenient). Parallel CTE will always appear to be perfect at this level since, in the presence of poor CTE, rather than leave a deferred charge trail the electron will simply arrive one or more rows later. The same will also be true of any poor horizontal CTE originating upstream of the EM register. The effects of poor CTE within the EM register, however, will be more obvious, producing a horizontal elongation of the single electron event. Initially these events were simply selected using a threshold filter and their profiles in the serial direction overlaid. The aim was to produce an average profile of a single-electron event. This technique did not work well since it has no way of discriminating between two single-electron events that by chance lie in adjacent pixels and one single-electron event that has later being distorted by poor CTE. An alternative method was to autocorrelate the weak flat fields. If the autocorrelation profile is then shown to be broader in the horizontal (serial transfer) direction than in the vertical direction then it will be indicative of poor horizontal CTE. This gives a somewhat qualitative result but is very useful for detecting the onset of poor CTE when optimising the clock waveforms and operating temperature of the camera (see Section 3.5). The plots shown in Figure 3.9 show the autocorrelation profiles for the camera across a range of temperatures. Note the clear broadening in the serial direction as the temperature is reduced: the serial CTE is critically dependent on operating temperature. At lower temperatures the electron mobility decreases and it becomes harder for the clock potentials to move the ever-more sluggish electrons around. The profile in the parallel direction remains consistently narrow, as expected. A quantitative measure of the CTE at the single electron level was done at a later stage in the camera optimisation by comparing actual images with synthetically generated images containing various degrees of CTE degradation. This is explained in detail in Section 5.1.1.

3.5 Dark current and operating temperature

The operating temperature was chosen very carefully for this camera in order to give optimum performance. Higher temperatures limited the performance through excessive dark current. Lower temperatures, as mentioned in the previous section, produced problems with charge transfer efficiency. One of the most important factors in camera dark current performance was the choice to run in either inverted or non-inverted mode.

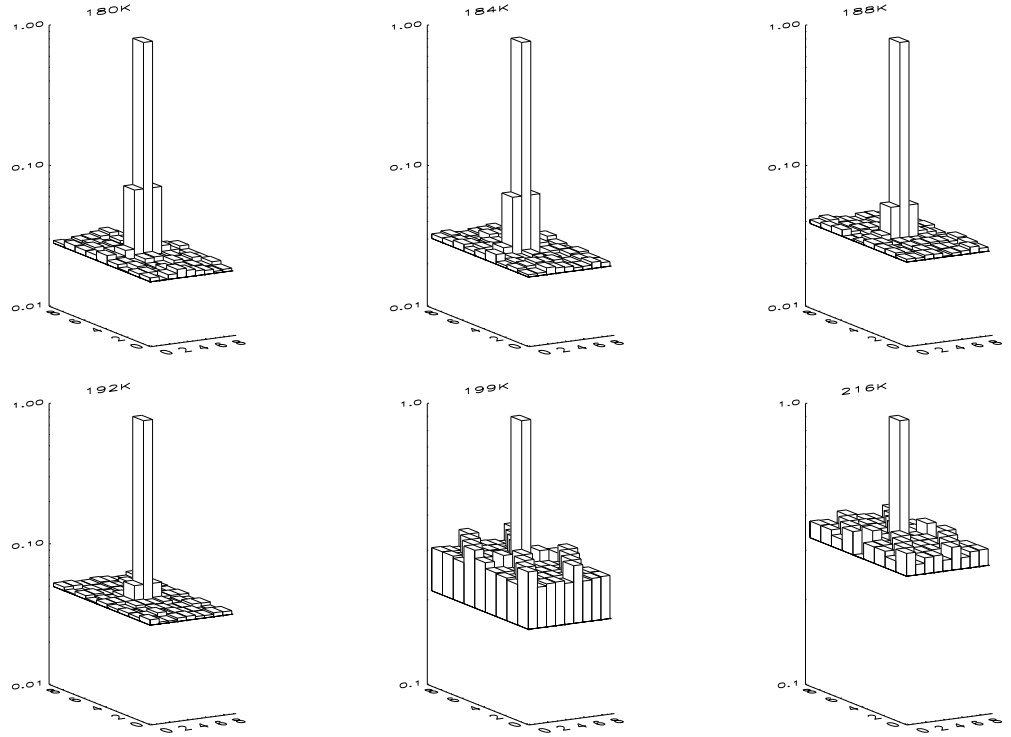


Figure 3.9: Autocorrelation of single-electron events at various temperatures. The majority of these events originate in the image area of the CCD as dark current or from low-level illumination. The X and Y axes of these plots have units of pixels. The Z axis is the normalised autocorrelation function.

3.5.1 The transition to non-inverted mode

It was necessary to reliably establish the exact conditions at which the CCD201 entered inversion. This was done using a series of short-exposure dark frames, taken at room temperature. It was more convenient to do these measurements warm since the dark current would be very high and the onset of inversion much more apparent. Between each frame in the sequence the parallel clock-low voltage was made slightly more negative and the dark current measured. Figure 3.10 shows the result. The dark current dropped steeply, as the CCD became inverted, when the parallel clock-low voltage reached $-7.5V$. In order to provide an operational margin, a clock-low voltage of $-5.5V$ was chosen for all subsequent characterisation work in non-inverted mode. Note that these voltages are expressed relative to the substrate potential of the CCD. In this particular camera, due to controller limitations, this did not coincide with the system ground.

3.5.2 Measurement of ultra-low dark currents

Measuring low-level dark current (signals in the region of a few electrons per hour) requires a lot of effort to get right, particularly in the case of an EMCCD where

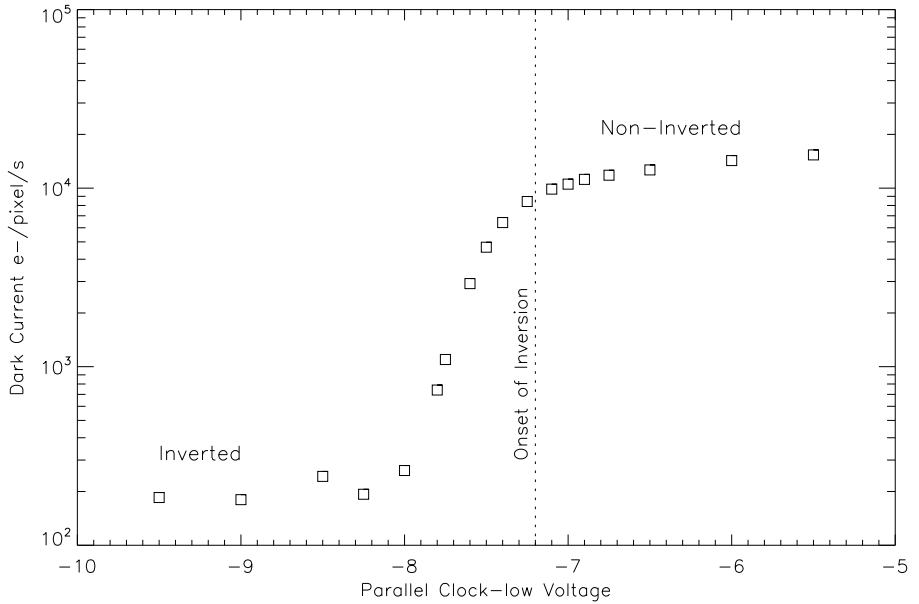


Figure 3.10: Dark current as a function of parallel clock-low voltage (with respect to the CCD substrate).

every last electron is clearly visible. First, it is important to make sure the camera *is* actually in the dark. Simply turning off the room lights (and even the light in the adjoining lab) is not enough. The room will undoubtedly contain many objects that fluoresce and have decay time-constants of minutes or even hours. Nothing short of closing off the cryostat window with a tight metal cover taped around its edges should be considered. Second, the camera should be left in a settled condition for several hours, ideally overnight, before commencing measurements. This avoids any disturbances induced by the power-on reset of the device. Third, the thermal time constant of the camera is likely to be quite long. When measuring dark current changes with temperature, the camera must be left for a considerable time (at least half an hour) at each set-point to ensure the temperature servo (see Section 2.2.1) has stabilised. Finally, an EMCCD allows the measurement of ultra-low signals but the gain mechanism itself has a strong temperature coefficient so the system must have the gain re-calibrated at each new temperature set-point prior to commencing dark current measurements.

Other noise sources such as clock induced charge and cosmic rays can easily be mistaken for dark current so these need to be separately measured and accounted for in the dark current calculations. As if the above complications are not enough, it should also be noted that dark current rate (electrons per pixel per second) is not necessarily constant with exposure time! When running a CCD in non-inverted mode and at typical Peltier cooler temperatures the dark current rate will increase significantly as the exposure time increases (see Section 3.5.6).

3.5.3 The cosmic ray background

Cosmic rays and other sources of environmental radiation contribute a significant noise current to the detector. This radiation is mainly in the form of secondary-muons generated by cosmic rays interacting with the atmosphere. The charge generated in the QUCAM2 EMCCD is approximately equal to the intrinsic dark current of the detector at the operational temperature. Cosmic ray events appear as bright spots in the image with a typical integrated charge of a couple of thousand electrons. This leads to peak signals that generally exceed the charge capacity of the EM register so cosmic rays produce ugly streaks across the image. Figure 3.11 shows this effect.

The cosmic ray rate was measured by taking an overnight series of 2 hour dark frames and then combining these images in two different ways. The first was a simple averaged combination. The dark current, ‘with cosmics’, was then measured by comparing the mean signal in the image area and bias regions of the image. The second combination method involved filtering out the cosmic rays by excluding the frames that contained either the minimum or maximum values (using the Image Reduction and Analysis Facility `imcombine` function) from the calculation of each pixel average. This almost completely removed the cosmic ray events leaving just the underlying dark current. Subtracting the ‘without-cosmics’ averaged frame from the ‘with-cosmics’ frame then yields the cosmic ray current. The result was about $0.9\text{e}^- \text{ pixel}^{-1} \text{ hour}^{-1}$.

This camera does not suffer from so called ‘hot pixels’ that have a similar appearance to cosmic rays and can be a problem with Peltier cooled cameras. This is due to its lower operating temperature.

The data was taken initially using the EMCCD output for better sensitivity to the low currents, however, it was realised that many of the events were not being properly recorded since they were above the 16-bit dynamic range of the system. Fortunately, a repeat measurement using the normal output, using longer dark frames to overcome the increased measurement noise, yielded the same result indicating that the saturation of the ADC by high value events had not in fact affected the data to a significant extent.

3.5.4 Settling time after camera reset

It took some time to appreciate the importance of allowing the CCD to settle after a power-on reset. Much time was wasted in measuring clock induced charge and dark current just a few minutes after powering on the system. It is actually necessary to

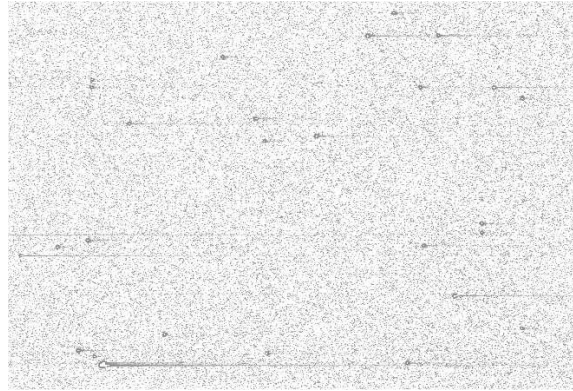


Figure 3.11: Typical appearance of cosmic rays using the EM output. Readout is to the left.

leave the camera powered-on and in darkness for at least 2 hours before embarking on any delicate measurements. Figure 3.12 shows how the dark current in the CCD at an operating temperature of 178K varied in the 4 hours following power-on. The CCD was operated in non-inverted mode and the dark current was measured using 300s exposures. Cosmic rays were excluded by hand when measuring the dark current, which bottomed out at $0.77 \text{ e}^- \text{ pixel}^{-1} \text{ hour}^{-1}$, a level low enough to be insignificant compared to other noise sources present such as cosmic rays, sky background and CIC. Given the short exposure times, the measured signal was tiny and it was important to subtract off the clock induced charge component during the calculation. This was done by measuring the difference in the signal between the image area and the serial overscan (it had already been established that the parallel CIC was negligible, see Section 3.8.2).

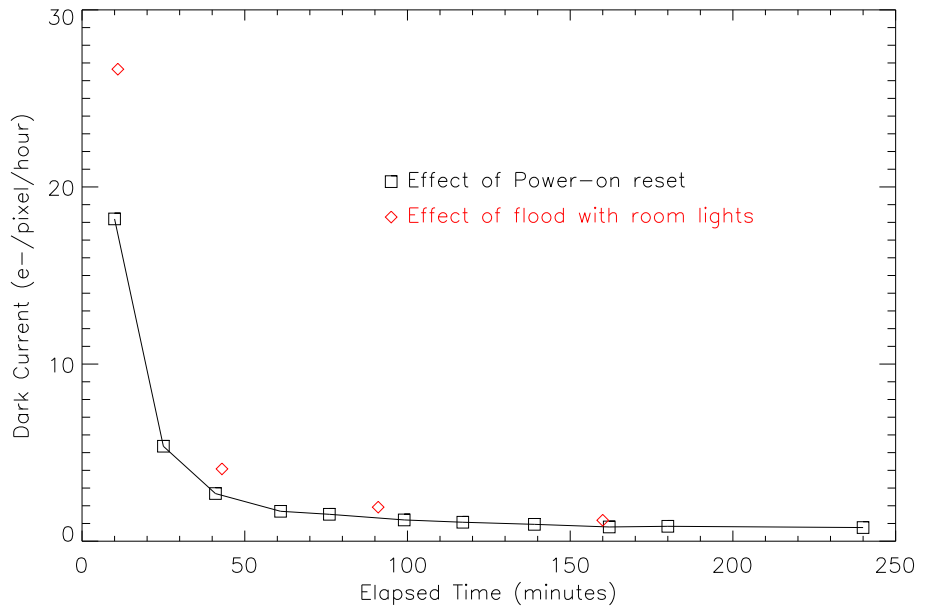


Figure 3.12: Excess dark current following power-on reset.

3.5.5 The manufacturer's dark current model

The manufacturers of the CCD publish models⁴ for the dark current of the CCD201 detector. Dark current has two main components: surface dark current and bulk dark current. The surface of a CCD is over-coated with a passivation layer, generally SiO₂. The interface between this layer and the underlying silicon generates mid-band interface states that increase the probability of a thermally excited electron reaching the conduction band. These electrons, once generated, will then fall into the potential well of the underlying pixel and contribute a ‘surface dark current’. Surface dark current can be suppressed by running the CCD inverted. This populates the surface of the CCD with holes which neutralise the dark current electrons. The second source of dark current is ‘bulk dark current’, generated deeper inside the device by electrons being thermally excited directly into the conduction band. Since these electrons do not generally have any mid-band states through which they can hop (although so called ‘hot pixels’ containing structural defects might well do), they must surmount the full band-gap of silicon. This bulk current is therefore much lower than the surface component and can be just a few electrons per second, even at room temperature. The published models give the following relationships.

$$S_B = 3.3 \times 10^6 T^2 \exp(-9080/T) \quad \text{Bulk component} \quad (3.3)$$

$$S_S = 122 \times T^3 \exp(-6400/T) \quad \text{Surface component} \quad (3.4)$$

T is the temperature in Kelvin, S_B is the bulk component and S_S is the surface component expressed in units of nA/cm². Generally speaking, one would expect a non-inverted CCD to follow the surface dark current model and an inverted CCD to follow the bulk dark current model. These relations are quoted as accurate between 240K and 300K: the typical range of a Peltier cooler. It is stated in the model that it is not as accurate at lower temperatures where it tends to underestimate the actual dark current. In the case of the bulk current, this was borne out by experiment, as shown in Figure 3.13, which compares the actual dark current measured in both inverted and non-inverted mode with the two models. Since the data were taken during cryostat cool down there would have been a lag between the detector temperature and that of its baseplate on which the temperature sensor was mounted. This lag was not measured since it would have involved gluing a sensor directly to the detector. At room temperature the models are in good agreement with the lab data, although at lower temperatures there is a clear divergence. In the case of the non-inverted data the agreement is good down to about 190K where there is a sudden drop in dark current of almost two orders of magnitude. This feature is very interesting and marks the transition between the surface dark current regime, normally

⁴E2V Technical Note 4: http://www.e2v.com/assets/media/files/documents/imaging-space-and-scientific-sensors/Papers/low_light_tn4.pdf

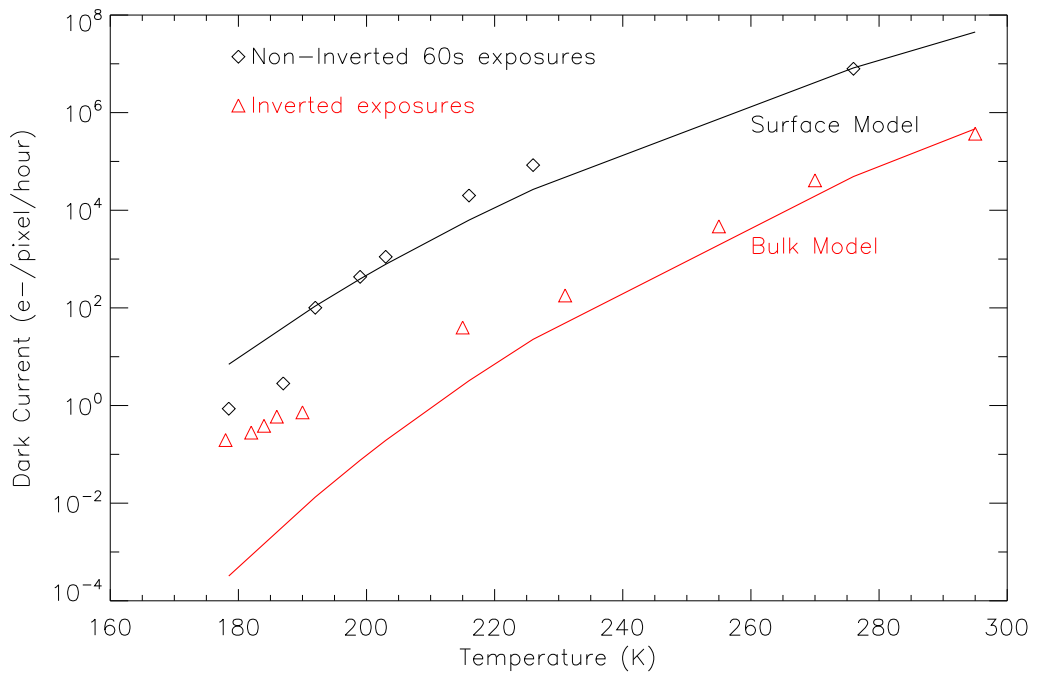


Figure 3.13: Inverted and non-inverted dark current compared to manufacturers models. The models are the continuous lines.

dominant for non-inverted mode operation and the bulk dark current dominated regime. The reason for this sudden transition is explained in the next section.

3.5.6 Dark current suppression using ‘Dither’

Dither is a term used by E2V to describe the effect of vertical clock modulation on the dark current rate (Jorden et al., 2004). It is an important effect since it allows a CCD to be used in non-inverted mode, so as to gain the advantages of low CIC, whilst at the same time avoiding the effects of increased dark current.

During the clear and readout operations of a CCD, the vertical clocks make multiple transitions between their high and low states in order to vertically transfer the charge. These transitions, even if the clocks remain non-inverted at all times, can inject holes into the mid-band surface states where they neutralise the surface dark current. The hole lifetime is strongly temperature dependent and below 193K can exceed 1 hour. Even in the Peltier regime, at 230K, the lifetime is of the order of 10s (Burke & Gajar, 1991). So, at whatever our chosen operating temperature, as long as we keep the exposure time below the hole lifetime, we should see a suppression of surface dark current. This was borne out by experiment. A series of dark current frames was taken at three different operating temperatures whilst operating the CCD in non-inverted mode. The exposure times were varied between 50s and 1000s. The parallel phases were held constant during integration. The results are shown in Figure 3.14. Note how at the coldest operational temperature of 178K the dark

current rate remained constant for exposures lasting up to 1000s whereas at higher temperatures (with their correspondingly lower hole lifetimes) the dark current rate gradually creeps up as the exposure time gets longer. It was decided to stay with 178K for the operational temperature, two degrees below that initially chosen. This reduced the dark current slightly and did not appear to impact the charge transfer efficiency.

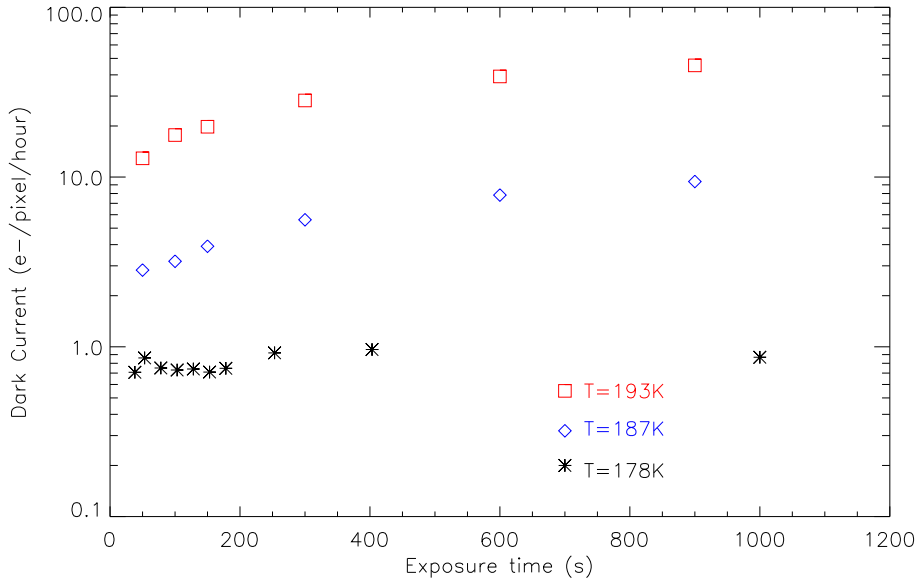


Figure 3.14: Non-Inverted mode dark current as a function of exposure time and temperature.

In the case of inverted operation, dither had no effect since there was no surface dark current component to suppress. Figure 3.15 shows that for inverted mode operation, as expected, the dark current rate was fairly constant with time, perhaps showing a slight increase for shorter exposures. This observed increase may not be real, due to the tiny dark charges accumulated during such short exposure times. For example, a dark current of $0.1\text{e}^{-}\text{ hour}^{-1}$ combined with an exposure time of only 25s produces a mean signal of less than $10^{-3}\text{e}^{-}\text{ pixel}^{-1}$ and such signals are extremely difficult to measure. In conclusion, the operating point of 178K is well chosen in that it gives fully acceptable dark current performance for the camera regardless of whether we operate in inverted or non-inverted mode. The hole lifetime at this temperature is long enough to give a constant dark current rate for all practical exposure times. Additionally, if we are using Peltier-cooled devices, which are generally designed for inverted mode operation, we should be very careful in our measurements of dark current: using a long dark frame to calibrate dark current may give an extremely pessimistic result (by as much as 2 orders of magnitude!) if the camera is intended for high frame rate applications, for example wavefront sensing (WFS). This can be demonstrated using the data presented in Figure 3.14. Suppose we operate our CCD at 193K and measure dark current using 600s exposures. We might think that

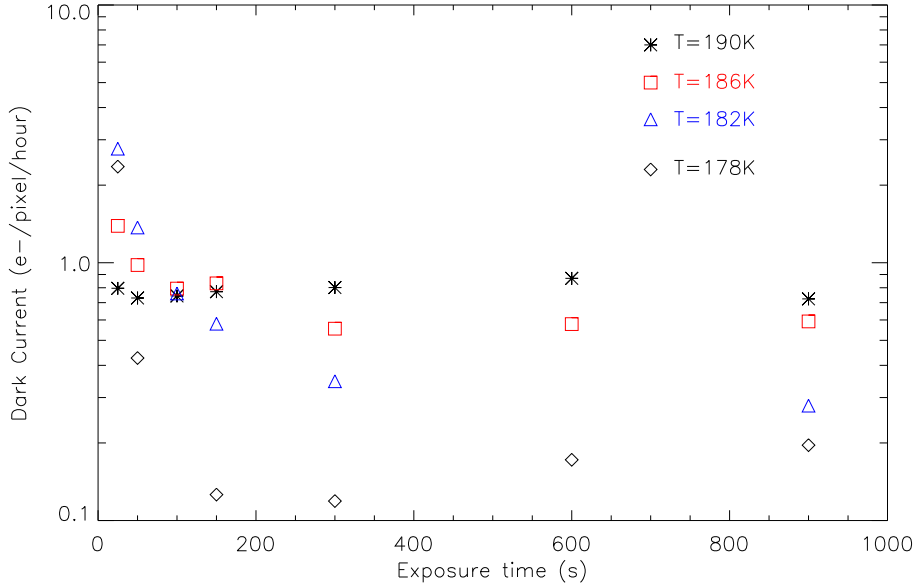


Figure 3.15: Inverted-mode dark current as a function of exposure time and temperature.

the dark current is $40\text{e}^-/\text{hour}$ using this graph. In fact the actual dark current is much lower at operational frame rates. At 50s exposure times the dark current has already fallen to $12\text{e}^-/\text{hour}$ and will likely fall further at the multi-Hz frame rates typical of a WFS.

3.5.7 Residual image

Residual image can be caused by extreme over-exposure and leads to image ghosts in subsequent frames. In thinned CCDs, such as the CCD201 used in this project, the residual image arises from charge overflow from an integrating pixel reaching the surface of the CCD. Once at the surface this can be trapped in mid-band interface states, from where it then slowly leaks back into the underlying pixel. The time-constant of this leakage can be many hours at cryogenic operating temperatures. Residual image can therefore be thought of as a kind of excess dark current whose magnitude is dependent on the elapsed time since the over-exposure event. The solution according to theory is fairly straightforward; the surface interface states can be discharged by momentarily inverting the CCD thus driving holes from the channel stops into the surface region where they neutralise the trapped charge.

Residual image was measured by exposing the CCD to progressively higher levels of over-exposure and then following each exposure by a series of short dark frames. Since the over-exposures exceeded the saturation limit of the camera the actual levels of exposure had to be calculated. A stable LED light source was used whose brightness was measured using short non-saturating exposures. The light it delivered for the longer exposures could then be easily calculated by simple ratioing of the

exposure times. It was noted that residual image became much worse as soon as the over-exposure produced a bloomed image (corresponding to the surface full well being exceeded). Image blooming is described in Section 1.2.5. Figure 3.16 shows the effect. Note the sudden jump in the remnance dark current between over-exposure levels of 150ke^- and $225\text{ke}^- \text{ pixel}^{-1}$. Since during these measurements the camera may have seen some very low-level fluorescence in the lab, the absolute values of dark current are not accurate and the figure serves only to show the discontinuity in remnance dark current when surface full-well capacity is exceeded. It is therefore very important to guard the CCD against over-exposure by continual flushing of the image area during idling. This minimises the chances of inadvertent over-illumination (from dome lights for example) causing the full well to be exceeded.

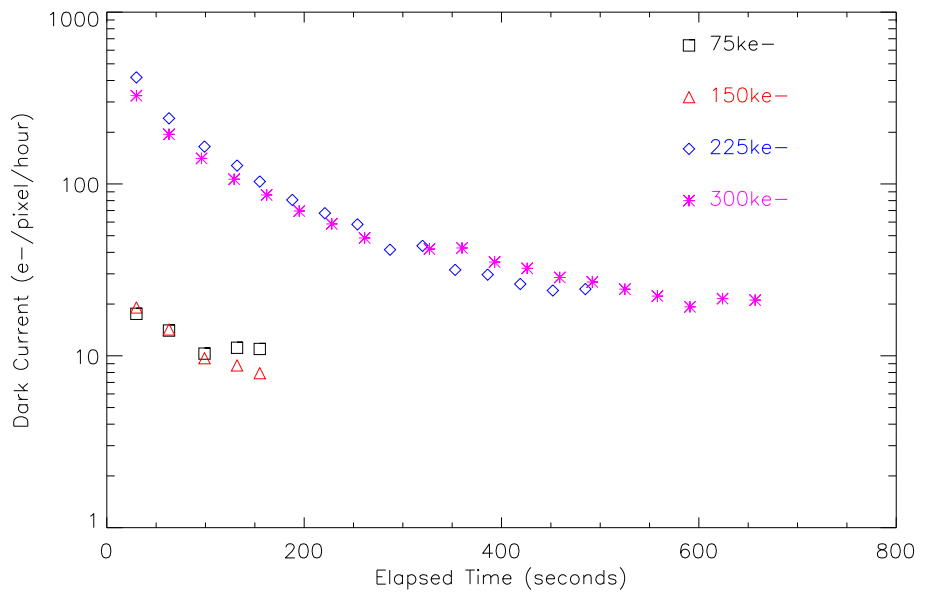


Figure 3.16: Effect of increasing over-exposure levels on remnance dark current. Note the sudden increase once the exposure level exceeds $150\text{ke}^- \text{ pixel}^{-1}$. At the two lower exposure levels the dark current was only measured up to 150s after the illumination event since by then the trend in the data was clear.

The CCD was also crudely flooded with room light and the residual dark current measured as a function of time. The decay curve, shown in Figure 3.12, indicates that the dark current closely matched the response of the CCD to a power-on reset suggesting that the same mechanism underlies both effects: population and subsequent decay of mid-band interface states at the surface of the CCD.

3.6 Charge-handling capacity and dynamic range

A brief look at the camera linearity using the normal output of the CCD revealed no saturation and blooming in the image up to the 16-bit limit of the ADC. To further study the charge handling capacity of the CCD it was therefore necessary to reduce the voltage gain of the video amplifier so as to extend the maximum pixel signal. This was easily done for either CCD output by modifying a programmable gain amplifier on the video board and by reducing the integration time of the signal integrator by a factor of two. An extended illuminated target was used to produce a large number of evenly-illuminated pixels within a window on the chip measuring approximately 100x100 pixels. The exposure was gradually increased and at each level the mean and variance of the signal in the window was recorded. Pixel-to-pixel variations in sensitivity can affect the statistics, so at each exposure level it was necessary to record *two* frames and then subtract one from the other to calculate the variance. This canceled out any intrinsic pixel-to-pixel variations but had the side effect of doubling the variance in the signal. The value of the variance divided by two was then plotted against the mean signal level in what is known as a ‘photon-transfer curve’ (Janesick 2001).

Figure 3.17 shows the result for the detector operated in non-inverted mode. The graph gives us two useful pieces of information. Firstly the gradient of the graph in its linear region is equal to the system gain in e^-/ADU . Secondly the mean signal level at which the graph starts to diverge from a linear response corresponds to the onset of ‘surface full well’. At this level, which in non-inverted mode occurs at $75e^-$, the charge packet begins to interact with the Si-SiO₂ interface at the CCD surface. This interaction produces some charge recombination and loss of signal but does not necessarily result in any visible blooming of the image. The so-called ‘blooming full well’ occurs at somewhat higher signal levels.

Blooming full well was investigated using a pinhole image so as to make more obvious the onset of blooming. The exposure level was gradually increased until vertical blooming of the image became clearly visible. In inverted mode this occurred at an exposure level of between $75e^-$ and $80e^-$. In non-inverted mode it occurred at between $140e^-$ and $210e^-$. This is to be expected since in inverted mode the clock-high level on one of the vertical phases acts to better constrain the charge within each pixel. The actual bloomed images are shown in Figures 3.18 and 3.19. Note the charge trails only into rows above the illumination site (the readout direction is towards the bottom). A proportion of the electrons reaching the CCD surface become trapped and then, over the course of a few tens of milliseconds, leak back into the active region of the detector, contributing to the charge in subsequent readout rows and so producing the vertical trails. Note that when these images

were taken the normal amplifier was used. This meant that the image area full well was the limiting factor. If instead we had used the EM output this would not be the case and the EM register would saturate long before the image area.

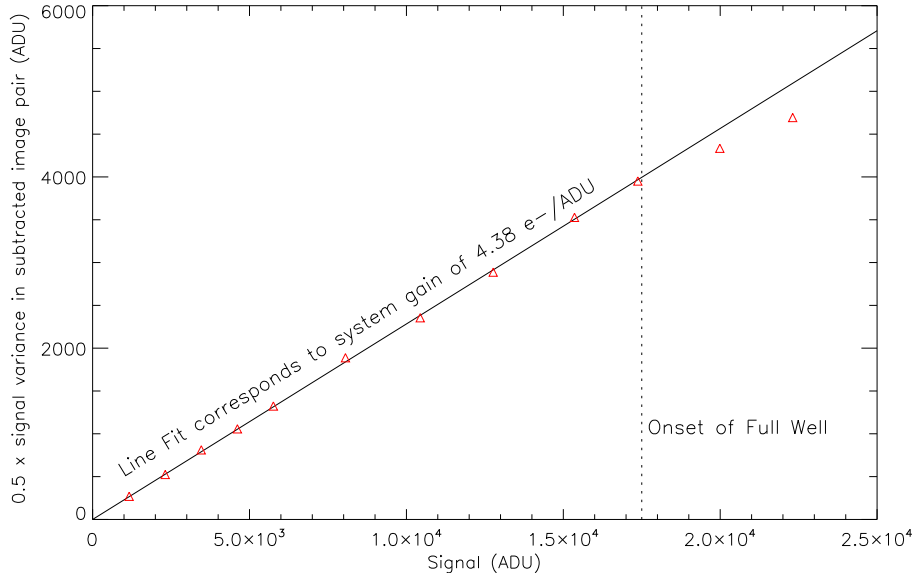


Figure 3.17: Measurement of the image-area full well capacity in non-inverted mode.

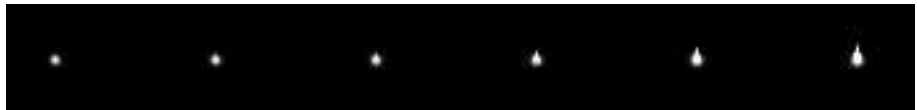


Figure 3.18: Vertical blooming in inverted mode. From left to right, the exposure levels vary between 64 and 142ke⁻.

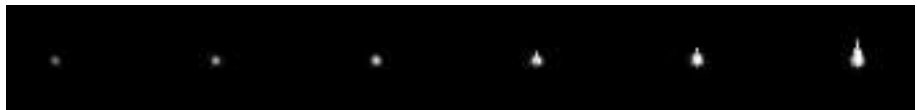


Figure 3.19: Vertical blooming in non-inverted mode. From left to right, the exposure levels vary between 70 and 430ke⁻.

If we use the EM output as the exposure is increased, the image will first bloom horizontally as the EM register reaches maximum charge. According to the data sheet this occurs at $750\text{ke}^- \text{ pixel}^{-1}$. Although this is an order of magnitude greater than the full well of the image area, it needs to be divided by the multiplication gain g_A to convert the units to input referenced image area photoelectrons. These are more convenient units to discuss since they show what the maximum exposure level, in terms of photoelectrons, that the device can handle. At typical EM gains the EM output will produce images that bloom horizontally long before they bloom vertically.

The capacity of the EM register was tested in the laboratory using a pinhole image of varying brightness. Due to the low signal levels it was actually necessary to take 10 pinhole images at each exposure setting and average them together prior to analysis. The spot images themselves are shown in Figure 3.21. As with the normal output measurements, it was also necessary to reduce the gain of the video processor in the controller so as to be able to deal with higher signal levels. It would also have been possible to reduce the multiplication gain but this was not done, since the effect of multiplication voltage on the EM register capacity was not known. The new system gain was then accurately measured using the histogram technique described earlier (see Section 3.2). The cross-section of the spot image was then measured at various brightness levels as shown in Figure 3.20. The spot was not particularly well focussed and its image had a flat top with some structure. This structure actually proved rather useful in interpretation of the images since it became indistinct just prior to the onset of blooming. It can be seen that above 220k e⁻ (referenced to the *output* of the EM register) the structure in the spot image starts to disappear. The multiplication gain of the EM register in this measurement was $\times 400$ so the EM register full well is equivalent to 550 input-referenced photoelectrons. So the measured charge capacity of the EM register (220ke⁻) was about a factor of three lower than quoted in the data sheet (750ke⁻). This could be explained by non-optimal clock shaping. In conclusion, this measurement shows that it is the EM register capacity that places a limit on the dynamic range of this CCD and image area full well is at least two orders of magnitude greater than required.

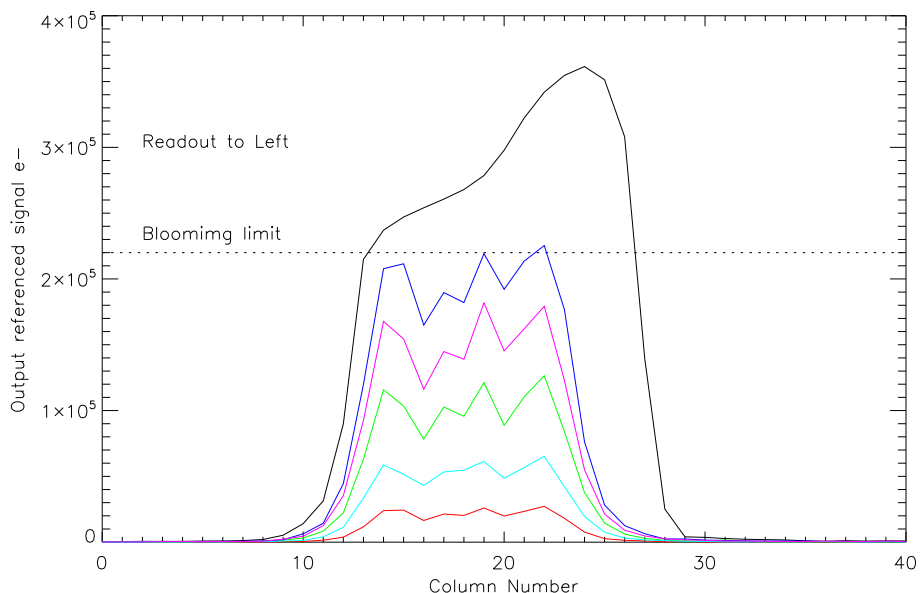


Figure 3.20: Horizontal profile of a spot image of varying intensity.

So image area full well is not an important parameter if we restrict ourselves to the EM output: it is the EM register that places the limit on the maximum exposure



Figure 3.21: Increasing image brightness leading to horizontal blooming in the EM register.

level. If we use the normal output this is not the case and knowledge of the image area full well is as important as it is for a conventional science CCD.

3.7 Amplifier linearity

The linearity of both outputs of the detector was measured using an external LED light source mounted on the faceplate of the camera. This provided a more direct illumination of the CCD. The drive current of the LED was low enough to prevent significant self-heating and so maintained a linear relationship between the LED on-time and the number of photons it delivered to the detector. The LED was interfaced to the camera controller and a series of exposures taken with steadily increasing LED on-times. When using the EM output it was necessary to add a neutral density filter in front of the illuminating LED. Figure 3.22 shows the response of the normal output. The EM output was briefly measured and was linear to within $\pm 5\%$ at signal levels up to 45k ADU. At this stage only a brief confirmation of an acceptable linearity was needed so as to diagnose any gross problems. Amplifier linearity for both outputs was measured more thoroughly at later stages in the optimisation of the CCD (see Section 4.3).

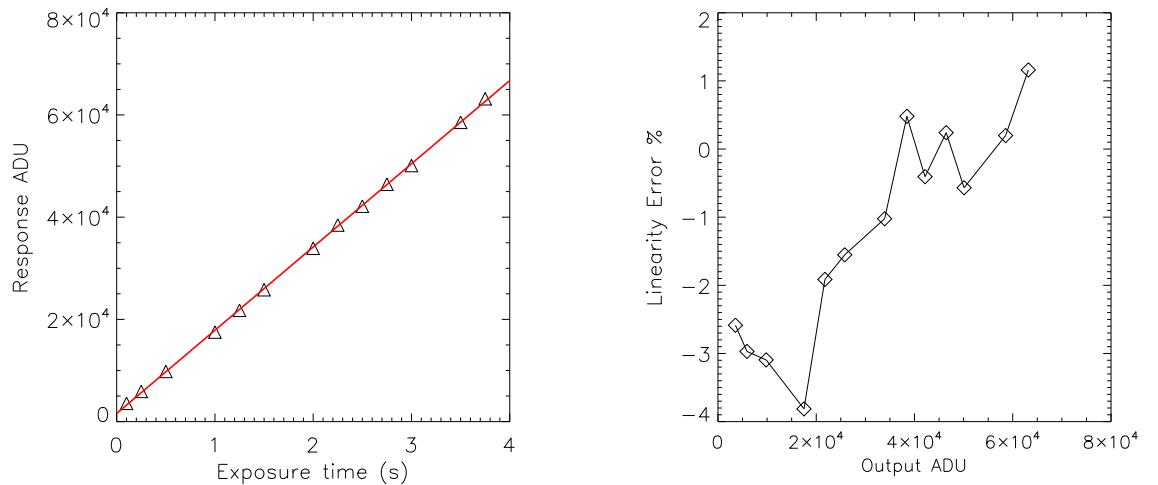


Figure 3.22: Linearity of the normal output.

3.8 Measurement of CIC

In measuring CIC we first need to subtract off the bias level from the image and then convert from ADU into units of electrons. For this we need to know accurately the system gain. A method for accurately measuring the gain has already been explained in Section 3.2. Measuring the bias in a conventional CCD is easy: it corresponds to the mean value of the bias region. This region should ideally be an overscan region (see Section 1.4), since the underscan is often affected by large transients induced by the vertical clocking and can contain a gradient of many ADUs. For an EMCCD things are more complicated since the bias regions of the device will still contain CIC events. In order to exclude the disturbance of these events and get to the true underlying bias level we need instead to measure the *median* pixel value of the whole image (once again avoiding the edges, where bias-gradients may be present). This median value is then subtracted off and the mean value of the resultant image converted into units of electrons which is then equal to the mean per-pixel CIC.

CIC measurements should only be attempted on images without bias gradients and with low read-noise. CCD images can contain bias gradients of a few ADU. If we wish to measure CIC to an accuracy of 0.01 e^- and the system gain is say $0.01\text{ e}^-/\text{ADU}$, then a bias gradient of just 1 ADU across the measurement window will frustrate our efforts. Much time was wasted before this was appreciated. In the end the CIC was only measured across a small window (less than 200x200 pixels) at the centre of the image across which the bias was flat.

3.8.1 Inverted mode CIC

It was immediately obvious from the bias frames that the level of CIC from the parallel clocks was very high. The serial underscan region of the chip could be easily discerned, especially when a large number of biases were summed. The pixel values in the underscan were much lower than the image area. Since these pixels never had image area charge transferred into them, they contained only CIC generated in the serial register, which in this case was at a much lower level. The image area pixels contained CIC contributions from both the serial and parallel transfers. We then calculated the CIC generated in the parallel transfer by subtracting the mean in the serial underscan from the mean in the image area. In doing this, care must be taken to avoid using underscan pixels very close to the image periphery which have a significant gradient. This gradient is caused by the parallel clocking disturbing the substrate potential of the CCD. The CCD and the video processor then take several pixel times (this being the time taken to read out one pixel) to recover from this transient effect. It is also essential to measure the dark current and subtract it

off since it is easily confused with parallel CIC. The parallel CIC was in fact so high that Poissonian statistics showed that a significant number of pixels contained more than one electron. This required special care in interpretation of the gain calculation program output which underestimates the e^-/ADU gain by 5% in this case (see Section 3.2). This gain program relies on the event height distribution of pixels containing single electrons. Multiple-electron pixels have an entirely different height distribution and the program no longer gives an accurate result. The inverted-mode CIC from all sources was in the region of $0.11e^-/\text{pixel/frame}$.

3.8.2 Non-inverted mode CIC

Operating the CCD in non-inverted mode produced a dramatic drop in parallel CIC. The serial underscan was no longer visible, even in a stack of 300 summed bias frames, since the CIC it contained was equal in magnitude to that in the image area. This told us that we were now dominated by CIC generated within the serial and EM registers. Some parallel CIC may have also been present but it was so swamped by the serial contribution as to be invisible. The CIC measured in input referenced photoelectrons was found to be $0.03e^-/\text{pixel/frame}$.

So great was the advantage of running non-inverted that it was decided to abandon inverted mode operation, especially having established that there would be no dark current penalty in doing so (see Section 3.5.6).

3.9 High and low-level flat fields

Flat field exposures are best done by pointing the camera into an integrating sphere. Since none was available it was necessary to improvise. A reasonably good flat field was obtained by placing a diffusing screen over the front of the camera cryostat and placing a faintly illuminated white screen 50cm in front of it.

The exposure levels were adjusted using a combination of neutral density filters, variations in the brightness of the light source and variations in the exposure time. Three sets of flat fields were then taken at mean exposure levels of $1e^-$, $10e^-$ and $1000e^- \text{ pixel}^{-1}$. The first two of these were read out via the EM output, the last through the normal output. The purpose of this was to show up any low-level image defects, for example blocked columns, that may not be immediately obvious in high-level test frames. In the case of the $1e^- \text{ pixel}^{-1}$ exposures, 50 separate flats were taken and averaged together so as to improve the SNR. For the other two sets, only 25 frames were averaged together at each exposure level. To further

improve the SNR, the averaged frames were fully binned in the y axis to produce a 1D average. These average profiles were then normalised and plotted together in Figure 3.23. For clarity a small vertical displacement has been introduced to separate the plots. These horizontal cuts through the flat field images reveal a very

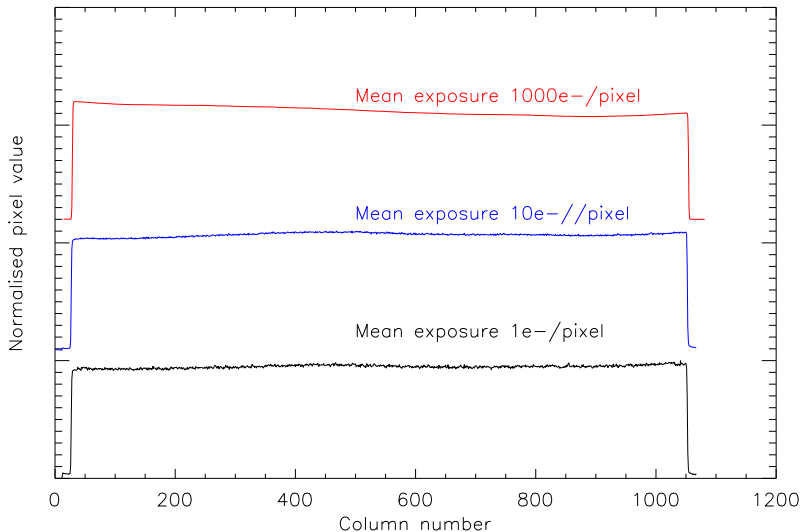


Figure 3.23: Horizontal cuts through flat field images at several exposure levels

clean response with no blocked columns. Note the unilluminated regions at the image edges. These are either dark-reference columns that lie beneath the light shield or serial under/overscan columns.

3.10 Summary of initial setup conditions

The state of the camera at the end of the initial characterisation process is now summarised here. It is this state that the camera was used for the astronomical observations detailed in Chapter 7.

Table 3.3: Initial performance of camera. The CDS times are quoted to indicate the length of time taken to sample the reference and then the signal part of the waveform. Note that a more comprehensive list of the parameters obtained during later fine-tuning of the camera can be found in Table 4.1.

Pixel time total (EM amplifier)	$3.3\mu\text{s}$
Pixel time CDS (EM amplifier)	$1+1\mu\text{s}$
Pixel time (normal amplifier)	$5.1\mu\text{s}$
Pixel time CDS (normal amplifier)	$2+2\mu\text{s}$
Frame transfer time	13ms
Row transfer time	$12\mu\text{s}$
Full frame read (EM amplifier)	3.6s
Full frame read (normal amplifier)	5.4s
System gain g_{S0}^* (EM amplifier)	$2.4\text{e}^-/\text{ADU}$
System gain g_S (normal amplifier)	$0.97\text{e}^-/\text{ADU}$
EM multiplication gain g_A	380
Read-noise (EM amplifier)	20e^-
Read-noise (normal amplifier)	4.0e^-
Mean charge in bias image	$0.03\text{e}^- \text{pixel}^{-1}$
Cosmic ray rate	$0.9\text{e}^- \text{pixel}^{-1} \text{hour}^{-1}$
Image area dark current	$0.77\text{e}^- \text{pixel}^{-1} \text{hour}^{-1}$
Parallel CTE (per transfer)	> 0.999999
Serial CTE (per transfer)	> 0.999999
Image area full well	140ke^-
EM register full well	220ke^-
Linearity (EM amplifier)	$\pm 5\%$ to $45\text{kADU}/280\text{e}^-$
Linearity (normal amplifier)	$+1/-4\%$ to $65\text{kADU}/63\text{ke}^-$
Operating temperature	178K
Operating mode	Non-inverted

* see Section 1.3.2

Chapter 4

Fine tuning of camera performance

The initial set up of the camera was done using the manufacturer's data sheet ¹. This gave a set of bias voltages and clock configurations most suitable for general operation. Many of the performance parameters in the data sheet are defined for operation at TV frame rates (10s of Hertz) and at the typical temperatures obtained using Peltier cooling ($\sim 250\text{K}$). In our application – sub-Hertz frame rates with the emphasis on ultra low noise, a more optimised set-up was sought.

4.1 Reduction of the clock induced charge

The clock induced charge was identified early as being the limiting noise source in the camera, dark current not being an issue at cryogenic temperatures and read-noise being rendered insignificant by the avalanche multiplication gain. Almost all the optimisation work was therefore centred on reducing the CIC through various means. This work was spurred on by a study of low-CIC bias frames provided by two other researchers: Derek Ives at UKATC and Olivier Daigle at the Université de Montréal. The former provided bias frames that contained a charge (assumed to be solely CIC) of $0.01\text{e}^- \text{ pixel}^{-1}$, the latter sent images that contained only $0.003\text{e}^- \text{ pixel}^{-1}$ but there remains some uncertainty in this figure as the biases contained very large amounts of pattern noise that could have distorted the measurement.

¹E2V CCD201 data sheet: http://www.e2v.com/assets/media/files/documents/imaging-space-and-scientific-sensors/A1A-100013_2_v1.pdf

4.1.1 Use of non-inverted mode

The manufacturers of the CCD quote in a technical note² that using non-inverted mode can reduce the CIC by two orders of magnitude. In normal inverted operation the parallel clocks when in their low state are well below the substrate voltage. In this state the clocks attract holes from the channel stop regions and these then accumulate at the surface of a pixel under the oxide layer. When a clock then rises positive with respect to the substrate, as it must during the charge transfer process, these holes are kicked back into the channel stops and they produce electrons through impact ionisation. Although the probability of this happening in any single clock transition is small, the effect becomes significant after a pixel has been transferred several thousand times on its journey from image site to output amplifier. According to Janesick (2001) the magnitude of this effect is dependent on the positive slew rate of the clock edge, the clock amplitude and also the time for which the clock remains high. If the clocks are kept permanently non-inverted, which typically means ensuring they never go more than 6V below the substrate, then the hole and subsequent CIC generation should not occur. According to E2V, CIC generation should not be present in the serial register since its clocks are permanently non-inverted. Non-inverted mode did, as predicted, bring about a large reduction in parallel clock generated CIC. Indeed it rendered it so low as to be unmeasurable, i.e. the signal visible in the serial underscan (see Section 1.4) of a master frame composed of as many as 300 summed biases was no different from that in the image area. Oscilloscope traces of the parallel area clocks are shown in Figures 4.1 and 4.2 for inverted and non-inverted modes, respectively. The substrate potential in both cases was 4.5V. It was at this stage of development, operating in non-inverted mode with the CIC $\sim 0.03e^- \text{ pix}^{-1}$, that the camera was used on the telescope for the observations described in Chapter 7. All subsequent results presented in this thesis were obtained in non-inverted mode.

4.1.2 Tuning of serial clock waveforms

The manufacturers claim that there is no serial-register CIC since its clocks are never inverted. This was found not to be the case and even with the parallel clocks in non-inverted mode CIC was visible everywhere in the bias frames. The fact that the summation of as many as 300 bias frames did not reveal any difference in the level between the image area and the serial underscan (see Section 1.4) indicates that the events originate in the serial register or the EM register or both. Note that if the CIC is only created by the parallel clocks then the serial under and overscan

²E2V L3 CCD technical note 4: http://www.e2v.com/assets/media/files/documents/imaging-space-and-scientific-sensors/Papers/low_light_tn4.pdf

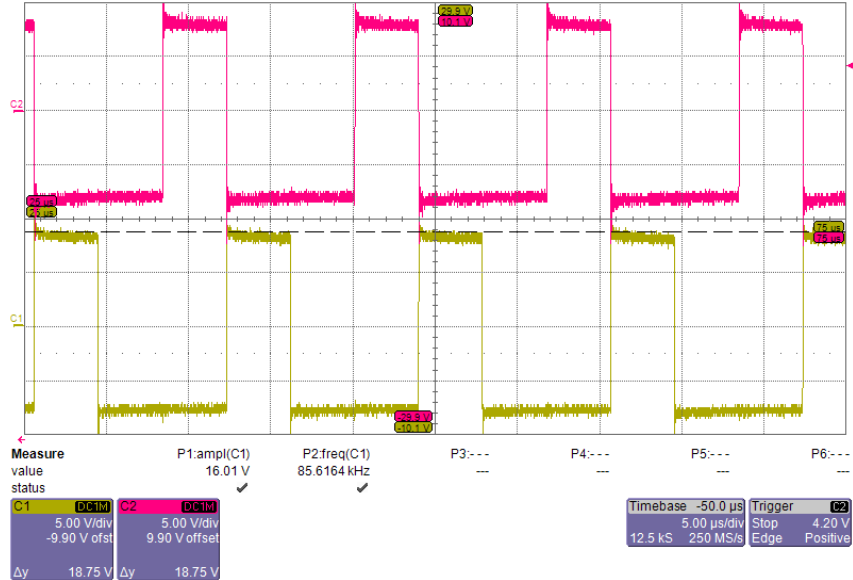


Figure 4.1: Parallel clock phases in inverted mode. The small trace markers C1 and C2 on the vertical axis at left represent zero-volts. The traces show the waveforms applied to the parallel clock phases during readout of the CCD. During integration, both phases will be in their low states. As shown in the figure this is $\sim 8.5\text{V}$ with the substrate at 4.5V.

regions should be empty of CIC. Initially it was thought, given the higher voltages present in the EM register, that it must be the source of serial CIC. If true this would be a depressing result since there is little flexibility in reducing the HV clock swing, so as to reduce the CIC, without directly affecting the EM gain.

To try and confirm this hypothesis an experiment was devised involving the use of the dump gate (DG). This structure on the CCD (the CCD geometry is described in detail in Section 1.3.1) allows the contents of the portion of the serial register that lies immediately adjacent to the store area to be emptied of charge. Its normal application is in the rapid clearing of the CCD prior to an exposure. In this experiment it was instead used to clear the first part of the serial register prior to serial readout. This will of course produce empty images since any signal charge from the store area is effectively erased. However, this is of no importance since the experiment was carried out in total darkness so as to make the CIC more easily visible. If one assumes that CIC is generated only in the EM register then the dump gate should make no difference to the measured CIC. If, however, some of the CIC is generated in the serial register then the use of the dump gate should produce a horizontal gradient in its magnitude. For the DG to be effective it was necessary to hold all the serial clocks in their low state for several microseconds. This drives the charge into the DG structure but also corrupts signal already present downstream in the pipeline (see Figure 1.8 for a description of the pipeline). The corruption occurs because with all serial phases low there are no potential wells in which to confine the photo-charge. There will be nothing to define the edges of each pixel element

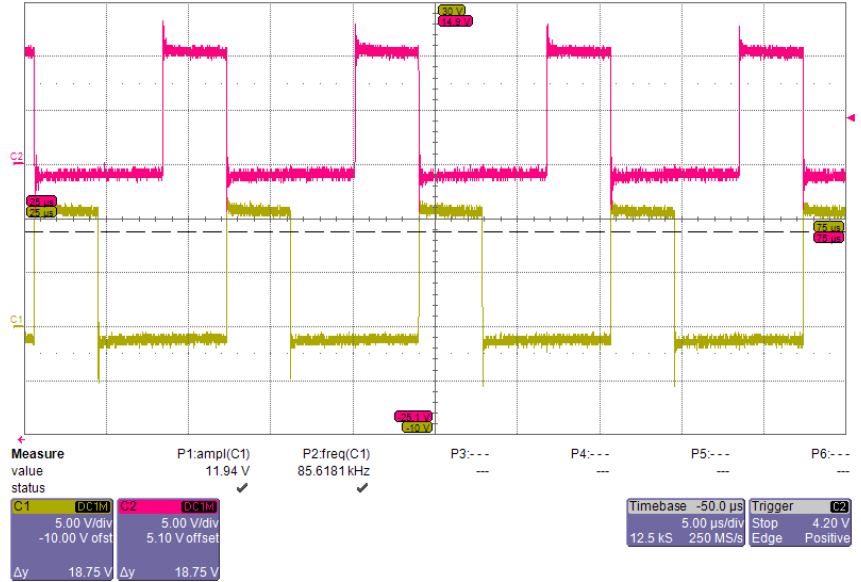


Figure 4.2: Parallel clock phases in non-inverted mode. The clock-high voltages were further reduced to 8V when reading out images through the EM output. In this mode the clock-low voltages are ~ 1 V and the substrate was at 4.5V.

and charge will be able to flow freely from one element to its neighbours. In the case of the EM register this may not be entirely true since it still has the applied potential of the $R\phi DC$ phases to separate adjacent elements. If, however, we read out the entire pipeline for each row read there should be no corruption of the part of the image that really interests us: that part adjacent to the dump gate.

The reason for the horizontal CIC gradient can be difficult to understand and requires some explanation. At first sight, one may assume that, since CIC is proportional to the total number of clock transitions a pixel experiences during the readout process, a pixel lying far from the readout amplifier should experience a higher level of CIC. One should then expect CIC gradients in both the horizontal and vertical axes of the image. This would be true if the CCD was entirely cleared of charge prior to each readout. However, this is never the case. One must consider that prior to each readout the chip has either been flushed in a clear operation or read out in a previous exposure (Figure 4.3 illustrates this). These operations leave a ‘history’ of CIC events in the CCD pixels prior to our subsequent measurement readout. The distribution of these historical events will be highest the closer we get to the readout amplifier since the CIC charge residing in these pixels will have accumulated through a larger number of clock transitions than for pixels more distant from the amplifier. When these historical events are added to the events created in our measurement readout the overall effect is that each pixel of the image will have experienced the same number of clock transitions regardless of its position and the CIC distribution will be flat. This rule is subverted by the DG operation which removes the historical events.

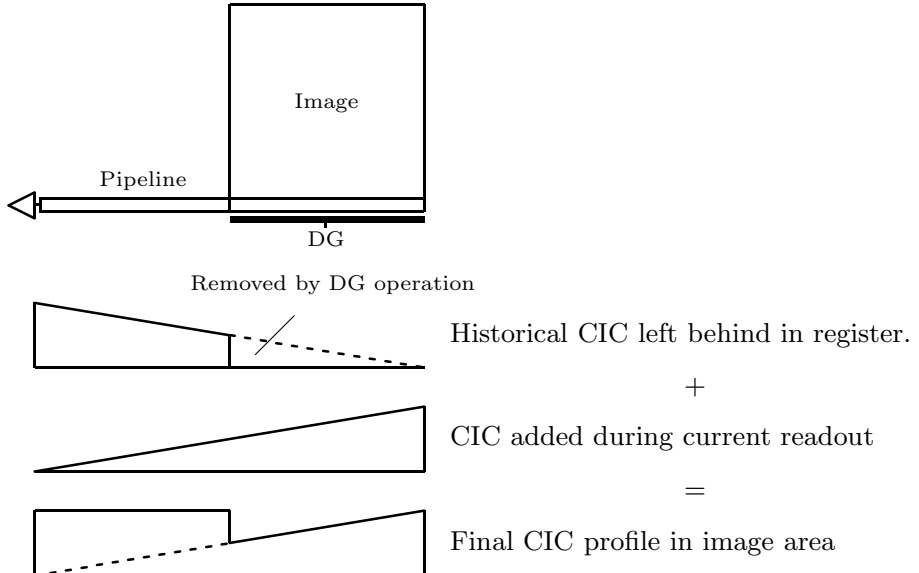


Figure 4.3: Effect of dump gate on CIC distribution. DG activation induces a slope in the serial CIC events.

For the dump gate experiment the horizontal readout dimension of the chip was extended from its normal 1080 columns to the full length of the EM + serial registers, i.e. 2160 pixels. Each line of readout then entirely emptied the pipeline. Due to the tiny signals (at the start of optimisation each pixel contained on average $0.03e^-$ of charge) a large stack of bias frames was then taken. These images were first bias subtracted (the bias being equal to the median pixel value) and then co-added. The resultant master bias was then fully binned in the vertical direction and the pixel values converted into units of electrons (the conversion factor being measured from some weak flat fields obtained with the dump gate disabled using the histogram technique described in Section 3.2) and plotted as a function of column number. Such a graph is shown in Figure 4.4. The section of the graph that corresponds to the serial pixels lying next to the dump gate clearly shows the expected gradient. A line fit to this gradient is also shown extrapolated in the direction of the origin. The gradient of the extrapolated line when the higher clock level was equal to 10V was 5.5×10^{-6} which gives us the CIC in e^- generated per serial pixel transfer. Since the pipeline is 1540 elements long this indicates a total serial CIC signal, ν_{CS} , of $0.0085 e^- \text{ pixel}^{-1}$ originating in the non-EM parts of the serial pipeline. This is equal to about 30% of the total CIC.

The technique of manipulating the dump gate proved very useful in the next stage of optimisation which was to modify the serial clocks in an attempt to reduce the CIC. These modifications involved reducing the serial clock swings to see the effect on the CIC. Since these modifications could also impinge on the CTE it was necessary to monitor the profile of the CIC events after each change using the autocorrelation technique described in Section 3.4.3. As a start, the high-level voltage of the serial

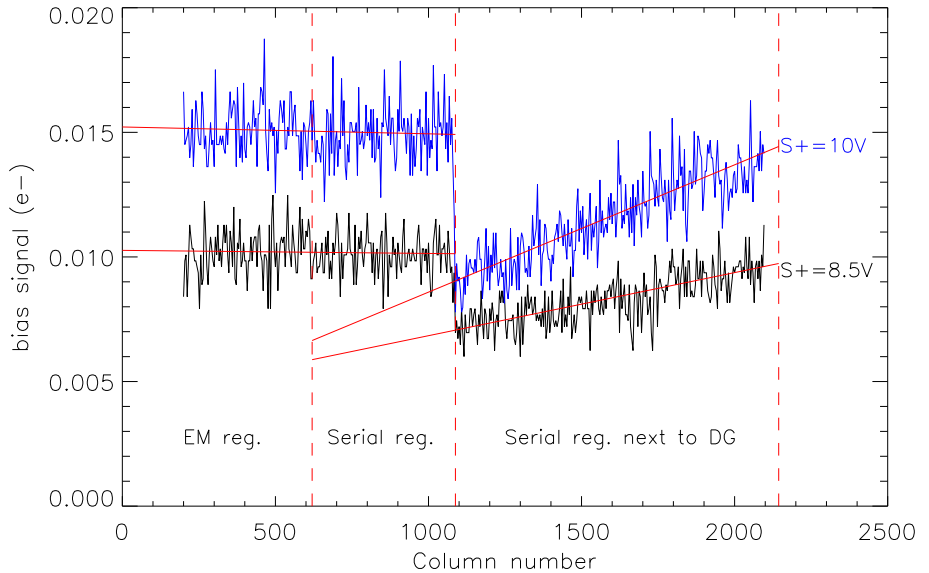


Figure 4.4: Use of the dump gate to measure serial generated CIC. Here the lower serial clock level was 0V and the graph shows the CIC profiles for two different upper clock level values. The $S+$ voltages labeled on the plot refer to the positive serial clock levels. The substrate voltage was 4.5V.

clocks were reduced in steps of 0.5V until the CTE degradation was visibly affected. Further reduction in the serial clock swings gave very poor CTE, where the tails in the single electron events exceeded 10% of the peak. It was found that this could be partly recovered by dropping the clock-low voltage. Experiments were also performed to increase the overlap between the serial clocks in an attempt to improve CTE and allow further drops in clock amplitude. These were not successful. Some adjustments were made to the OG and $R\phi DC$ bias electrodes (see Section 1.9 for details of the CCD geometry) which are also present within the serial pipeline and must affect the charge transfer in some way. Again this was not successful; it seems that the serial clocks can not be reduced beyond a certain threshold voltage without affecting CTE.

Having done this optimisation work on the serial register clock voltages, an unfortunate discovery was made. It was noticed that when experimenting with highly-reduced serial clock voltages the CTE degradation seemed to preferentially affect the image columns closest to the readout amplifier, i.e. those columns corresponding to pixels that started inside the EM register (recalling that the entire pipeline was read out in each row of the image). CIC events in columns corresponding to pixels in the conventional part of the serial register, in contrast, appeared quite sharp. This is quite hard to explain. If there is a CTE problem in the EM register then it should affect all pixels equally since they must all pass through it. It should be noted that any CTE problems in the conventional part of the serial register are not directly visible at these low signal levels: a single electron of signal cannot be elongated (the electron being of course indivisible) but will simply be displaced upstream during

the readout and its profile will be unaffected.

The only explanation is that some single discrete event, within each line readout, is temporarily reducing the charge containment within the EM register and allowing CIC events (left behind in the EM register from the previous line readout) to spread to neighbouring elements. This event could only be the line transfer event moving charge from storage area to the serial register and this was confirmed using an oscilloscope that revealed a spurious transition of the ϕ H2 clock phase due to an error in the waveform-tables of the controller software. Once corrected it was then found that the serial CIC gradient dropped dramatically even when using the highest serial clock voltages! The total CIC present in the images also dropped by approximately 50% to $0.017e^-$. It seemed that the spurious clock transition was creating a large excess of CIC. It should be noted that all the astronomical observations included in this thesis were performed before this bug was located.

More care was then taken with checking the CCD waveforms using an oscilloscope, and other short-comings became apparent. It was noted that the serial waveforms had a lot of unnecessary space between clock transitions. The device data sheet indicated that the CCD could be clocked at much higher speeds, with smaller gaps between clock transitions (in fact much smaller than the controller is capable of providing). The waveforms were subsequently modified to give an almost doubling in readout speed. This had to be done incrementally, using the autocorrelation technique to ensure that the CTE was not being degraded. It was also decided to raise the EM avalanche multiplication gain to 1840. This was needed to overcome the loss of system gain that came from speeding up the controller.

These changes further reduced the CIC signal in the bias frames (very slightly) from $0.017e^-$ to $0.015e^-$. Of this, $0.0007e^-$ was due to image area dark current. Disentangling dark current from CIC was done by taking a series of short dark frames with exposure times varying from 0 to 30s. At each exposure time the images were actually taken in blocks of 10 so as to improve the accuracy. A graph was then plotted to show dark signal versus exposure time. The gradient of the least square fit through this data was then equal to the true dark current and the y -axis intercept corresponding to a zero exposure time was equal to the CIC. The dark current was measured at $1.5e^- \text{ hour}^{-1}$, somewhat higher than previously measured. This rise in dark current could not be explained.

Figure 4.5 shows the shape of the serial clocks in the fastest configuration that could be achieved with the SDSU controller and high-voltage clock card. Any further reduction in clock overlaps gave unacceptably low CTE.

The same waveform is shown in Figure 4.6 with an extended time axis. The overall pixel time was $1.3\mu\text{s}$ of which $0.48\mu\text{s}$ was used by the CDS in the video processor and

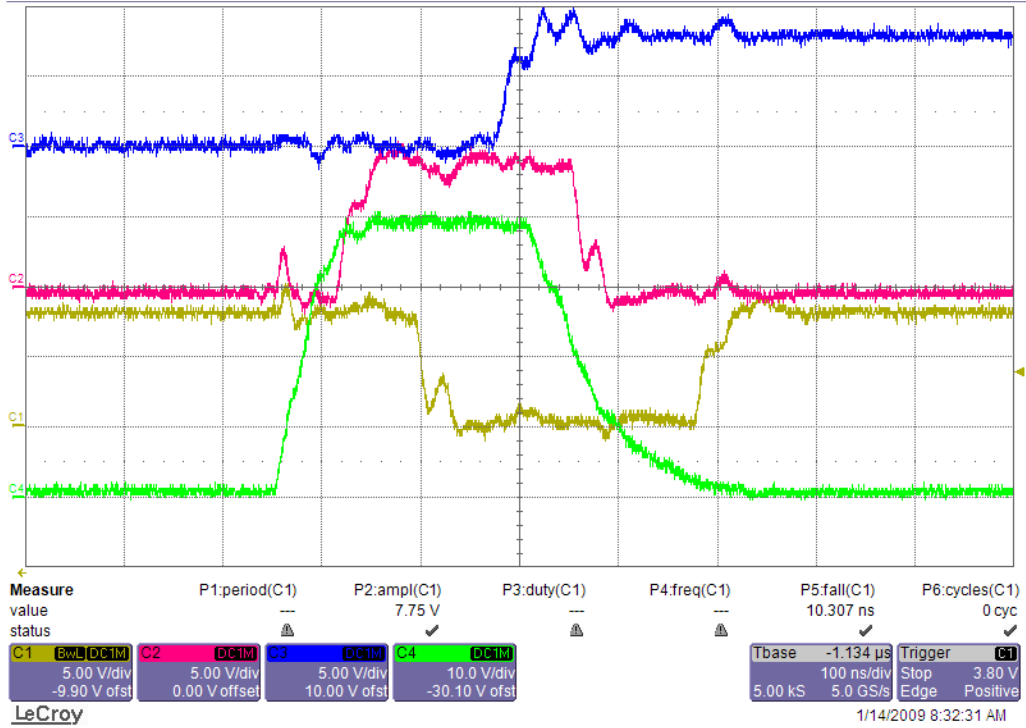


Figure 4.5: Optimised serial-clock waveforms. Zoomed in view of the critical charge transfer sequence. Note that the green HV clock has stabilised before $\phi H1$ (shown in yellow) goes low and causes the multiplication. At the instant that $\phi H1$ goes low the charge packets are attracted into the potential wells under the HV clock. The other two serial clock phases are shown in magenta ($\phi H2$) and blue ($\phi H3$). The waveforms appear quite noisy due to the 500MHz bandwidth of the oscilloscope and the capacitive coupling between the phases.

0.82μs was required to perform the clocking operations. Further reduction in pixel time would have been possible by reducing the sample times of the video processor at the expense of the read-noise. Since this would also increase the risk of pattern noise appearing once the camera was mounted on the telescope this was not done.

The dump gate technique was then revisited with more care to get an idea of just how much CIC was originating in the serial register after the optimisation of the serial clock voltages. The bias gradients induced by the DG activation were now so low that they could be seriously affected by any intrinsic bias gradients (even at the sub-ADU level) that may exist in the image due to limitations of the controller. This was overcome by fitting two lines through the data on either side of the step visible in the CIC at the start of the DG section (see Figure 4.4). The measured height of the step could then be used to calculate the true CIC gradient. Figure 4.7, obtained using the DG technique, with the slightly lower clock-low voltages required for good CTE, shows a gradient $p_{CS} = 3.3 \times 10^{-6}$ e⁻ per transfer when the clock-high voltage was equal to 8.5V. Since the serial register contains a total of 1540 stages this suggests a total serial CIC contribution ν_{CS} of 0.0051e⁻ (it was 0.0085e⁻ prior

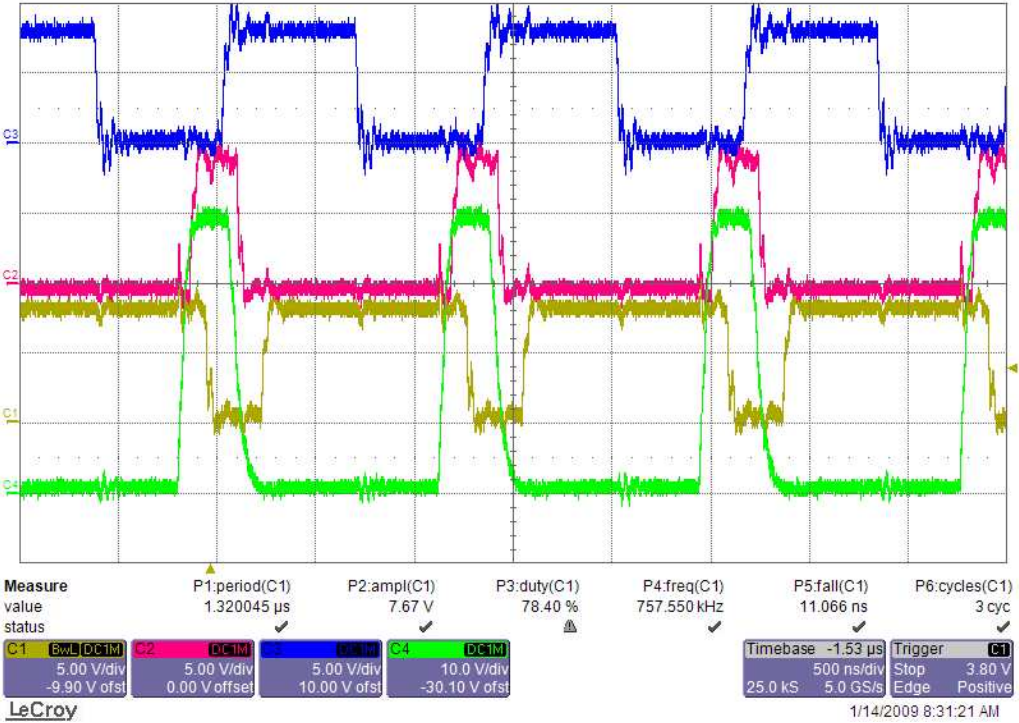


Figure 4.6: The optimised serial-clock waveforms presented in Figure 4.5 shown at lower time resolution over 3 complete pixel cycles.

to serial clock optimisation). Note the pipeline corruption visible in the black curve in this figure. The corrupted part, visible as a signal exponentially rising to the left, corresponds to the pixels in the connecting section between image and EM register. Since there is no applied potential to these register elements for several μs during DG activation this is not surprising. What is not explained is why the pipeline is *not* corrupted when the clock-high voltage is lowered from 8.5 to 8V (blue curve in Figure 4.7).

Regular measurement of the CTE went hand-in-hand with the serial clock optimisation process. Figure 4.8 shows the autocorrelation of the bias frames for various serial-clock voltages and confirms that the final CTE with reduced serial clocks was no worse than at the start of optimisation, at least at the single photoelectron level. The reduction in serial CIC was rather small (reduced by 40%) but nonetheless useful and the DG technique was found to be a valuable debugging aid.

4.1.3 Measurement of parallel CIC

As mentioned before in Section 3.8.2, the use of non-inverted mode effectively removed the parallel CIC contribution. With the camera noise now at a lower level following fine-tuning it was decided to try and remeasure the parallel CIC. It would have been nice to operate the CCD in such a way as to induce a bias gradient, as was

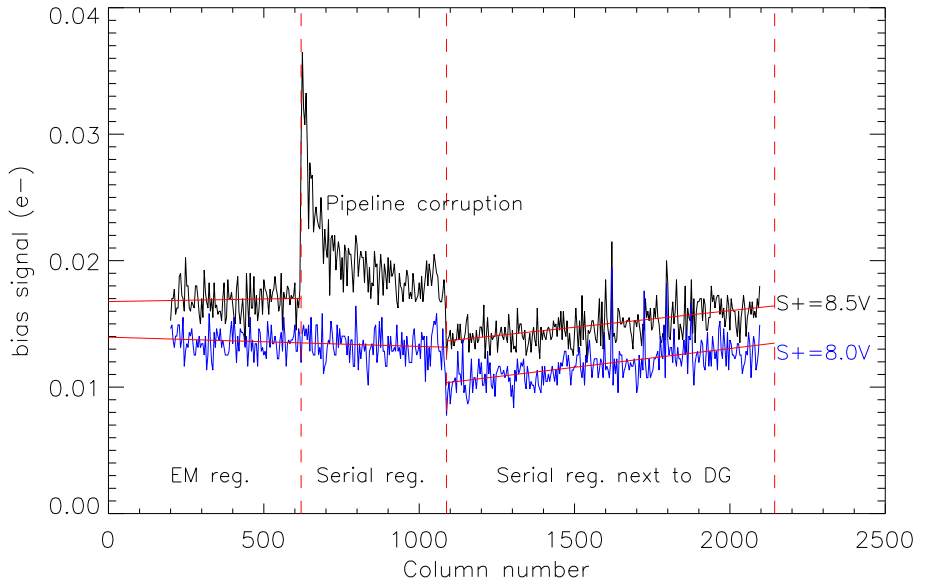


Figure 4.7: Use of the dump gate to measure serial-generated CIC. Here the lower serial clock level was -0.5V. The graph shows the CIC profiles for two different upper clock level values. The black curve shows the effects of pipeline corruption by the DG activation, between columns ~ 620 and ~ 1090 .

done when measuring the serial CIC. However, no such means could be found. With a more conventional three phase CCD this could have been done by reverse clearing the image and store areas prior to readout. The CCD201, being a virtual phase device, does not permit reverse clocking. Another method was therefore used. As explained in Section 4.1.2, the CIC distribution is normally flat due to the fact that the historical events left behind after a clear combine with those events generated during readout to yield a constant value independent of pixel position. This is not entirely true in the case of a frame transfer CCD if the store area is ‘overscanned’, i.e. more rows are read from it than are physically present within it. Prior to readout the entire CCD (store and image areas together) are vertically clocked so as to effect the image transfer, generating a smooth gradient of CIC events along the full height of the CCD. The key point is that when the store area is subsequently read out, the CIC present in those rows within the vertical overscan region will not contain *any* historical CIC since they do not correspond to physical pixels. They will, however, receive a full quantity of CIC from the storage area during readout. There will thus be a step in the CIC value above the final physical row of the storage area. If the CIC generated in the image and store areas are equal then the step should have a height of approximately 50% (the reason that it will not be exactly 50% is due to the image and store areas having a slightly different number of rows), although this could be distorted by the contribution of dark current. Taking two rows, the last physical row and the first overscan row, it should be now apparent that the latter has experienced exactly half as many parallel transfers as the former and should

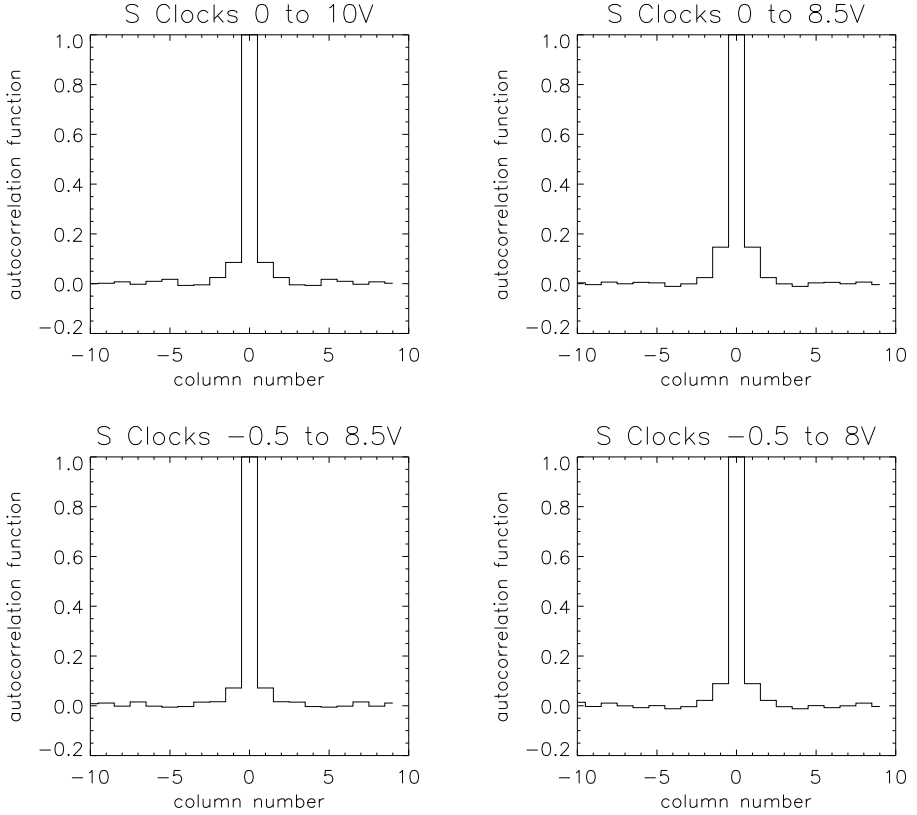


Figure 4.8: Monitoring of CTE using the autocorrelation technique during serial-clock optimisation. The substrate was at 4.5V. The serial clock voltages used are indicated at the top of each plot. Poor CTE manifests itself in these plots as an increase in the values lying immediately adjacent to the main peak. The horizontal axes are plotted in units of pixels. The vertical axes are plotted in units of the normalised autocorrelation function.

therefore see half as much CIC.

This method of analysis was first checked by looking at bias frames taken in inverted mode that were known to contain large amounts of parallel CIC due to the visibility of their serial underscans in bias frames. Indeed it was the case that the step could be seen in the vertical overscan region and this is shown in Figure 4.9. Interestingly, the step height is not 50%. This could have been explained by dark current, but this was ruled out after it was measured at only $0.0008e^-$ within the 1.6s frame time. It should be noted that these biases were not true biases because they were taken in long sequences (to improve the measurement accuracy up to 300 frames were taken) and in frame transfer mode (i.e. each frame was *not* preceded by a clear). In this case the exposure time is not zero, as it would be in a true bias from a slow-scan CCD with mechanical shutter. Instead, in a frame transfer CCD the bias frame effectively has a non-zero exposure time equal to the frame read time (see Section 1.2.6). Given the extremely low dark current of $1.5e^- \text{ hour}^{-1}$, however, the difference is small. The only remaining explanation is that the CIC generated in the image area is much higher than that generated in the store. It could be that the

aluminium overcoat on the store has some beneficial effect on the CIC. The total parallel CIC measured from Figure 4.9 is $0.11\text{e}^-/\text{pixel}$ in inverted mode.

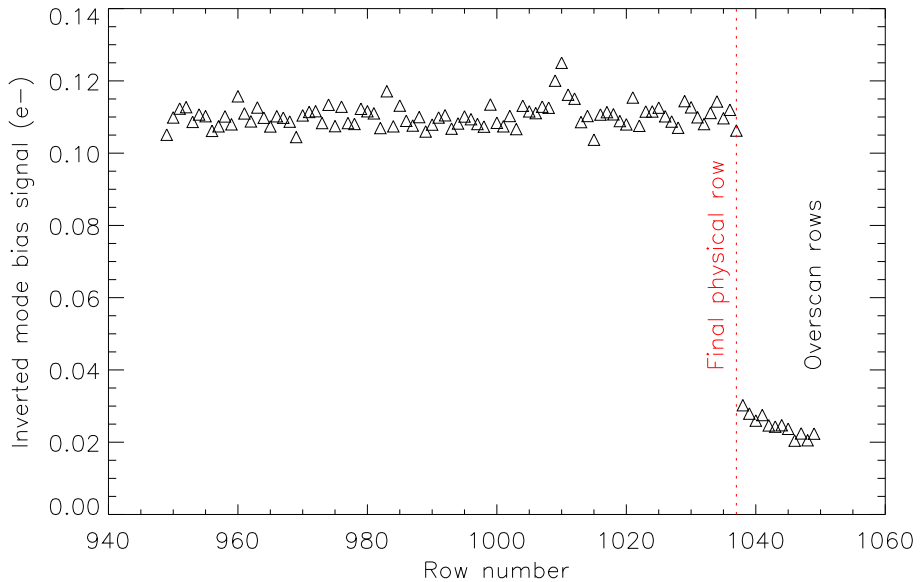


Figure 4.9: Parallel CIC made visible at the border of the vertical overscan region in inverted mode. The fact that the step is not 50% suggests that the image and store areas generate differing amounts of CIC.

The non-inverted bias frames were then investigated in the same manner. Data from 35000 image columns (combined from 50 separate frames) were averaged to give the plot shown in Figure 4.10. As can be seen, there is no step visible within the measurement noise of approximately 10^{-3}e^- . This is then slightly difficult to interpret without making the assumption that the CIC (which, if present, is below the accuracy of this measurement) is generated equally in image and storage areas. With this assumption we can then say that the total parallel CIC is $< 2 \times 10^{-3}\text{e}^-$ per-pixel. Figure 4.9 shows that this assumption is probably not true, however, and that the image area generates more CIC than the store. It was therefore difficult to draw any firm conclusion. Note that the total CIC, which is shown by the data points corresponding to the physical (i.e. light sensitive) rows is at a level of between 0.01 and 0.015 e^- . Since this is approximately the amount that was measured in the serial overscan regions we can at least say that the use of non-inverted mode had reduced the parallel CIC to a negligible level.

The plot in Figure 4.10. shows the presence of a very low-level bias gradient and is a reminder of how important this can be when measuring such tiny signals. The gradient amounted to a fraction of an ADU in the raw frames. Its effect was minimised by making CIC measurements only within small regions of the image over which the bias gradient was negligible.

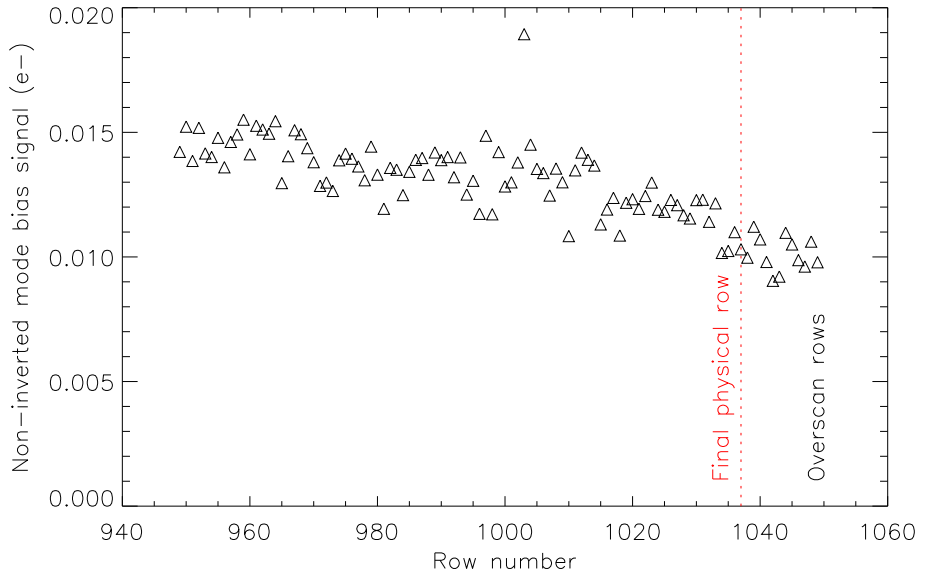


Figure 4.10: A vertical cut through many averaged bias columns. The top section of the images had a strip of parallel overscan. A step in the parallel CIC is not visible at the border of the vertical overscan region in non-inverted mode.

4.1.4 Tuning of EM register clock waveforms

Attention was now turned to the EM register. Unfortunately the amplitude of the EM HV clock phase could not be varied as freely as the serial clocks since it directly affects the EM gain. Instead, several alternatives were tried. Firstly, the E2V data sheet states that it is the voltage difference between the HV clock and an adjacent bias gate, designated $R\phi DC$ that determines the amplification factor. It was reasoned that, by dropping the HV clock amplitude whilst at the same time dropping the bias voltage (a DC level) on $R\phi DC$ (see Figure 1.9), some reduction in CIC could be achieved. No improvement could be seen. The second modification that was tried was to add load capacitors to the HV clock driver so as to slow down its edge transitions. This seems reasonable since clock slew rate is described by Janesick (2001) as a key factor in generation of CIC in inverted mode devices. This change had no effect and the bias image per-pixel charge (almost entirely CIC) remained stubbornly at around $0.013e^-$.

4.1.5 Reduction of EM-register CIC using high gain

In this section the effective charge of an electron generated at a random position within the EM register is calculated. Such electrons constitute CIC and because they do not experience full amplification they effectively have a fractional charge \bar{q}_I . The relation between \bar{q}_I and avalanche multiplication gain g_A is derived later in this section.

If the EMCCD is operated in linear mode then a high multiplication gain can reduce the significance of in-EM register CIC. This is because a high gain will increase the mean value of a photoelectron by a greater factor than it will increase the mean value of an in-EM register CIC electron.

This can be shown mathematically as follows. The mean value, q_O , of a pixel with one photoelectron of signal as it transits the EM register is given by

$$q_O = (1 + p)^x, \quad (4.1)$$

where x is the position within EM register and p the per-transfer multiplication probability. The mean value, \bar{q}_O , of this pixel during its EM register transit can then be obtained by integrating this function over the length of the register and then dividing by the number of stages N . If we reference this charge to an equivalent signal at the input to the register, such that $q_I = q_O/g_A$, we get:

$$\bar{q}_I = \frac{1}{Ng_A} \int_{x=1}^N (1 + p)^x dx, \quad (4.2)$$

where N is the total number of stages within the EM register. This is given by the standard solution

$$\bar{q}_I = \frac{1}{Ng_A \ln(1 + p)} [(1 + p)^x]_{x=1}^N, \quad (4.3)$$

which gives the result

$$\bar{q}_I = \frac{1}{Ng_A \ln(1 + p)} [(1 + p)^N - (1 + p)^1], \quad (4.4)$$

since we have already defined $g_A = (1 + p)^N$ and therefore that $N \ln(1 + p) = \ln g_A$, this then reduces to:

$$\bar{q}_I = \frac{g_A - (1 + p)}{g_A \ln g_A} \approx \frac{1}{\ln g_A}. \quad (4.5)$$

Equation 4.4 then shows the average size of an electron within the EM register. This will then also be the average size of a CIC event originating within the register, when referenced to the register's input.

Now it is interesting to examine how ν_{CEM} , the in-EM register generated per-pixel CIC charge for our particular camera measured in photoelectron equivalent electrons, varies with g_A for a given probability of CIC generation per stage within the EM register, p_{CEM} . The generation of CIC is described by binomial statistics, where the number of trials is equal to the number of stages in the EM register and the probability of 'success' is equal to p_{CEM} . Binomial theory shows that the mean number of successes (i.e. the mean number of CIC events per pixel) is simply

$= p_{CEM}N$. Referring back to Equation 4.4,

$$\nu_{CEM} = \bar{q}_I p_{CEM} N. \quad (4.6)$$

Expanding we get

$$\nu_{CEM} = \frac{p_{CEM}N[g_A - (1 + p)]}{g_A \ln g_A}. \quad (4.7)$$

We can now insert some actual experimental data into Equation 4.7. The per-pixel CIC charge ν_C , from all sources was measured in Section 4.1.4 to be $0.013e^-$. In Section 4.1.2 the contribution from the serial clocks ν_{CS} was measured to be $0.005e^-$. This would imply that ν_{CEM} was equal to $0.007e^-$ (given that $\nu_C = \nu_{CS} + \nu_{CEM}$). This therefore implies that $p_{CEM} = 8.8 \times 10^{-5}$, more than an order of magnitude higher than the probability of CIC generation per-stage within the serial register, p_{CS} . This is to be expected, given the higher voltages present.

If we were to then increase the EM gain what would be the effect on ν_{CEM} ? Figure 4.11 shows what could be expected. Since higher multiplication clock voltages

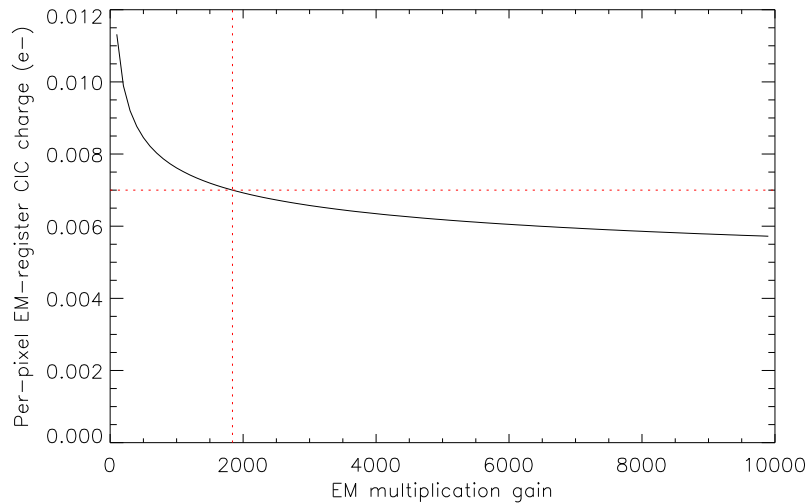


Figure 4.11: Use of high EM-gain to reduce the significance of in-EM register generated CIC when operating in linear mode. The dashed red cross shows the actual gain and CIC levels of the camera. The graph shows how the measured per-pixel CIC charge would drop if even higher gains had been employed.

are required there is also the possibility of this producing a higher per-transfer probability of CIC being generated. Note that if the camera is used in photon-counting mode the use of higher multiplication gains will not give a SNR advantage. The number of CIC events, that will be counted as photons, produced in the EM register is $p_{CEM}N$. The multiplication gain does not enter into the equation. In fact, higher multiplication gains may reduce photon counting performance since the higher clock voltages required could actually increase p_{CEM} and therefore the amount of CIC

generated within the EM register.

Since the CCD was already being operated at a fairly high gain it was thought best not to experiment with even higher multiplication voltages. This was an operational camera and it was impossible to rule out accidental over-exposure. According to the manufacturers, sustained illumination at high signal levels (i.e. close to the charge capacity of the image area pixels) and high gains can cause ageing and even failure of the device³. Even moderate exposures that result in near-saturation of the EM register for sustained periods can cause a reduction in gain. It was therefore decided to accept the CIC figure of $0.013\text{e}^{-}\text{ pixel}^{-1}$ and to devote further effort to other aspects of the camera's performance. Nevertheless the result shown in Figure 4.11 does hint at the possibility of reducing in-register CIC by a further 20% if it could be guaranteed that the camera will not be damaged through over-exposure. Note that on this graph an EM multiplication gain of 10,000 would reduce the in-EM register CIC from 0.007 to 0.0056e^{-} .

4.2 Confirmation of EM-register charge capacity

During optimisation the whole serial clocking process had been radically altered. It thus seemed sensible to re-measure the capacity of the EM register to check that no degradation had occurred due to the reduced clocks and faster readout. Reduced register capacity directly affects the dynamic range of the system and so is an important parameter.

A de-focused spot image of varying brightness was read out through the EM output. It was necessary to first reduce the electronic gain of the video amplifier within the controller to increase its dynamic range. This new gain then had to be measured using faint flat fields and the histogram gain technique (see Section 3.2). Figure 4.12 shows cuts through the spot image as its brightness was increased. The spot image was examined for horizontal blooming, apparent both as an elongation of the image and also as a smoothing of its internal structure, which was found to begin at a signal level of 400ke^{-} . This was actually better than before (see Figure 3.20) and closer to the data sheet value of 750ke^{-} , probably due to the more carefully phased serial clocks and perhaps also to the slightly higher HV clock amplitude. The EM multiplication gain was 1840 so this blooming limit corresponds to an input signal of more than 200e^{-} , i.e. more than sufficient to cover the read-noise dominated regime of a conventional CCD. Note that blooming actually occurs just after the CCD response becomes non-linear so here we are not, strictly speaking,

³E2V L3 sensor ageing technical note 5: http://www.e2v.com/assets/media/files/documents/imaging-space-and-scientific-sensors/Papers/low-light_TN5.pdf

measuring the upper limit of the EM-register linearity. Nevertheless it was still a useful measurement since it showed that the register capacity had not suffered during the optimisation process.

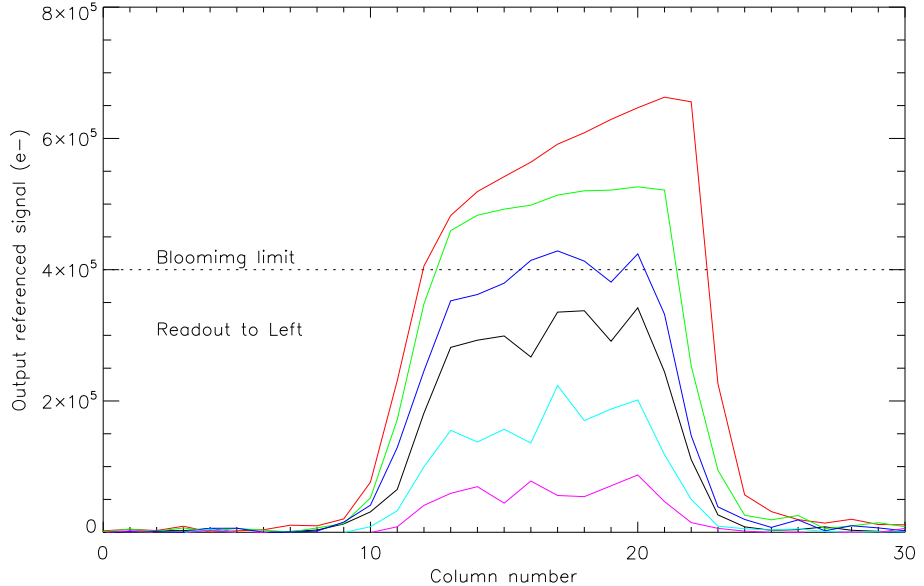


Figure 4.12: Repeat measurement of the EM-register charge capacity after optimisation. Blooming occurred at around 400ke^- where the spot profile begins to elongate. This was approximately twice the pre-optimisation value (see Figure 3.20).

4.3 Confirmation of system linearity

After so much adjustment of the serial-readout waveforms and voltages it was thought prudent to re-measure the system linearity. This was done on the ISIS spectrograph using a tungsten calibration lamp to project a flat field onto the camera. The exposure time was incremented and the peak signal in the image measured. The plots in Figures 4.13 and 4.14 show how the response of the camera varied as a function of the exposure time. This result should be compared with the initial results for the linearity shown in Section 3.7. The conventional amplifier is actually better than before ($+0.2/-0.4\%$ error rather than $+1/-4\%$) although this could be explained by an improved measurement technique since the first result was rather noisy. The EM output has acceptable linearity only up to 12kADU. This is somewhat lower than many observers would expect. Quoting this value in ADU rather than electrons is more useful since an observer can tell directly from their images if they are in the non-linear region or not without having to convert the units themselves.

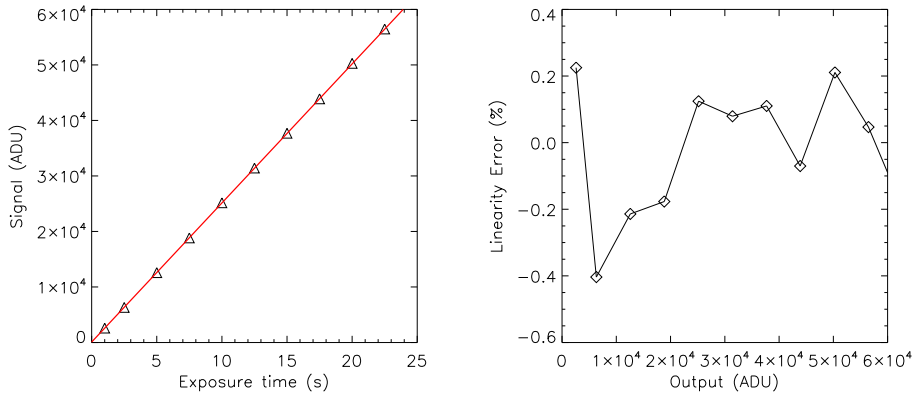


Figure 4.13: Final linearity of the normal output. The panel on the left shows a least-squares linear fit through the data points. The panel on the right shows the residuals of this fit.

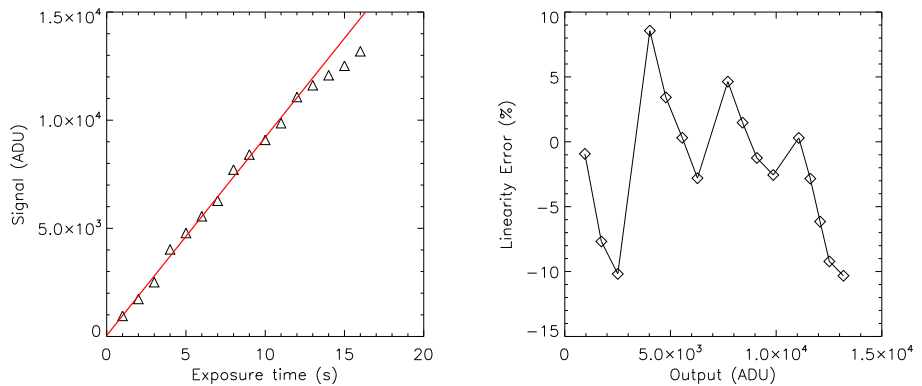


Figure 4.14: Final linearity of the EM output. The panel on the left shows a least-squares linear fit through the data points. The panel on the right shows the residuals of this fit.

4.4 Photon counting with EMCCDs

Photon counting (PC) with an EM camera requires careful optimisation of the threshold level, above which a pixel is interpreted as containing a single photon. Providing that the signal levels are not too high (i.e. low enough to ensure negligible coincidence losses) then the observer has the choice, once the observations are complete, to interpret the images linearly or using photon counting. The former method is the traditional interpretation of pixel value being linearly proportional to the number of incident photons. This will necessarily include the effects of multiplication noise as explained in Section 1.3.5. If instead we choose to photon count by applying a threshold and interpreting those pixels above this value as containing a single photoelectron we can avoid the effects of multiplication noise and approach very closely to the performance of an ideal detector. One can even imagine different parts of the same image being subject to these two contrasting methods of interpretation. A bright spectral line containing several electrons per pixel would

be interpreted linearly since coincidence losses would preclude the use of photon counting whereas a nearby faint spectral line containing, for example, $0.1\text{e}^- \text{ pixel}^{-1}$ could be photon counted.

4.4.1 Optimisation of the PC threshold

The choice of threshold is quite complex (Basden et al. 2003). It depends very much on the characteristics of the camera in question and in particular on the distribution function of the CIC. It also depends on the mean signal level of the object under observation. Luckily there is no need to decide on a threshold prior to the observation and it can be optimised fully during the reduction. With a camera whose noise performance is dominated by CIC originating prior to the EM register there is little flexibility for reducing the noise by judicious placement of the threshold. The distribution of CIC events will closely match that of the genuine photoelectrons and any reduction in the threshold, so as to allow through more photoelectrons, will also detect a proportionate increase in CIC events. If, however, the CIC is very low and the object reasonably bright then there will be a benefit from pushing the threshold lower; the exact value needs to be tuned to the object's brightness. For CIC originating within the EM register the distribution of events is heavily skewed to lower values, which causes a sharp increase in detected CIC as the threshold is lowered. This will be accompanied by only a gradual increase in detected photoelectrons. Once again the exact placement of the threshold depends on the object brightness and the CIC level. The ultimate lower limit on the threshold placement is dictated by the read-noise of the camera. If the threshold approaches too closely to the bias level then pixels containing just read-noise (and no real signal) will be interpreted as containing photoelectrons and the SNR will plummet.

Figure 4.16 shows the cumulative distribution function (CDF) of pixel values for a stack of genuine bias frames containing a mean per-pixel charge of 0.013e^- due to CIC and dark current. Figure 4.15 shows the same analysis but this time for a stack of synthetic flat-field frames containing only photoelectrons (i.e. no CIC or read-noise) with a mean illumination low enough to avoid significant coincidence losses. Section 5.0.1 explains in more detail how these synthetic frames were generated. These two figures in effect show how the photon counting efficiency and the susceptibility to noise are affected as the threshold is gradually reduced where the threshold is expressed in units of input referenced photoelectrons. Note that at lower threshold values the detected fraction of photons approaches one whereas the mean counts per pixel resulting from CIC and read-noise approaches 0.5. As far as the photons are concerned, the lower the threshold the better. In the case of the noise sources in the bias frame, setting the threshold too low is disastrous and

can effectively multiply the CIC that we measure by a large factor. The source bias frames used to produce Figure 4.16 contained a mean charge of $0.013\text{e}^- \text{ pixel}^{-1}$ but if we use photon counting with, for example, a threshold of 0.07e^- then the mean count rate will be $0.04 \text{ counts pixel}^{-1}$. The CIC has effectively been multiplied by a factor of 3 in this case. If we consider a CIC event that has been generated half way along the EM register then it will appear as a discrete event in the output image and therefore may be counted as a photoelectron. It will, however, on average only contribute a fraction of the charge produced by a genuine photoelectron to the bias frame if that frame is interpreted in the proportional manner since it will not experience the full multiplication factor of a photoelectron traversing the full length of the EM register. This means that a bias frame containing, for example, a mean charge of $0.01 \text{ e}^- \text{ pixel}^{-1}$ of CIC (measured proportionally) will contain considerably more than 1 event per 100 pixels if that frame is then analysed using photon counting. The second reason for the multiplication of the noise sources (CIC and read-noise) at low photon-counting thresholds is the effect of false triggers due to read-noise with a Gaussian distribution. If the threshold lies within the underlying read-noise and approaches the bias level, then up to half of the pixels will be interpreted as containing a photoelectron. This tends to push the optimum threshold to higher values. Equation 4.8 shows the SNR obtained using a photon counting analysis.

$$\text{SNR}_{PC}(t) = \frac{\text{Signal}.F_P(t)}{\sqrt{\text{Signal}.F_P(t) + \text{CIC}(t)}}, \quad (4.8)$$

where $F_P(t)$ is the detected fraction of signal and $\text{CIC}(t)$ is the CIC count rate for the given threshold t .

The pixel value distributions shown in Figures 4.15 and 4.16 were then used to model the performance of QUCAM2 in photon-counting mode. In this model the object signal was set at 0.01e^- , 0.05e^- and 0.1e^- and the SNR calculated as a function of the photon counting threshold using Equation 4.8. It was thought to be more instructive to express the resultant SNRs as a fraction of the SNR that could be obtained under the same conditions using the CCD in proportional mode. Higher intensities were not considered since coincidence losses would become significant. The result is shown in Figure 4.17. The graph indicates that the CIC of this camera was slightly high for efficient photon counting, offering a 20% gain if the threshold is carefully chosen (under ideal conditions photon counting can improve the SNR by up to 40%). It would seem that a reduction in CIC would offer further benefits and this is the subject of more detailed modeling in Section 5.2. Note that at lower threshold values the photon counting SNR falls steeply due to the effects of false triggers from the read-noise. At higher threshold values there is a loss of SNR due to most photoelectron events falling under the threshold and being lost. The graph

also indicates that the threshold should be set between 0.1 and 0.4e⁻ depending on the signal level.

4.4.2 Summary of the camera noise sources

The final signal level in the bias frames was 0.013e⁻ pix⁻¹ of which 0.005e⁻ is believed to be due to serial CIC and 0.0007e⁻ due to image-area dark current. The parallel CIC could not be detected in non-inverted mode operation. This leaves 0.007e⁻, which is assumed to originate in the EM register. Since charge originating within the EM register has a different distribution to that originating before the EM register, the exact origin of the CIC can be resolved by examination of the bias histograms. This is modeled in some depth in Section 5.1. To put the significance of CIC into perspective, it is useful to compare it with the typical dark-sky background signal of the William Herschel Telescope. When used with a medium resolution (0.43Å per pixel) grating on a moonless night, the ISIS spectrograph sees 0.003e⁻ pix⁻¹ s⁻¹ through its red arm. In this configuration the CIC is thus the limiting noise source of the camera, at least for exposures of up to 5s duration.

4.5 Final performance of camera

Once the fine tuning phase was complete the camera performance was as shown in Table 4.1. The CTE has been quantified exactly by comparing various models with actual images and is described in detail in Section 5.1.1. These final performance parameters are quite acceptable in all respects except for the rather high CIC. This remains the limiting noise source in the camera. The two outputs of the camera are quite complementary. The normal output gives a performance at least as good (and actually slightly better in terms of read-noise) as the other science cameras in use at the ING. For fainter objects, the EM output also performs well: it has exceptionally low noise and a dynamic range high enough to give a good overlap with the range of operation of the normal output. For example the EM output is linear up to approximately 80 photoelectrons of signal per pixel. The photon noise at this level is about 9 photoelectrons. If we then switched to the conventional amplifier which has about 3e⁻ of read-noise we would still be photon-noise dominated.

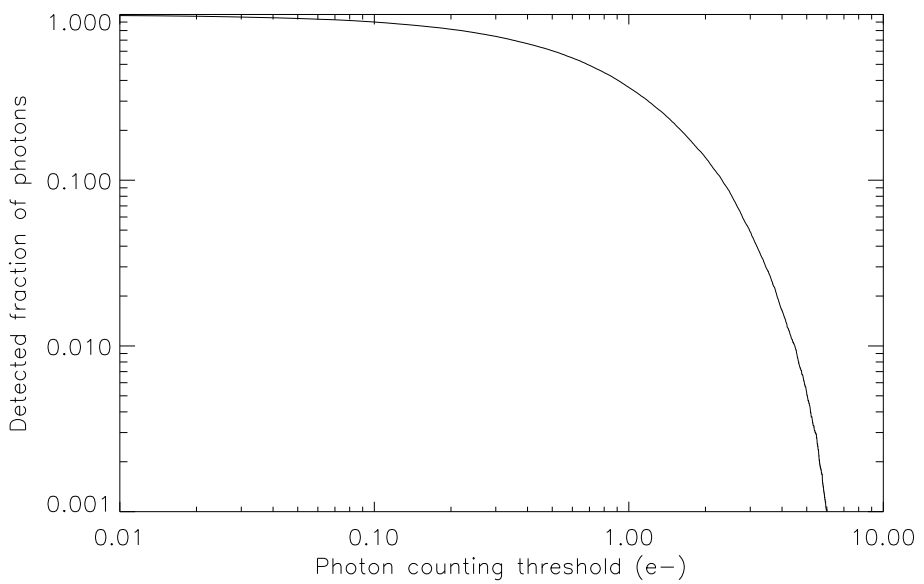


Figure 4.15: Effect of varying photon counting threshold on the detected fraction of photoelectrons. Based on model images.

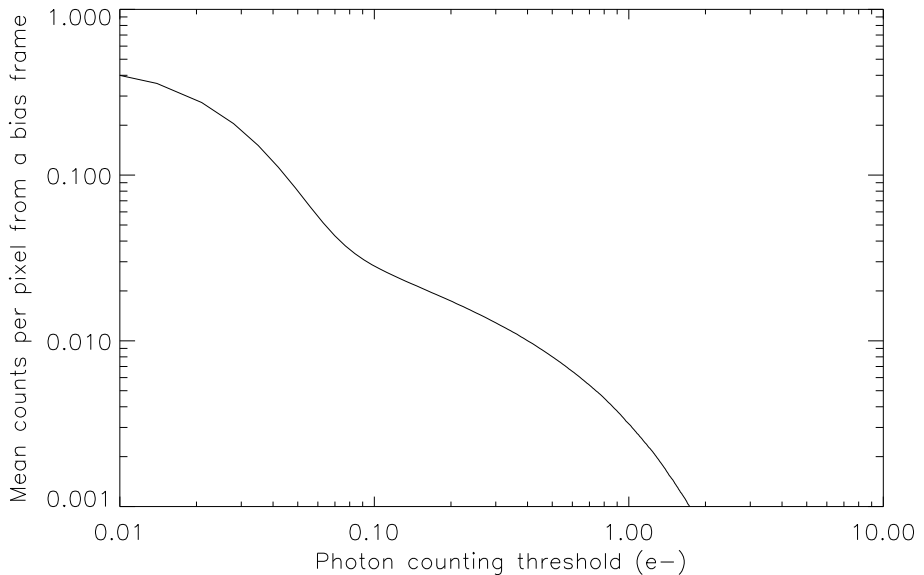


Figure 4.16: Effect of varying photon counting threshold on the noise contribution from CIC and read-noise. The images are actual QUCAM2 bias images in which the mean CIC charge was $0.013\text{e}^{-}\text{pixel}^{-1}$.

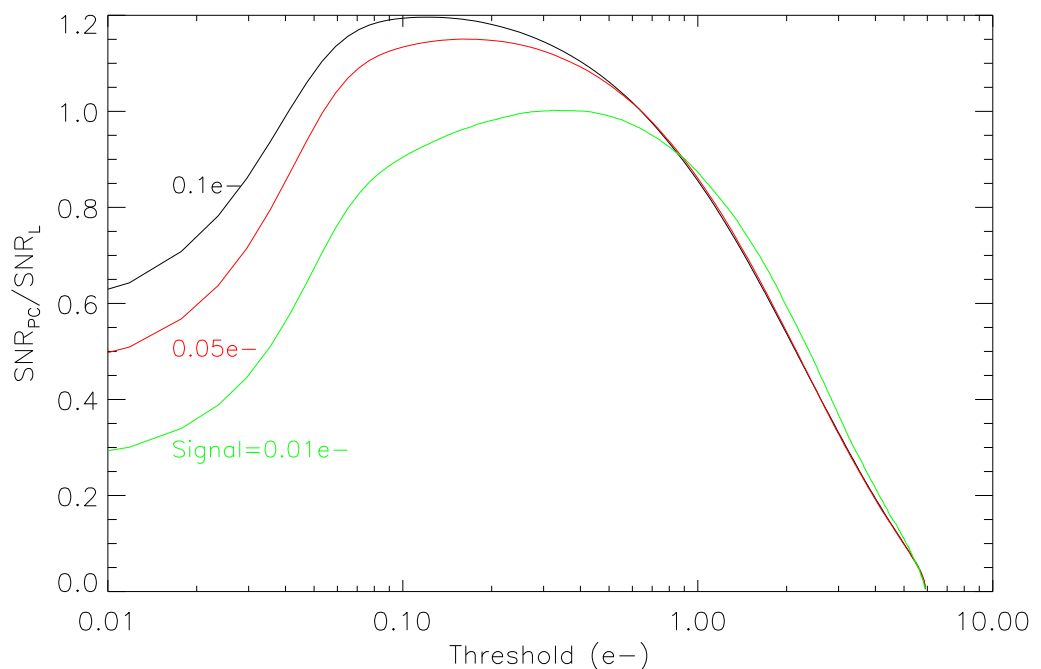


Figure 4.17: SNR gains from using photon counting at three discrete signal levels. The photon counting SNR (SNR_{PC}) is compared with that achievable if the CCD is operated in linear mode (SNR_{L}). The threshold is expressed in units of input-referenced photoelectrons.

Table 4.1: Final performance of camera

Pixel time total (EM amplifier)	$1.3\mu\text{s}$
Pixel time CDS (EM amplifier)	$0.24+0.24\mu\text{s}$
Pixel time (normal amplifier)	$5.1\mu\text{s}$
Pixel time CDS (normal amplifier)	$2+2\mu\text{s}$
Frame transfer time	13ms
Row transfer time	$12\mu\text{s}$
Full frame read (EM amplifier)	1.6s
Full frame read (normal amplifier)	5.4s
System gain g_{S0}^* (EM amplifier)	$12.85\text{e}^-/\text{ADU}$
System gain g_S (normal amplifier)	$1.05\text{e}^-/\text{ADU}$
EM multiplication gain g_A	$\times 1840$
Read-noise (EM amplifier)	40e^-
Read-noise (normal amplifier)	3.1e^-
Mean charge in bias image	$0.013\text{e}^- \text{pixel}^{-1}$
Cosmic ray rate	$0.9\text{e}^- \text{pixel}^{-1}\text{hour}^{-1}$
Image area dark current	$1.5\text{e}^- \text{pixel}^{-1}\text{hour}^{-1}$
Parallel CIC per transfer	negligible
Serial CIC per transfer	$3.3 \times 10^{-6} \text{ e}^-$
Serial CIC total	0.005e^-
EM register CIC per transfer	$1.4 \times 10^{-4} \text{ e}^-$
EM register CIC total	0.007e^-
EM register (single electron level) CTE per transfer	0.99985
Parallel CTE (per transfer)	> 0.999999
Serial CTE (per transfer)	> 0.999999
Image area full well	140ke^-
EM register full well	400ke^-
Linearity (EM amplifier)	$\pm 5\% \text{ to } 12\text{kADU}/83\text{e}^-$
Linearity (normal amplifier)	$\pm 0.4\% \text{ to } 63\text{kADU}/66\text{ke}^-$
Operating temperature	178K
Optimum photon counting threshold	0.1 to 0.4e^-
Operating mode	Non-inverted

* see Section 1.3.2

4.6 Comparison with other cameras

Olivier Daigle from the Université de Montréal supplied bias frames from a CCD97 EMCCD that contained an average of only 0.0029e^- of charge per pixel. It was not possible to determine what fraction of this charge originated as CIC and what originated as dark current since only a series of bias frames was analysed. His camera uses the high speed ‘CCCP’ controller (Daigle et al., 2008) that operates at up to 30 frames per second using avalanche multiplication gains of up to 4000. Interestingly, he has chosen to use inverted-mode operation due to concerns over high dark current

in non-inverted mode. This is in total contrast to the results of this thesis where the parallel CIC in inverted mode was found to be unacceptably high. His system has been designed for photon-counting operation with the emphasis on high-speed readout in order to reduce coincidence losses when observing brighter sources.

He claims that the CIC level of the camera is as low as 0.001 photoelectrons per pixel per frame (i.e. 1 pixel in a thousand lies above the photon-counting threshold). However, expressing a camera's noise level in units of mean counts rather than mean charge per pixel can be very misleading since it is an incomplete description. One can reduce the mean photon counts per frame arbitrarily by simply raising the photon counting threshold. This of course also reduces the detected fraction of genuine photoelectrons. A histogram of the pixel values in his images is shown in

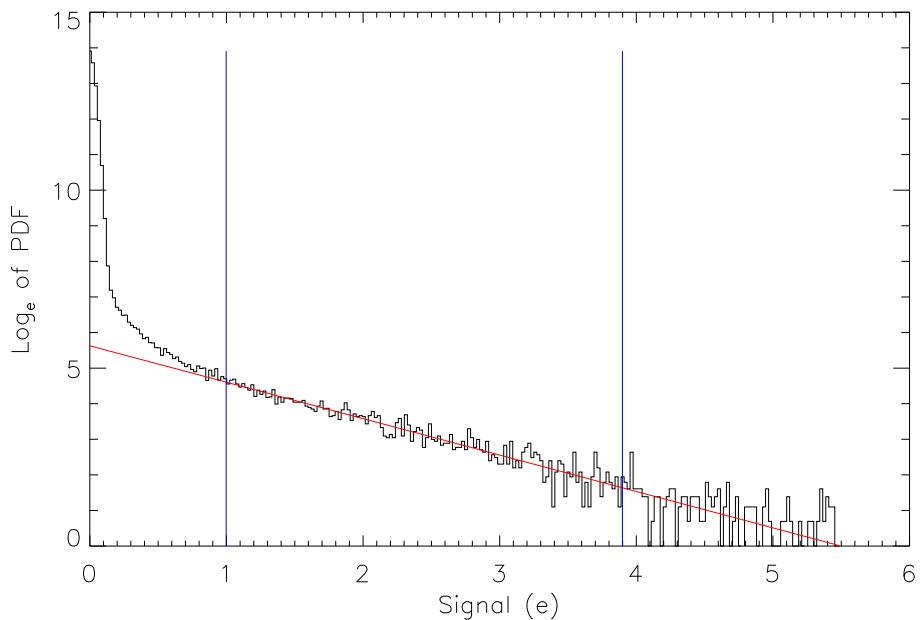


Figure 4.18: Histogram of noise events for an EMCCD camera built at the University of Montréal (Daigle et al., 2008). The plot shows a linear fit to the region lying between the two vertical blue lines. This fit was used to calculate the system gain and measure the level of noise (due to CIC and dark current) in the frames. This was found to be very low: 0.0029e^- .

Figure 4.18. This has been plotted with a horizontal axis labeled in units of input-referenced photoelectrons. Note the very high read-noise ($\sigma/g_A=0.04\text{e}^-$ RMS) in the bias, shown by a very broad peak around the origin. This level is rather high for efficient photon counting and compares with $\sigma/g_A=0.025\text{e}^-$ for QUCAM2. This is a consequence of the higher readout speeds used. If we set the photon counting threshold to $5\times$ the RMS read-noise (corresponding to an input referenced signal of 0.2e^-), so as to be well above the read-noise in the bias then, referring to Figure 4.15, only about 81% of the genuine photon events will be detected. At this threshold the count level in the biases due to CIC and dark current was 0.003 per pixel per

frame. This camera either needs a higher multiplication gain or a lower read-noise.

Daigle was not able to divulge the details of his serial clocking waveforms but it seems likely that he has found a way to reduce considerably the CIC events generated within the EM register. His use of extremely-high readout speeds (8Mpix s^{-1}) and high multiplication gains could be responsible for his success. Ives (2007) also believes that fast serial readout can help to suppress CIC. Fast readout (and the high frame rates that are implied) will certainly reduce the dark current component within each frame. It is very easy to mistake dark current for pre-EM register CIC which adds further difficulty in establishing the exact CIC level.

During the writing of this thesis a second camera, QUCAM3, was built. It was essentially a copy of QUCAM2; it also contains a CCD201 and is operated identically to it. Its performance is notably different, however. First, it had to be operated about 10 degrees colder in order to obtain the same dark current, although this could be explained by a poorer thermal contact between the CCD and the baseplate on which the temperature sensor is mounted. Second the CIC was measured to be 0.01e^- with virtually no optimisation. It will be interesting to see if there are any ageing effects that cause this value to rise with use.

Derek Ives at the UKATC kindly provided bias frames from his ULTRASPEC camera (Ives et al. 2008). This camera also uses a CCD201 device. These images were analysed for noise and were found to contain a mean charge of $0.01\text{ e}^- \text{ pixel}^{-1}$. Once again, it was not possible to decide what fraction of this is due to CIC and what fraction is due to dark current since only bias frames were analysed.

Chapter 5

Modeling of an EMCCD

The multiplication process of the camera was found to be amenable to Monte Carlo modeling. Initially this model (coded in IDL) was used to examine the distribution of pixel values for image-area generated photoelectrons to confirm the accuracy of the system-gain measurement program. The model was then extended to include the effects of CIC generated in various parts of the readout pipeline. In the photon counting regime the model also proved very useful since the CIC performance could be freely varied and its effect on the SNR examined. The model was also useful for exploring the performance of hypothetical future detectors. The models proved extremely useful in exploring the observational regimes where photon counting is to be preferred over linear mode operation.

5.0.1 Basic model of the multiplication process

The basic model consisted of an IDL function with two input parameters. The first was a 2D integer array of pixel values, the units being photoelectrons. The second parameter was the multiplication gain. The output was a 2D integer array, i.e. the output EMCCD image. The accuracy of the model was tested by first confirming that the mean output pixel value was indeed equal to the mean input value multiplied by the avalanche gain and secondly by checking that the form of the output pixel histogram matched that of an actual low-level flat field. The basic model is shown in Appendix A along with detailed comments that describe its operation.

5.0.2 Advanced model of the CCD201 EMCCD

The basic model was then extended to include more parameters, including imperfect CTE, CIC originating in the image, serial pipeline and EM register regions and

amplifier read-noise. The aim was to simulate, as closely as possible, real CCD201 images. This advanced model took a lot longer to run, as much as 2 hours for a single bias frame and even more for images containing significant illumination. Rewriting in a compiled language such as `gcc` would have given faster execution but it was felt that the convenience of using `IDL` more than offset the need to do overnight simulations. The advanced model code is shown in Appendix B along with detailed comments.

5.1 Engineering applications of the model

An engineering application is one that allows the internal workings of the CCD to be better understood. For example it can give valuable clues on the origin of various noise sources, in particular the origin of CIC.

5.1.1 Single-electron CTE

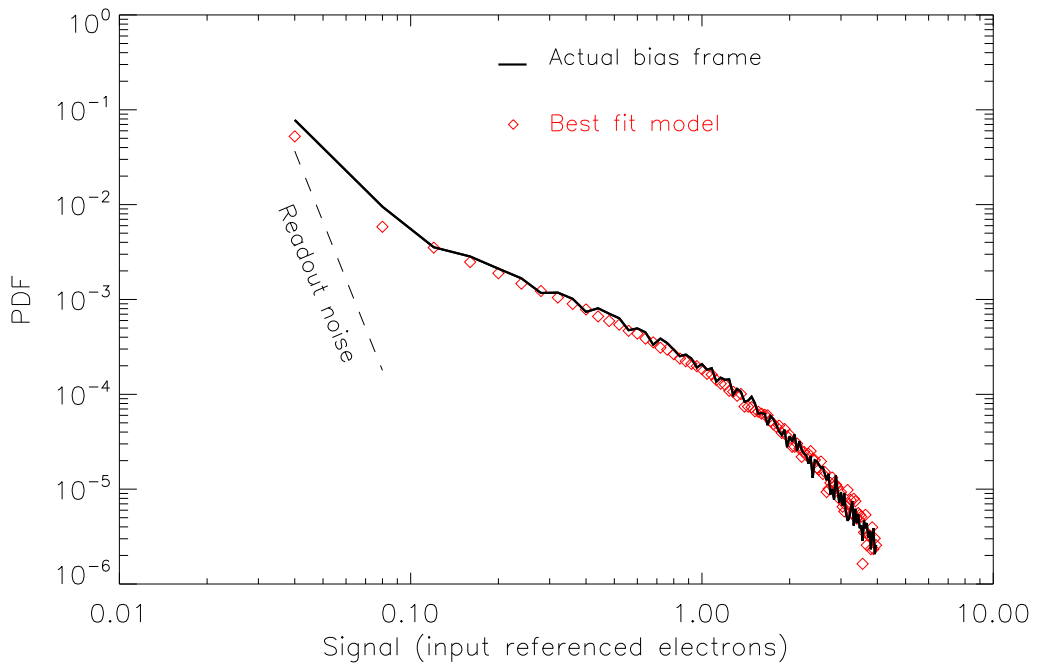
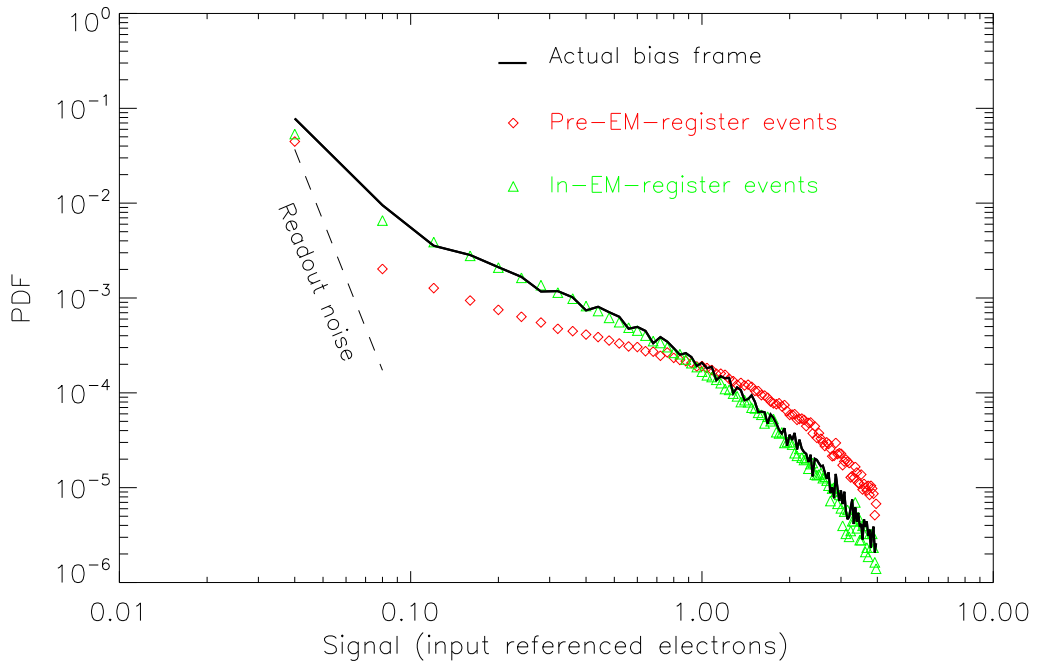
It was very important to quantify the CTE of the camera at an early stage since imperfect charge transfer had a large effect on the image histograms. At the single electron level, imperfect CTE will only be clearly visible in a single frame if it originates in the EM register. Bias frames clearly showed a slight elongation of some of the single electron events, indicating imperfect EM register CTE. Loss of CTE in the conventional part of the serial register would merely give a displacement rather than elongation of the event. Even at the low end of the acceptable range of CTE, the probability of a perfect transfer at the single electron level is still extremely high, with an electron experiencing on average less than one failed transfer during the entire readout process of up to 2069 vertical transfers and 2160 horizontal transfers. If this failed transfer occurs close to the start of the EM register, say after the input electron has experienced a single successful multiplication, then a large degree of elongation will result. If instead the failed transfer occurs close to the output end of the EM register then the proportionate elongation will be quite small. Examining any elongation in a single event and using it to infer the CTE will therefore give a large spread in values; a large collection must instead be studied. Since the Advanced Model included the effects of imperfect CTE, it was decided that the best way to quantify the CTE is an experimental approach that involved fine tuning the model parameters until a good fit between the autocorrelation function of the synthetic and real images could be found. It is important to use flat fields of low illumination rather than biases. Bias frames contain a large proportion of signal that originates within the EM register (the exact proportion still being somewhat uncertain). These

in-register events will on average experience fewer transfers and will thus indicate a higher CTE than for events originating pre-register. Using frames that contain an overwhelming proportion of pre-register events removes the uncertainty.

The fine-tuning process involved generating weak flat field images containing tens of mega-pixels, running these images though the EM register and then autocorrelating the resultant amplified image. The shape of the autocorrelation function was then compared with the autocorrelation of a genuine weakly illuminated flat field. After a few iterations a good fit to the data was found using a model with the CTE in the EM register of 0.99985 per transfer. Since the EM register contains 604 elements this meant that approximately 9% of the charge in a pixel is deferred to its upstream neighbour. This is somewhat higher than for a normal CCD where deferred charge of less than 1% would be considered acceptable.

5.1.2 Origin of the CIC

One of the conclusions of Chapter 4 was that once CIC generated in the serial register and image-area dark current had been accounted for there was still between $0.005e^-$ and $0.007e^- \text{ pixel}^{-1}$ of charge remaining in the bias frames. It was suspected that a large fraction of this must originate within the EM register but this was not proven. In order to investigate this further, the CCD201 advanced model was run twice, firstly assuming that all the noise ($0.013e^-$) originated within the EM register and secondly assuming that it all originated pre-EM register. These models included the CTE value obtained in Section 5.1.1, which was initially overlooked with the result that it was impossible to obtain a fit between the model and real images for any mix of in-EM register and pre-EM register events. The effect of poor CTE was to increase the number of low-value events and decrease the number of high-value events. Other problems were encountered due to inaccurate measurement of the system gain of the camera. It was necessary to re-measure the system gain using the photometric technique (see Section 3.2); the histogram technique was unable to give sufficient accuracy. The histograms of these model images were then compared with that of an actual bias frame. This comparison is shown in Figure 5.1 and shows immediately that almost all of the CIC must originate within the EM register, since the real bias pixel histogram lies practically on top of the pure in-EM register CIC model. Various mixes of pre-EM-register and in-EM-register CIC were then tried until a best fit (as judged by eye), shown in Figure 5.2, to the actual bias image histogram was found. The result is somewhat at odds with the conclusions of Section 4.4.2 and shows that $0.011e^-$ originates within the EM register whilst only $0.002e^-$ originates prior to the register. This result casts into doubt the earlier measurements (Section 4.1.2) which seemed to show the presence of $0.005e^-$ of pre-EM register CIC, i.e. more than twice the total pre-EM-register signal from all



sources combined as predicted by this model. This could be explained if there was a dark current component to the pre-EM-register CIC that had not been correctly subtracted off.

5.1.3 Effect of imperfect CTE on the CIC

It was thought that CIC may have some component in the deferred charge left behind in the serial pipeline due to imperfect charge transfer. There was no direct evidence to support this but it was thought worthy of further investigation. No clear way of demonstrating this analytically could be found so it was decided to simulate its effect. In this model, the CIC and read-noise were set to zero and an artificial image generated with a bright vertical bar of mean illumination $1000 \text{ e}^- \text{ pixel}^{-1}$ at its centre. The serial register CTE was set to 0.999999 per transfer. Six images were generated with the EM-register CTE varying between 0.995 and 0.999999 per transfer. For each image the mean charge found >10 columns horizontally upstream of the bright vertical bar was measured. Once the CTE exceeded 0.999, it was found that this mean charge reached zero. Even at a CTE of 0.995 (unusably bad), the signal was on average $0.02 \text{ e}^- \text{ pixel}^{-1}$. This shows that although very poor CTE will clearly produce deferred charge in the first few columns following a bright pixel it will not raise the general background at all. The extremely long (100 columns) horizontal trails visible upstream of cosmic rays (see Figure 3.11) can therefore not originate from poor CTE. Instead they must be due to the steadily growing charge packet from the cosmic-ray affected pixel reaching such a size that it begins to interact with the surface of the CCD during its passage through the EM register. Part of the charge becomes trapped in mid-level surface states and then leaks back out into other pixels further upstream as they transfer through this cosmic-ray affected region. This is exactly the same process seen in parallel transfers when the pixel capacity is exceeded (see Section 3.5.7).

5.1.4 Visualisation of multiplication noise

The model was used to show how a charge packet grows as it moves through the EM register. This was used as an aid to visualise how multiplication noise arises. Figure 5.3 follows the passage of ten electrons through the EM register, each shown with a different color. Note the large spread in output values and how the final output signal is mainly dependent on the gain experienced during the first ~ 100 stages, i.e. the curves are approximately linear on this logarithmic plot. The graph also shows, as a thick black line, the mean value of a charge packet at each stage of the register. The equation that describes the growth of a single photoelectron after

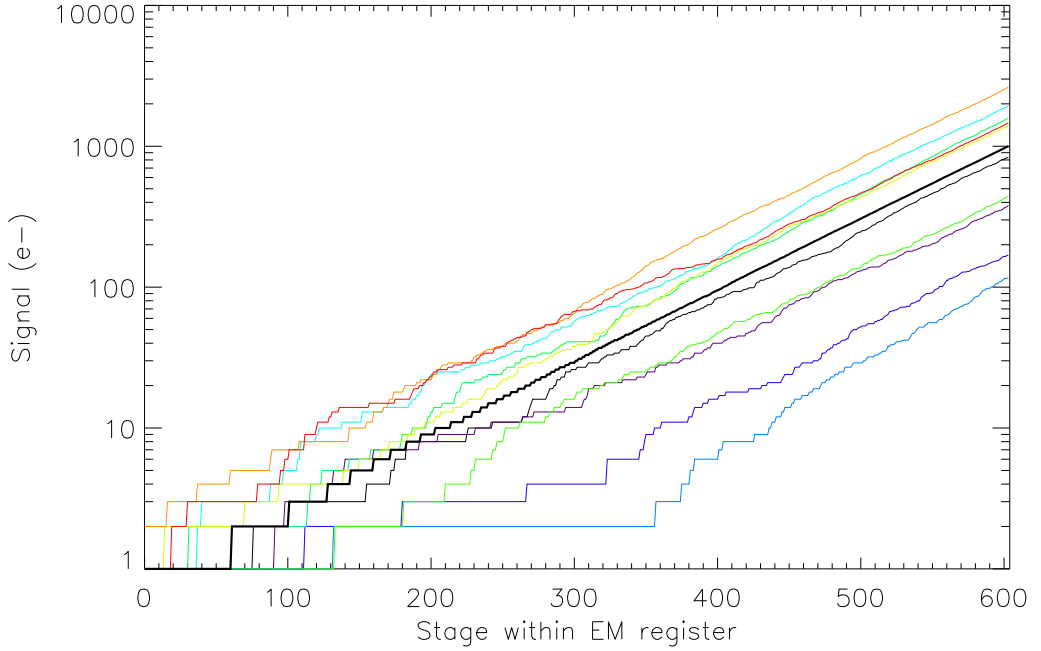


Figure 5.3: Growth of charge packets within the EM register. Ten electrons are followed through the EM register. Note the large spread in the corresponding output values. The average value of a charge packet that originates as a single photoelectron on its passage through the register is shown as a thick black line. The simulated EM avalanche multiplication gain was 1000.

passing through x elements of the EM register, already described in Equation 4.1 but reiterated here, is given by:

$$q_O = (1 + p)^x, \quad (5.1)$$

where p is the probability of gain per stage.

5.2 Modeling of PC operation

It was established earlier in Section 4.4.1 that the CIC rate of the optimised camera remained too high to give significant gains from switching to photon-counting operation. The question is how low do we need to push the CIC to make photon counting more useful? Using the Advanced Model we can now examine the performance of various hypothetical detectors with CIC rates as low as zero. Including this limiting value allows us to confirm the operation of the model since we would expect the SNR to be then equal to that of an ideal detector (see Equation 1.8).

The setting of the photon-counting threshold is extremely important for maximizing performance. Before starting the analysis we first need to consider the distribution of

event heights for both photoelectrons and CIC electrons and how these distributions vary with mean signal level and mean CIC level.

5.2.1 Statistics of photons

The generation of photoelectrons in the image area of the CCD is described by Poissonian statistics. The Poisson distribution describes the probability $P(M, n)$ that a pixel experiencing a mean illumination of M photoelectrons will receive a signal of n electrons. This is defined as follows:

$$P(M, n) = \frac{M^n \exp(-M)}{n!}. \quad (5.2)$$

Figure 5.4 shows this in colour scale form for mean illuminations M of up to $5 \text{ e}^- \text{ pixel}^{-1}$. For example, Figure 5.4 shows that if an image has a mean illumination of 1 photoelectron per pixel then any individual pixel will have a probability of ~ 0.37 of containing 1 electron, a probability of ~ 0.17 of containing two electrons and a probability of ~ 0.06 of containing 3 electrons.

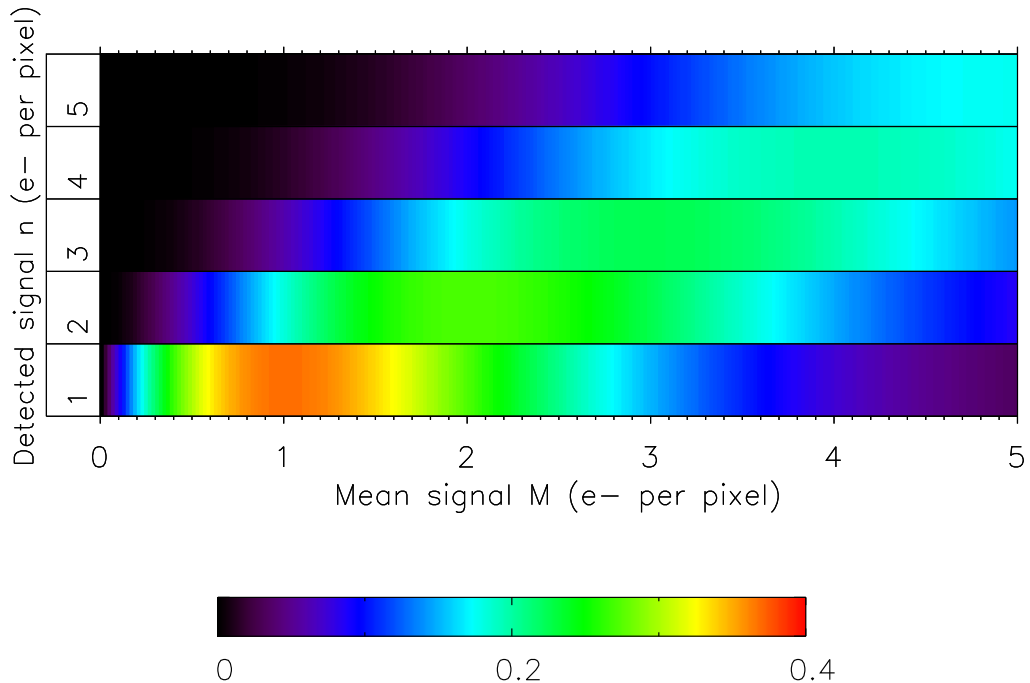


Figure 5.4: The Poisson distribution. The upper colour scale shows the probability $P(M, n)$ that a pixel will contain n photoelectrons as a function of mean exposure level M . Red codes for a probability of 0.4, black codes for zero, as shown in the lower colour scale.

5.2.2 Statistics of CIC

In this analysis only in-EM register CIC is considered. This is the overwhelming noise source in QUCAM2 (see Section 4.4.2) and it is assumed that any well optimised camera will be the same. The generation of CIC within the EM register can be described by the standard binomial probability equation:

$$P_n(k) = \frac{N!}{k!(N-k)!} p_{CEM}^k (1 - p_{CEM})^{N-k}, \quad (5.3)$$

where $P_n(k)$ is the probability of k electrons of CIC being generated within a pixel during its transit through the entire EM register, N is the total number of EM-register stages and p_{CEM} is the probability of CIC generation per EM-register transfer. The binomial distribution is shown graphically in Figure 5.5 for mean CIC levels, B_C , of up to 1 event per pixel. The y -axis only extends up to $3e^-$ since above this the probabilities are essentially zero. As an example, Figure 5.5 shows that if a pixel on average experiences 0.5 CIC events then there is a probability of ~ 0.3 that the pixel contains 1 CIC electron, a probability of ~ 0.07 that it contains 2 CIC electrons and a probability of ~ 0.01 that it contains 3 CIC electrons.

The p_{CEM} term had to be calculated at each mean CIC level before inserting it into Equation 5.3. This was done using the binomial property $B_C = p_{CEM}N$. The mean of the binomial distribution is then effectively B_C .

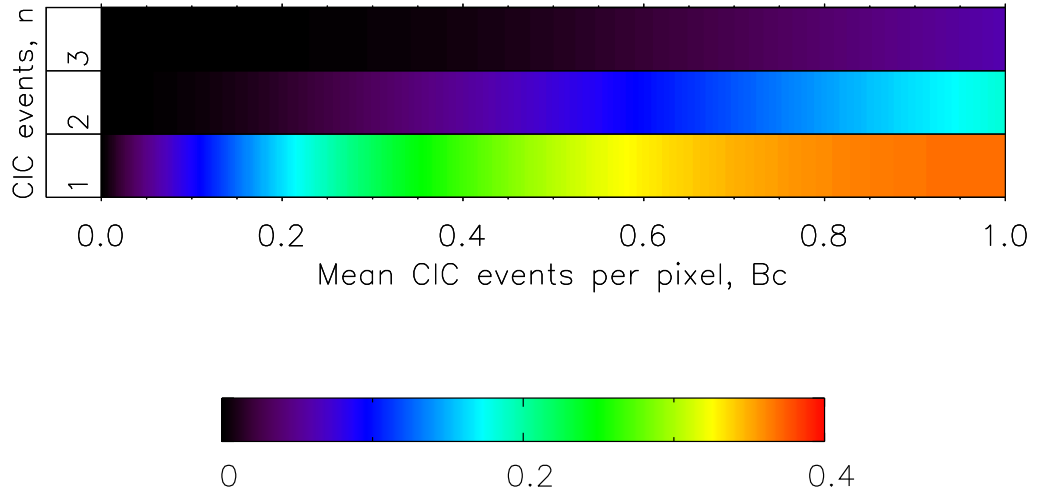


Figure 5.5: The binomial distribution. The upper colour scale shows the probability $P(B_C, n)$ that a pixel will contain n CIC events as a function of the mean number of events B_C experienced by a pixel on its passage through the EM register. Red codes for a probability of 0.4, black codes for zero, as shown in the lower colour scale.

5.2.3 The problem of threshold optimisation

Photon counting performance is limited by the presence of CIC. In the case of an EMCCD that has negligible CIC generated within the EM register then it is fairly simple to calculate the optimal threshold. It can be fixed at a level just high enough to avoid spurious counts from the read-noise. A level of 4σ is suitable since then only 1 pixel in 10^4 containing read-noise will be counted as a real photon. The EM gain must then be high enough to ensure that a large fraction (90% would be reasonable) of genuine photon events are counted, which (referring to Figure 4.15) requires the threshold to be no higher than about $0.1e^-$. This shows us that the effective read-noise (which is equal to the actual read-noise divided by the EM avalanche multiplication gain) must be less than $0.1/4 = 0.025 e^-$.

In the case of QUCAM2 the situation is rather more complicated since CIC generated within the EM register is actually the dominant noise source. Although a fixed threshold can be used, it is possible to dynamically tune its value to the mean signal-level present and gain a slight advantage. This is described and modeled in much greater detail in Section 4.4.1 but to summarise here: pre-EM register CIC will have *exactly* the same event height distribution as genuine photoelectron events, whereas in-EM register events will show an excess of low-value events. Moving the threshold will affect the detected fraction of CIC events differently to the detected fraction of photoelectron events.

Section 4.4.1 also shows that an excessively low threshold can actually cause a multiplication of the in-EM register events by greater than a factor of 1; the maximum factor, as the threshold approaches zero, is approximately $\ln[g_A] \sim 7$, where g_A is the avalanche multiplication gain. This is quite apart from the increase in noise that will be seen as the threshold starts to dip into the read-noise. The only unambiguous way to quantify CIC is to express the mean charge ν_C that it contributes to a pixel in a bias frame. This charge is best expressed in units of input-referenced photoelectrons so as not to imply any specific multiplication gain. To recap further, a mean in-register CIC charge of $0.01e^- \text{ pixel}^{-1}$ does *not* mean that 1 pixel in a hundred will contain a CIC electron. This mean of $0.01e^-$ is more likely to be composed of many smaller events (originating at intermediate positions in the EM register where they will not experience full multiplication) whose total size sums to an average of $0.01e^-$. If they are large enough to lie above the chosen PC threshold they will, however, be interpreted as ‘full’ electrons, hence the multiplication factor. It is important that this is appreciated if the rest of this chapter is to be fully understood.

In these models of photon-counting operation the per-pixel SNR was calculated as a function of three variables: the signal in mean photoelectrons per pixel, the CIC in mean charge per pixel and the threshold in fractional electrons. The CIC charge is

described as a photoelectron equivalent charge, i.e. it is described as an equivalent signal at the input to the EM register. For each combination of signal and CIC, the threshold value that gave maximum SNR was then located.

5.2.4 Generation of model signal frames

As raw material for the photon-counting simulations a series of images was generated containing just image-area photoelectrons with no CIC or read-noise present. Their generation was actually trivial, consisting of initialising a 2D array with all elements set to the same integer value. This ‘signal’ set consisted of a stack of 5 images, the first containing exactly 1 photoelectron per pixel ($n = 1$), the second 2 photoelectrons per pixel ($n = 2$) and so on (note that *no* pixel contained zero charge and the variance of each frame was zero). Use of these ‘maximally dense’ images boosted the computational efficiency of the model. The choice to only produce images up to $n = 5$ was taken to save time and could be justified since the probability of a single pixel receiving more than 5 photoelectrons in the photon counting regime (where the mean illumination is less than 1 photoelectron) would be entirely negligible.

These 5 images were then run through the simulated EM register to add the effects of multiplication noise. Each of the five multiplied images was then subjected to a varying photon-counting threshold and the number of pixels lying above each threshold value (effectively ‘counts’) recorded. The result was a 2D array of normalised count values (i.e. expressed as a fraction of the number of pixels in each frame) with threshold along the x -axis and input pixel-value (between 1 and 5 photoelectrons) along the y -axis, as shown in Figure 5.6. The range of thresholds examined extended up to $1e^-$ so as to cover fully the range of practical values. This range was actually more than sufficient since any PC system operated with a threshold of $1e^-$ will (referring to Figure 4.15) be hopelessly inefficient with $2/3$ of the photoelectrons being missed. The signal range of $5e^-$ was chosen to be high enough so that only a negligible number of pixels at the high-exposure end would fall under the maximum threshold. This is confirmed in Figure 5.6, where the top strip is fully red indicating that all events have been counted even at the highest threshold setting. Again this is somewhat higher than is actually needed since the coincidence losses (see Section 1.3.8) at this signal level would make photon-counting hopelessly inefficient. The array shown in Figure 5.6 can be interpreted as a series of cumulative distribution functions (CDF). Each row in the array represents the detected fraction of pixels containing various numbers of photoelectrons (1, 2, 3, 4 or $5e^-$ in this case) that lie above any given threshold. As an example, Figure 5.6 shows that if we use a threshold of 0.5 photoelectrons then there is a probability of ~ 0.6 that pixels containing 1 photoelectron will lie above the threshold and be detected. For pixels containing 2 photoelectrons, this probability rises to ~ 0.9 .

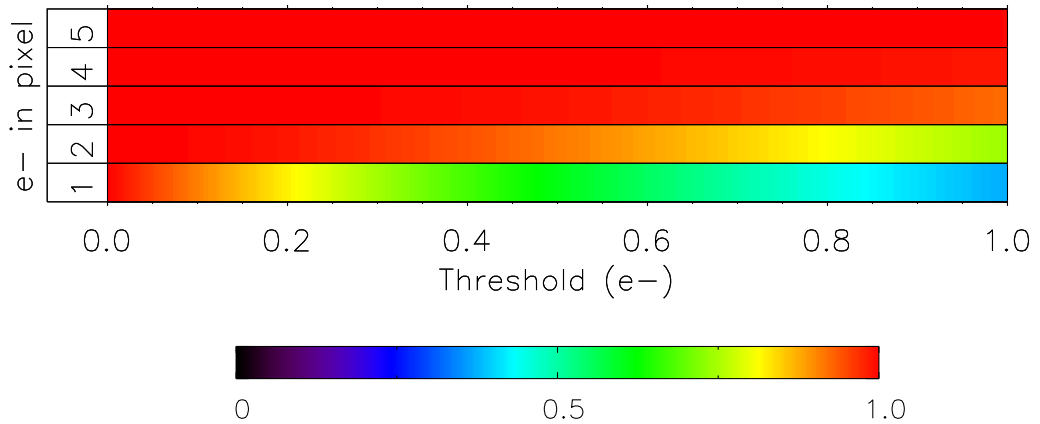


Figure 5.6: The fraction of pixels $C_P(t, n)$ containing n photoelectrons in an EMCCD image that will lie above a given threshold setting t , as obtained from a Monte Carlo model of an EMCCD. Red codes for a probability of 1, black for a probability of zero, as shown in the lower colour scale.

5.2.5 Generation of model CIC noise frames

Now a similar CDF array was constructed, this time using a set of frames containing only in-EM register CIC events and no photoelectrons. Whereas previously the signal frame pixels contained 1, 2, 3, 4 and 5 photoelectrons per pixel, this time we generated noise frames containing 1, 2, 3, 4 and 5 CIC *events* per pixel, i.e. frames containing pixels that had accumulated 1, 2, 3, 4 and 5 CIC electrons at random positions in their transit through the EM register.

The effect of multiplication noise on these events had to be simulated in a different way to improve computational efficiency. At the start of the readout of each simulated image row, the EM register was charged with a single electron per element. This simply amounted to initialising the array representing the EM register with each element equal to 1. This was then readout, simulating the effect of charge amplification, to yield an image with width equal to the length of the register. The resulting image was then scrambled (i.e. the pixels were reordered in a random fashion) and added to its original self to yield an image containing an average of 2 CIC events per pixel. This scrambling was necessary since the raw images contained pixels whose CIC content was approximately proportional to their column coordinate, with the pixels in the higher column numbers containing more charge. Further scramble-plus-addition operations were performed to yield images with on average 3, 4 and 5 events per pixel. It was not really necessary to go any higher than 5 CIC events since the binomial distribution graph (Figure 5.5) shows that there is an insignificant probability of more than 5 events being generated per pixel for *mean* CIC event levels of up to 1.0 per pixel, well beyond the useful operational range (indeed QUCAM2 gave ~ 0.08 CIC events per pixel).

The resulting output array, normalised in the same way as before by dividing by the number of pixels in the image, is shown in Figure 5.7. As an example Figure 5.7 shows that if we use a threshold of 0.1 photoelectrons then there is a probability of ~ 0.25 that pixels containing 1 CIC event will lie above the threshold and be detected. For pixels containing 2 CIC events this probability rises to ~ 0.4 . Note how the detected fraction falls away very rapidly with increasing threshold setting. Contrast this with the more gentle fall shown by photoelectrons in Figure 5.6.

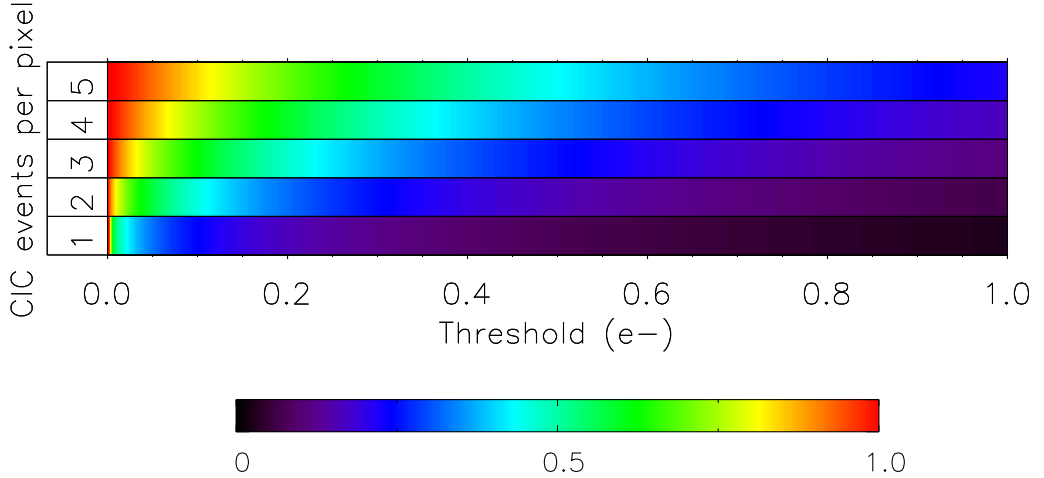


Figure 5.7: The fraction $C_C(t, n)$ of pixels affected by n in-EM register CIC events that are above a given threshold setting t . Pixels containing 1, 2, 3, 4 and 5 CIC events are shown. An ‘event’ in this case means an EM register transfer that generates one electron of CIC. Data obtained from a Monte Carlo model of an EMCCD. Red codes for a probability of 1, black for a probability of zero, as shown in the lower colour scale.

5.2.6 Effect of Gaussian read-noise

To be more realistic the effects of Gaussian read-noise (generated in the readout amplifier) were included in the model. It has two effects. First, it restricts how low we can set the photon-counting threshold. Second, it produces a slight blurring of the given threshold (the ‘fuzzy threshold’ effect), causing some pixels that lie just above it to fail to be counted and vice versa for pixels lying just beneath the threshold. The actual noise in the readout amplifier is given by σ . The effective read-noise will then be σ/g_A , i.e. divided by the avalanche multiplication gain. Although the read-noise can be pushed to very low levels by using high EM gain, it will never disappear entirely. A figure of $\sigma/g_A = 0.025e^-$ was chosen for the model, equal to that experienced by QUICAM2 and similar to that of other cameras examined (see Section 4.6).

It was not clear how to incorporate read-noise into SNR calculations in photon counting mode. According to Marsh (2008) it can simply be added in quadrature with the other noise sources. In general, however, if the threshold is placed well above the read-noise then it will simply not register except in the pixels that do contain a photoelectron. The average height of these photoelectron events will, of course, be 1 e^- regardless of the mean illumination level and the relative contribution of the read-noise should be much lower than the simple quadrature addition would predict.

The mechanism by which read-noise enters the photon-counting camera system can be visualised by considering the cumulative distribution function (CDF) of photo-electron events at the output of the EM register. This function shows what fraction P_d of photoelectron events are detected as a function of the photon counting threshold t , expressed in input referenced photoelectrons, and has the form $P_d = \exp(-t)$ (see Equation 1.9). One way to visualise the situation is that the read-noise does not affect the bias level but instead affects the threshold level: the bias remains steady and noise free but the threshold level is noisy and uncertain. In this way we can imagine that the read-noise is actually a ‘threshold noise’. The standard deviation of the detected fraction is therefore equal to the standard deviation in the threshold level (induced by the read-noise and measured in input-referenced electrons) multiplied by the gradient of P_d at our chosen threshold. This gradient is always between -1 and zero, although very close to -1 for the practical range of thresholds.

It was expected that the contribution of read-noise should be dependent in some way on the number of raw photon-counted images that are summed to yield the final analysable image. This is certainly the case when proportional images are added together, where the read-noise in the final image is simply equal to the read-noise in the individual frames multiplied by the square-root of the number of frames summed. A simulation was run in order to understand better the effects of the fuzzy threshold. The simulation generated 1000 weakly illuminated frames (with a mean signal of $0.05\text{e}^- \text{ pixel}^{-1} \text{ frame}^{-1}$) each containing 90,000 pixels that were then passed through a simulated EM register. These EM-amplified images were subjected to two analysis paths: in the first they were simply thresholded and the subsequent photon-counted images added to a running sum. After each addition the mean and the standard deviation of the running-sum image was recorded. In the second analysis path, the images had 0.05e^- of read-noise added to them prior to performing the thresholding and addition. At the end of the simulation it was then possible to see by what amount the standard deviation in the images had been increased by the read-noise. The threshold was placed quite high, at 5σ above the read-noise, so as to remove the effects of false triggers from bias pixels that may have otherwise confused the investigation. The output of the simulation is presented in Figure 5.8, and shows no increase in the standard deviation of the frames that had

the read-noise added.

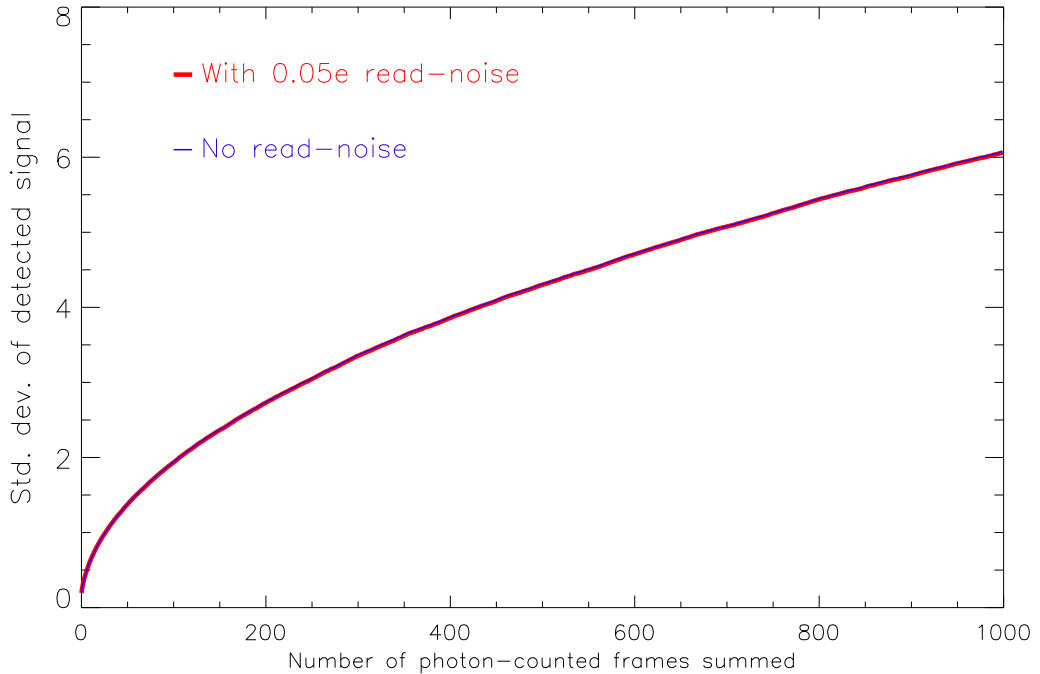


Figure 5.8: Gaussian read-noise in photon counting mode. This shows the effect of the ‘fuzzy threshold’. The two plots show how the standard deviation of the signal (as frames are successively combined) is related to its mean, both with and without the presence of 0.05e^- of read-noise ($=\sigma/g_A$). Each input frame had a mean illumination of $0.05\text{e}^- \text{ pixel}^{-1}$. The data points on the right-hand side of the graph represent photon-counted images produced by the summing of 1000 raw input frames. The threshold was set at 5σ so as to avoid the effects of false triggers from the read-noise.

The effect of false triggers when the threshold dips into the read-noise was then included in the model. This was done by generating a model noise image with a mean of zero and $\sigma/g_A = 0.025\text{e}^-$, corresponding to the actual read-noise of QUCAM2. This image was then subjected to a varying threshold and the fraction, C_G , of pixels lying above it measured. The result is shown in Figure 5.9 together with two other plots for two different levels of read-noise (for purposes of comparison). Note that if $\sigma/g_A = 0.025\text{e}^-$, then only one bias pixel in 3×10^{-5} will lie above a threshold of 0.1e^- .

The inclusion of these ‘false-trigger’ data in the photon-counting SNR calculations is described in more detail in Section 5.2.9. When calculating SNR in linear mode, read-noise was included in the usual way by adding in quadrature with the other noise sources.

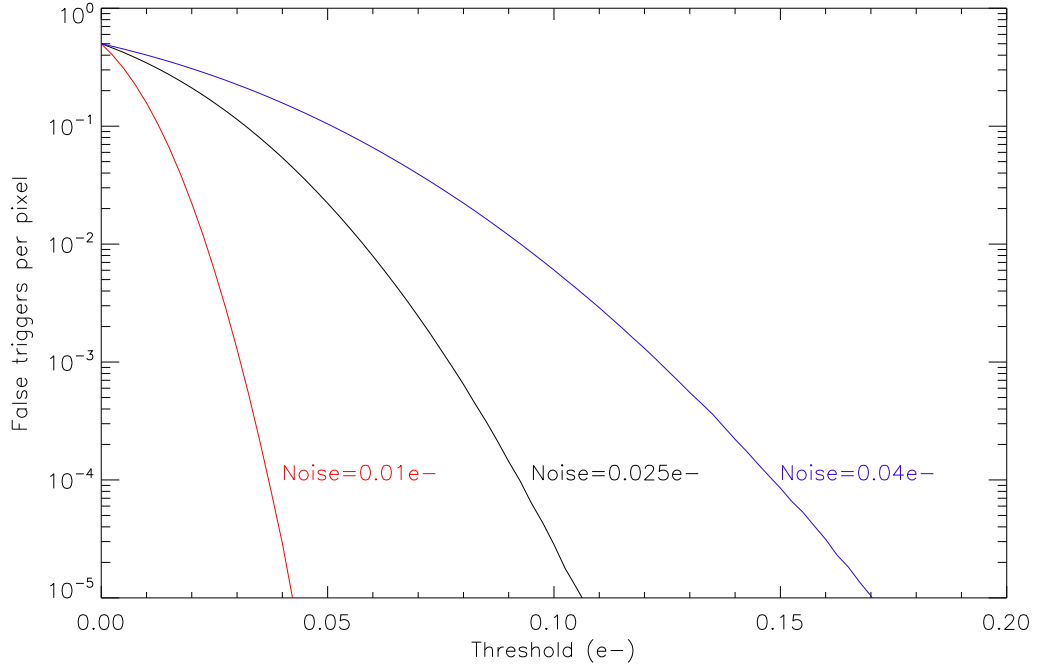


Figure 5.9: False triggers. The rate of false triggers, C_G , due to pixels containing only read-noise lying above the threshold is shown as a function of the threshold value. Three noise levels (σ/g_A) are shown, where 0.025e^- was the level experienced with QUCAM2.

5.2.7 Detected fraction of photoelectrons.

The two arrays representing the Poisson distribution, $P(M, n)$, and the cumulative distribution function, $C_P(t, n)$, for photoelectrons (Figures 5.4 and 5.6 respectively) can now be combined to yield the detected fraction $F_P(M, t)$ of photoelectrons as a function of the mean signal level M and the threshold setting t . The arrays are combined as follows:

$$F_P(M, t) = \sum_{n=1}^{\infty} \left[\frac{P(M, n) \cdot C_P(t, n)}{M} \right]. \quad (5.4)$$

Although the sum actually extends to infinity, it was actually only calculated up to $n = 50$. Since the maximum value for M that was considered was 10e^- (already well above sensible photon-counting levels but included for easier comparison with linear-mode performance), the probability of a pixel containing more than 50e^- was very small. The M in the denominator is included to normalise the result so that it expresses the detected fraction of photoelectrons. This makes the graphic more instructive since it highlights detail close to the origin which is where most operational photon-counting will be done. The array $F_P(M, t)$ is represented graphically in Figure 5.10. This figure makes sense: as we move to the right we see the effects of coincidence loss and as we move upwards we see the effect of an increasing proportion of the photoelectrons falling under the threshold. As one would expect, at the

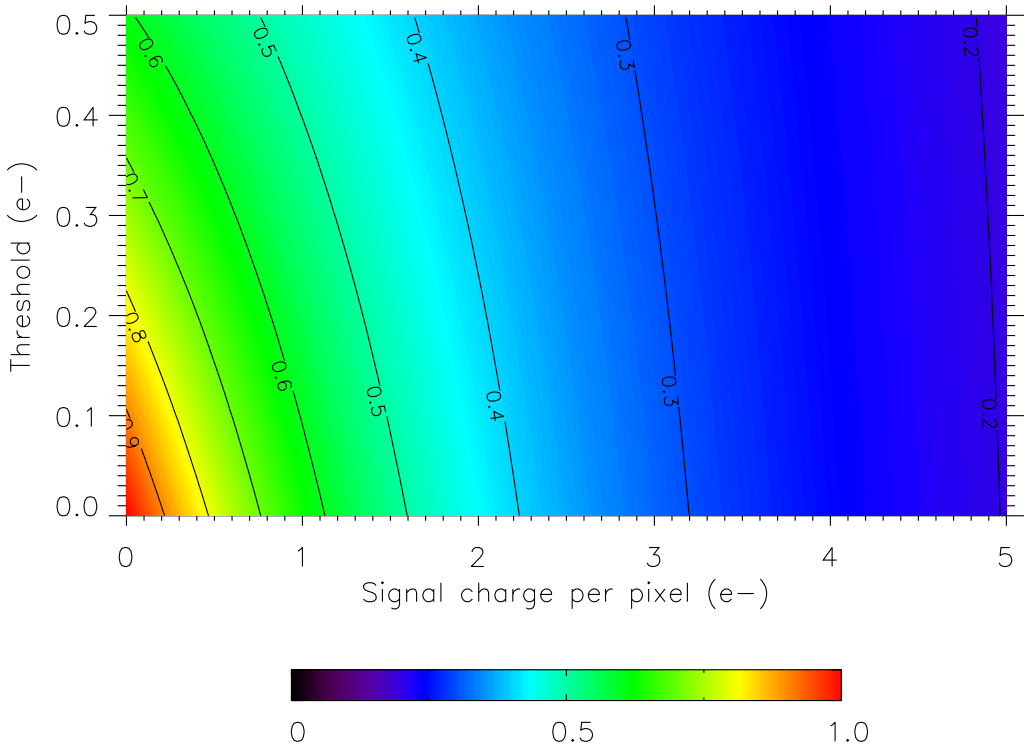


Figure 5.10: The detected fraction of photoelectrons F_P in a photon-counting EMCCD camera as a function of both the mean signal level M and the threshold t . Red codes for a probability of detection of 1, black for a probability of zero, as shown in the lower colour scale.

right-hand side where the mean exposure level is $5e^-$, the detected fraction is very close to 0.2, i.e. the 5 photoelectrons have been only counted as 1. Efficient photon counting is restricted to the small red region around the origin. As an example, the figure shows that if $M=3e^-$ and $t=0.1e^-$ then ~ 0.32 of the photoelectrons will be photon counted. Further confirmation of the accuracy of the result comes from a comparison with Figure 4.16. Both graphs show that at low-signal levels (where coincidence losses are insignificant) a threshold of $0.5e^-$ detects a fraction 0.6 of the photoelectrons.

5.2.8 Detected fraction of CIC events.

The two arrays representing $B(B_C, n)$, the binomial distribution and $C_C(t, n)$, the cumulative distribution function for CIC, can now be combined to yield the detected fraction $F_C(B_C, t)$ of CIC as a function of the mean in-register CIC events per-pixel, B_C , and the threshold t . The detected fraction of CIC events F_C is calculated as follows:

$$F_C(B_C, t) = \sum_{n=1}^{\infty} \left[\frac{B(B_C, n) \cdot C_C(t, n)}{B_C} \right]. \quad (5.5)$$

Once again the result is normalised, this time by dividing by B_C , so as to illustrate better the behaviour close to the origin. Also, although the sum is shown extending to $n = \infty$, it was actually only calculated up to $n = 5$ since above this level B was essentially zero across the practical range of B_C . The function $F_C(B_C, t)$ is represented graphically in Figure 5.11. As an example, this figure shows that if $B_C=0.08e^-$ (the value measured in QUCAM2) and $t=0.1e^-$ then ~ 0.25 of the CIC electrons will be photon counted. This is a good result since at this same threshold ~ 0.9 of the photoelectrons will be detected if coincidence losses are not present (see Figure 5.10). This demonstrates that a careful choice of threshold allows us to selectively filter most of the CIC events with only a small loss of genuine photoelectron events. It should be noted that this calculation of the detected

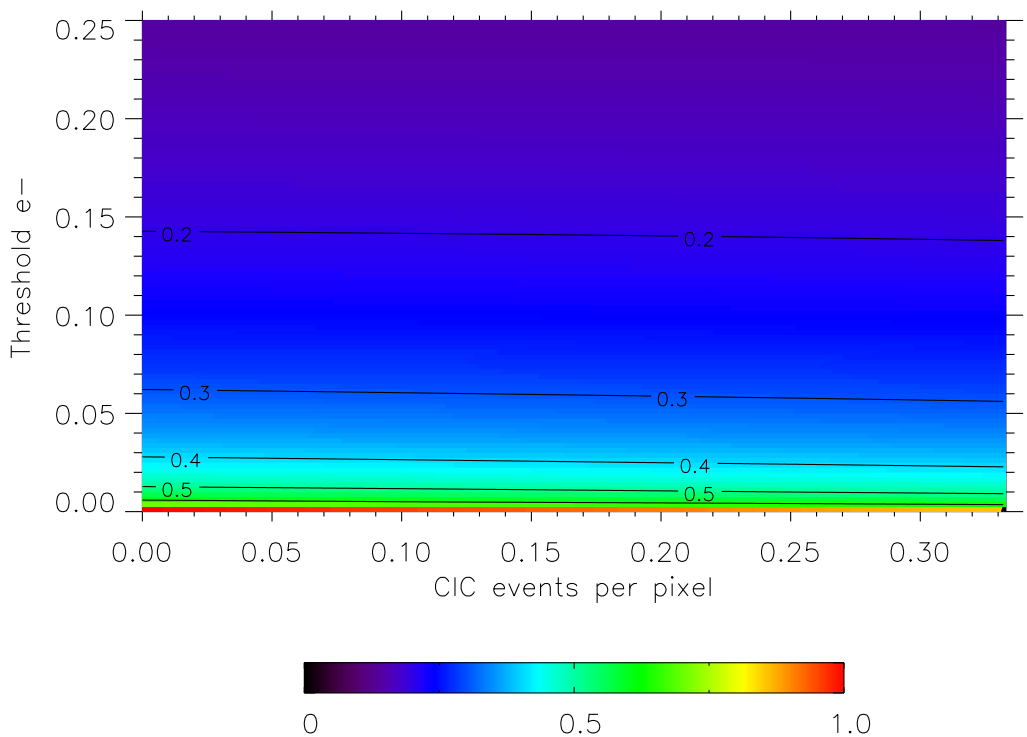


Figure 5.11: Colour scale showing the detected fraction of CIC, F_C , in a photon-counting EMCCD camera, as a function of both the mean number of CIC events per pixel B_C and the threshold t . Red codes for probability of detection = 1, black for a probability of zero, as shown in the lower colour scale.

fraction of CIC is based on units of mean events per pixel, i.e. the number of CIC events that a pixel will experience on average as it transits the full length of the EM register. This is not directly measurable from a bias frame. A more useful measure of CIC is the mean CIC charge per pixel ν_{CEM} . The relation between this and B_C has already been derived in Section 4.1.5. To reiterate:

$$\nu_{CEM} = \frac{p_{CEM}N[g_A - (1 + p)]}{g_A \ln g_A}, \quad (5.6)$$

where g_A = EM avalanche multiplication gain, p_{CEM} = per transfer CIC generation probability, N = number of EM register stages. Given that

$$B_C = p_{CEM}N, \quad (5.7)$$

we get

$$B_C = \frac{\nu_{CEM} g_A \ln g_A}{[g_A - (1 + p)]}. \quad (5.8)$$

Making the substitution

$$K = \frac{g_A \ln g_A}{[g_A - (1 + p)]}, \quad (5.9)$$

and rearranging, we get

$$\nu_{CEM} = B_C/K. \quad (5.10)$$

This conversion of B_C into ν_{CEM} is used to describe CIC in later sections. It should be stated once more that all the CIC is assumed to originate in the EM register, as should be the case for a well-optimised EMCCD.

5.2.9 Calculating photon-counting SNR

The SNR of an EMCCD in photon counting mode has already been shown in a simplified form in Equation 4.8. This is now made more realistic to include the detected fraction, F_P , of photons and, F_C , of CIC events, as well as C_G representing the false triggers from the read-noise, calculated in the previous sections. The resulting SNR equation is :

$$SNR_{PC}(M, B_C, t) = \frac{M \cdot F_P(M, t)}{\sqrt{M \cdot F_P(M, t) + B_C \cdot F_C(B_C, t) + C_G(t)}}. \quad (5.11)$$

5.2.10 Calculating linear-mode SNR

This is included here since in a study of photon-counting SNR it is useful to compare with SNR_L , the signal to noise ratio that would have been obtained in linear mode:

$$SNR_L = \frac{M}{\sqrt{2 \cdot (M + \nu_{CEM}) + (\sigma/g_A)^2}}. \quad (5.12)$$

Note the factor of 2 in the denominator to include the effects of multiplication noise. Here we use ν_{CEM} to describe the CIC (as opposed to B_C that was used in the photon-counting analysis).

5.2.11 Photon-counting performance of QUCAM2

The SNR was evaluated across the practical range of signal M , CIC level ν_{CEM} and for a range of thresholds t between 0 and $0.5e^-$. A read-noise of $50e^-$ was used since photon counting is done at high pixel rates where read-noise is much greater. An avalanche gain of 2000 was used. For each combination of M and ν_{CEM} the value of t that gave maximum SNR was selected. To make the results more accessible, the SNR was actually expressed as a fraction of SNR_{IDEAL} , the SNR that could be obtained from a perfect detector, i.e. one that gives $\text{SNR} = \sqrt{M}$. This hypothetical perfect detector was limited only by Poissonian photon noise and suffered no coincidence losses. The result is shown in the upper panel of Figure 5.12. This shows that with QUCAM2, which has $\nu_{CEM} = 0.01e^-$, for signal levels in the region of $0.1e^- \text{ pixel}^{-1}$, we can achieve an SNR equal to 80% of a perfect detector. If a way could be found to reduce the CIC to $0.001e^-$ then this figure might exceed 90%. We would then be limited by the read-noise which prevents the threshold being set low enough to include all of the signal events. The lower panel of Figure 5.12 shows the SNR of a photon counting EMCCD, this time compared with what could be achieved with linear mode operation. It shows that if the CIC is less than about $0.005 e^- \text{ pixel}^{-1}$ then for signals in the region of $0.1 e^-$ then photon counting can give as much as a 30% improvement in SNR compared to that achievable in linear mode.

The optimum threshold for each combination of signal per pixel, M , and CIC charge per pixel, ν_{CEM} , was then plotted on a separate contour graph, as shown in Figure 5.13. This shows that the optimal threshold for our camera is between 0.08 (3.2σ above read-noise) and 0.15 e^- (6σ above read-noise): a result reassuringly close to what was actually measured in Section 4.4.1.

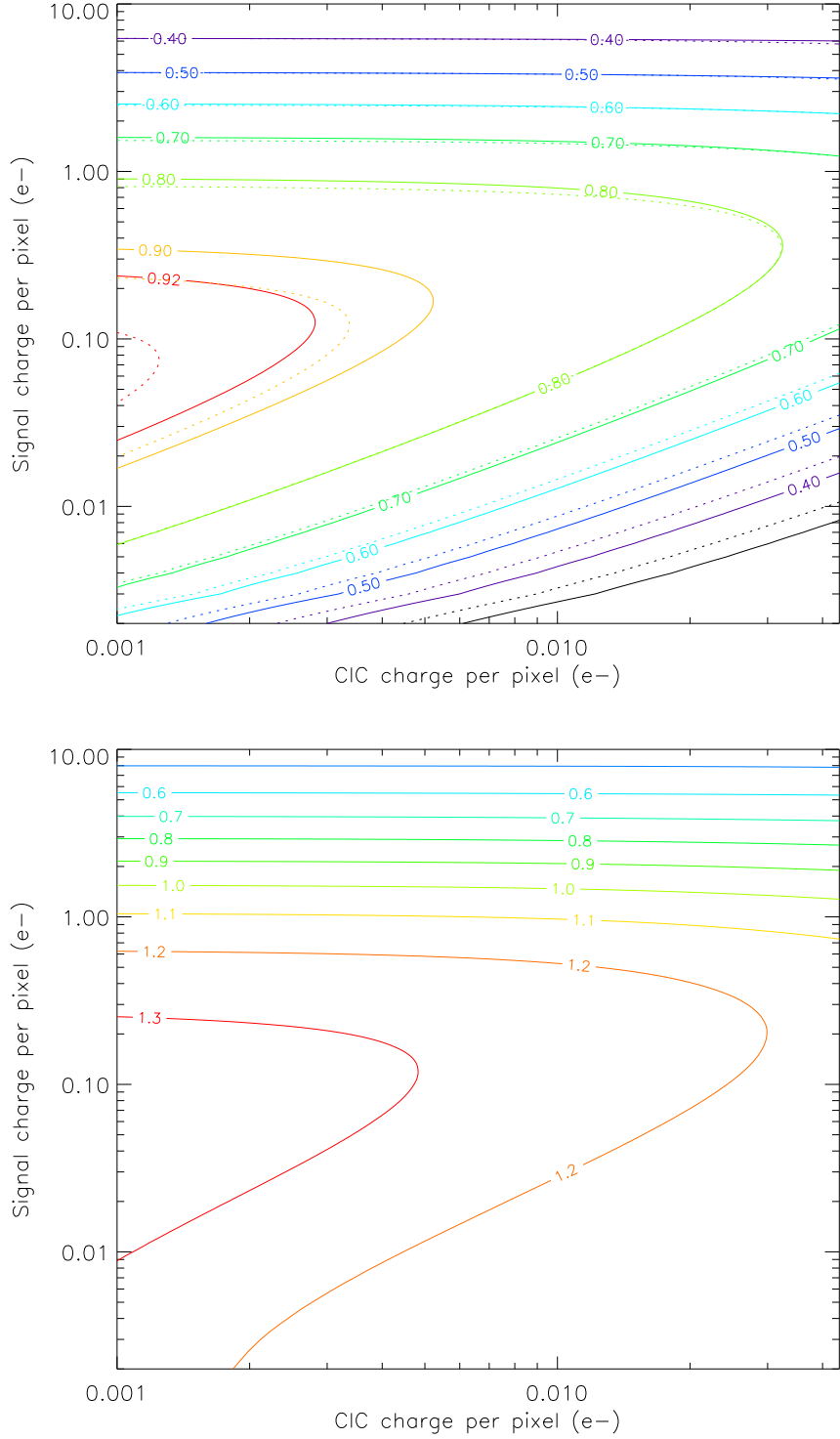


Figure 5.12: Comparing a photon counting EMCCD with both an ideal detector (top) and an EMCCD operated in linear mode (bottom). *Top:* The continuous contours are labeled with the $\text{SNR}_{PC}/\text{SNR}_{IDEAL}$. It was assumed that all the CIC was generated in the EM register, the read-noise was $50e^-$ and that the avalanche multiplication gain was 2000. The threshold has been optimised for each CIC and signal combination. The dotted lines show the result if a fixed threshold of $0.1e^-$ had instead been used.

Bottom: The contours show the $\text{SNR}_{PC}/\text{SNR}_L$ for a single exposure. The threshold has been optimised for each CIC and signal combination.

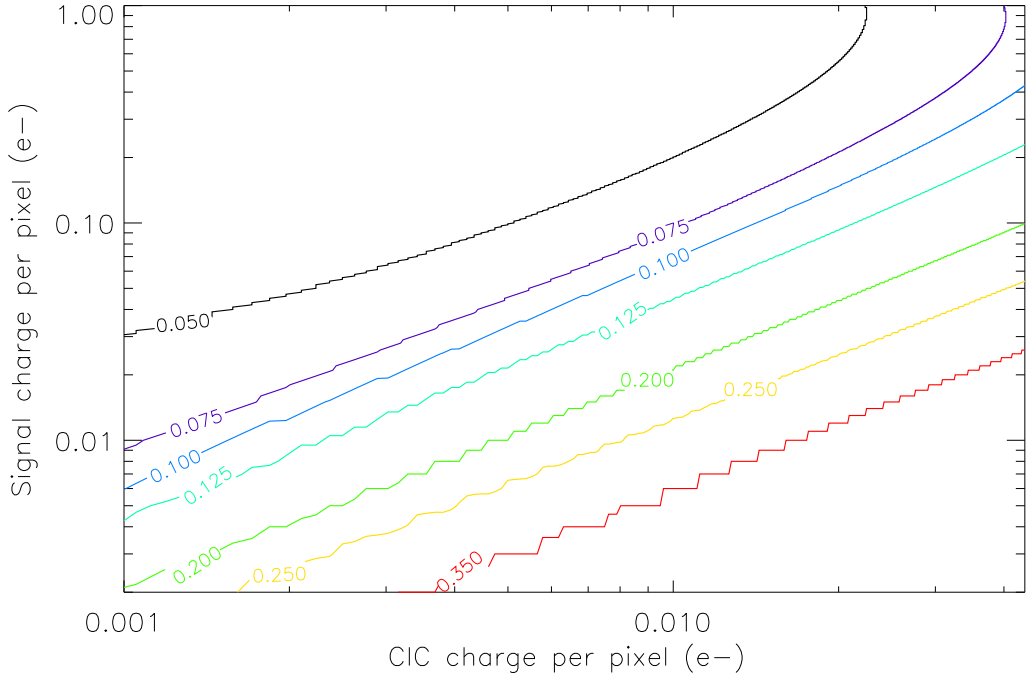


Figure 5.13: Optimum PC threshold in units of input-referenced photoelectrons. It was assumed that all the CIC was generated in the EM register, the read-noise was 50e^- and the avalanche multiplication gain was 2000.

In conclusion, the model results show that the CIC of the camera needs to be pushed to below 0.003e^- to be really useful for photon counting. If a way could be found to reduce this noise component then it would be necessary to make reductions to the read-noise to increase the SNR further. This could be done by reducing the intrinsic read-noise of the amplifier (by reducing the read-out speed) or by simply boosting the EM gain.

5.2.12 Practical photon counting

A single photon-counted image is not of much use. The SNR of a single pixel will never exceed 1 and so blocks of frames need to be summed together to produce an analysable image. The exact ‘blocking factor’, D , will depend on the brightness of the object we are observing and the time-resolution that we require. If we sum many photon-counted images together, whose total exposure time is equal to a single linear-mode image (i.e. one temporal bin), then the effective CIC will increase by a factor of D and the signal in each frame will decrease by the same factor. As D increases there will come a point where this extra CIC will degrade the photon-counting SNR advantage to such an extent that using the EMCCD in linear mode will give a better result. In linear mode we then see just a single frame’s-worth of CIC but of course suffer the SNR degradation produced by the multiplication noise.

The equation describing SNR achievable in photon-counting mode has already been stated in Equation 5.11. This now needs to be expanded to include the blocking factor, D , as shown in Equation 5.13. The mean photo-signal M is now taken to represent that received within one temporal bin, produced by either a single linear-mode image or D photon-counted images that have been thresholded and then summed. Both the CIC and the false triggers from the read-noise are therefore multiplied by a factor of D . In the case of the photoelectron events we must be careful to calculate the detected fraction for a mean signal of M/D *not* M . The SNR equation is therefore:

$$SNR_{PC}(M, B_C, t) = \frac{M \cdot F_P(M/D, t)}{\sqrt{M \cdot F_P(M/D, t) + D \cdot B_C \cdot F_C(B_C, t) + D \cdot C_G(t)}}. \quad (5.13)$$

The equivalent relation if we use linear mode, which was originally shown in Section 5.2.10, is reformulated here for comparison:

$$SNR_L = \frac{M}{\sqrt{2 \cdot (M + \nu_{CEM}) + (\sigma/g_A)^2}}, \quad (5.14)$$

these two equations were then combined as follows:

$$\frac{SNR_{PC}(M, B_C, t)}{SNR_L(M, B_C)} = \frac{F_P(M/D, t) \cdot \sqrt{2 \cdot (M + B_C/K) + (\sigma/g_A)^2}}{\sqrt{M \cdot F_P(M/D, t) + D \cdot B_C \cdot F_C(B_C, t) + D \cdot C_G(t)}}. \quad (5.15)$$

This equation was evaluated for a range of blocking factors up to 1000, which was seen as a reasonable limit for the number of photon-counted frames that would be blocked together in a practical situation. A series of output graphs (Figure 5.14) was then produced showing the SNR achieved with photon-counting relative to that achieved with a linear-mode analysis. The linear-mode CCD sees the signal M in a single frame whose exposure time is equal to the required temporal resolution. The photon-counting CCD, in contrast, produces an equivalent image consisting of D separate exposures each with a mean signal level = M/D . The result was somewhat surprising since it had been previously assumed that the effective multiplication of the CIC when using high blocking factors would make photon counting impractical. This turned out not to be the case and the only effect of the large blocking factors was to move the optimum region of PC operation to higher mean (per temporal-bin) signal levels.

The calculations were then repeated but this time comparing the photon counting

SNR with what could be obtained with an ideal detector. This is shown in Figure 5.14. Once again the large blocking factors merely moved the optimum photon counting region of operation to higher signal levels.

5.2.13 Photon counting: conclusions.

For photon counting to be effective the CIC charge in electrons per pixel should be below $0.003e^-$ and the EM gain should be high enough to push the effective read-noise (actual read-noise/ g_A) below $0.025e^-$. Once these conditions are met (none of the cameras analysed satisfied both conditions) then photon counting gives a 10–20 % advantage across a narrow operational range where the signal per frame is below about $0.6e^-$ per pixel. Above this we are restricted by coincidence losses, although this can be overcome by blocking together many shorter photon-counted frames taken at higher frame rates. At the low signal end of the range the photon counting EMCCD is limited by the CIC ‘ K -factor’ (see Equation 5.10) that effectively multiplies the significance of a CIC event when photon counting is used instead of linear mode operation. If we need to use large blocking factors with photon-counting then there must come a point where a single conventional CCD exposure, despite the relatively large read-noise component that it carries, will yield a superior SNR to the photon-counting EMCCD. This is demonstrated in Figure 5.16. Here the photon counting performance is compared with a conventional CCD of $3e^-$ read-noise. This shows that photon counting remains superior to the conventional CCD up to a signal of $\sim 3.5e^-$ per photon-counting frame. Taking the panel at top left in Figure 5.16 as an example, where the blocking factor $D = 3$, this shows that for a signal per-temporal-bin (M) above $10.5e^-$ the conventional CCD would be superior to photon-counting.

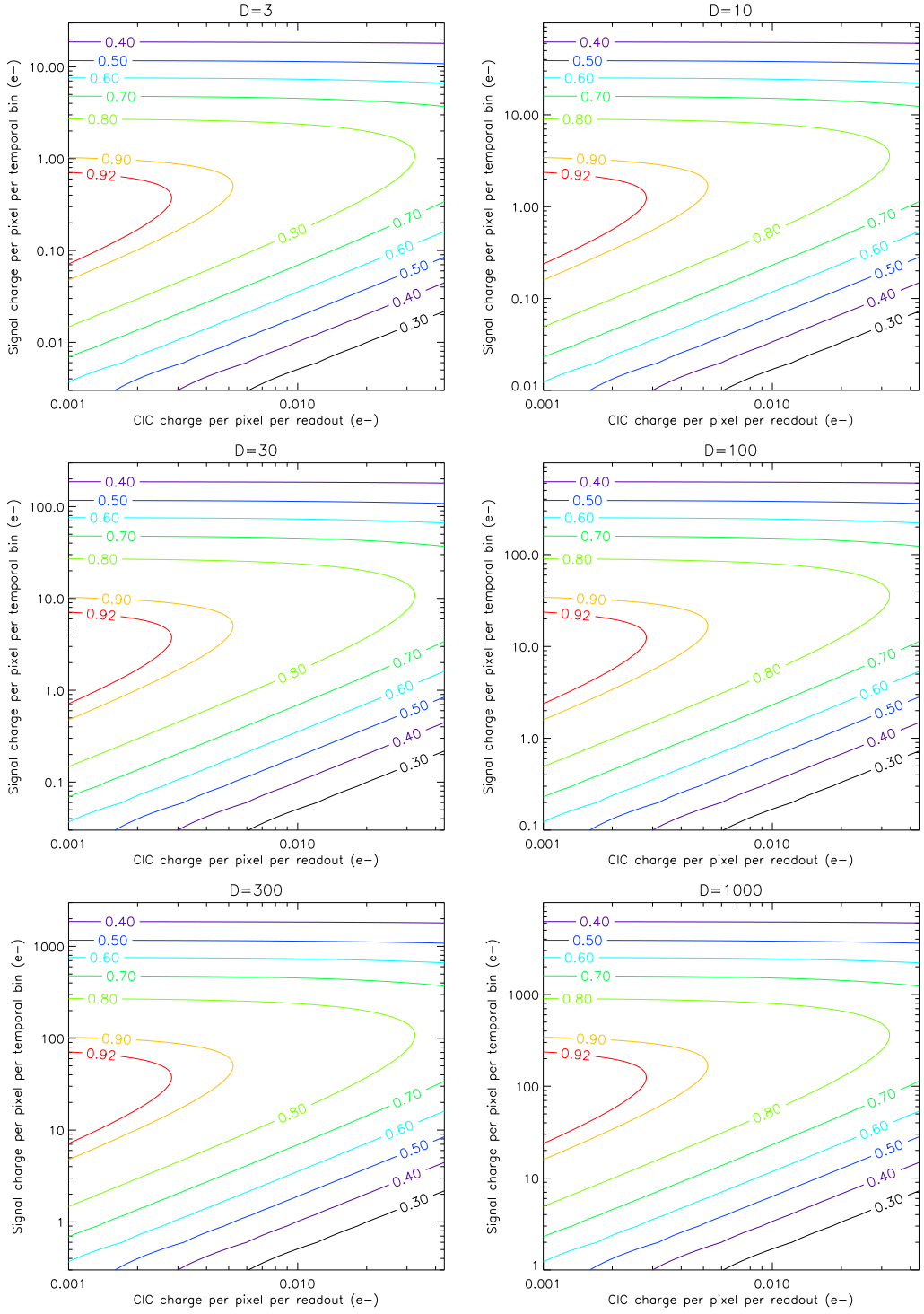


Figure 5.14: Comparing a photon counting EMCCD with an ideal detector. For each single ideal-detector exposure of T s, D separate photon-counted images each of exposure time T/D s are summed together. The contours show $\text{SNR}_{\text{PC}}/\text{SNR}_{\text{IDEAL}}$ for 6 values of D varying from 3 at top-left and 1000 at bottom-right. It was assumed that all the CIC was generated in the EM register, the read-noise was $50e^-$ and the multiplication gain was 2000. The threshold has been optimised for each CIC and signal combination.

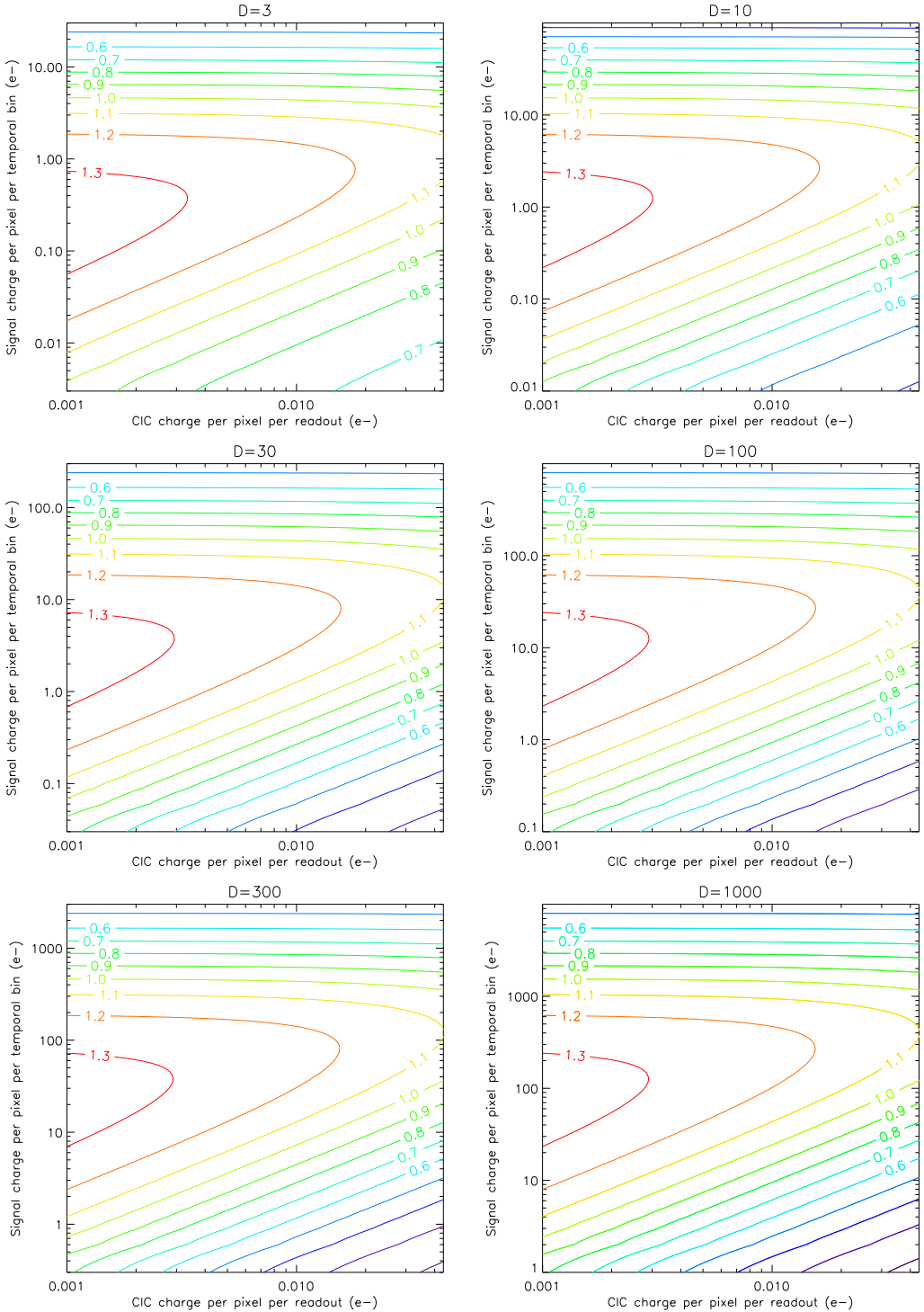


Figure 5.15: Comparing a photon counting EMCCD with one operated in linear mode. For each single linear-mode exposure of T s, D separate photon-counted images each of exposure time T/D s are summed together. The contours show $\text{SNR}_{\text{PC}}/\text{SNR}_L$ for 6 values of D varying from 3 at top-left to 1000 at bottom-right. It was assumed that all the CIC was generated in the EM register, the read-noise was $50e^-$ and the multiplication gain was 2000. The threshold has been optimised for each CIC and signal combination.

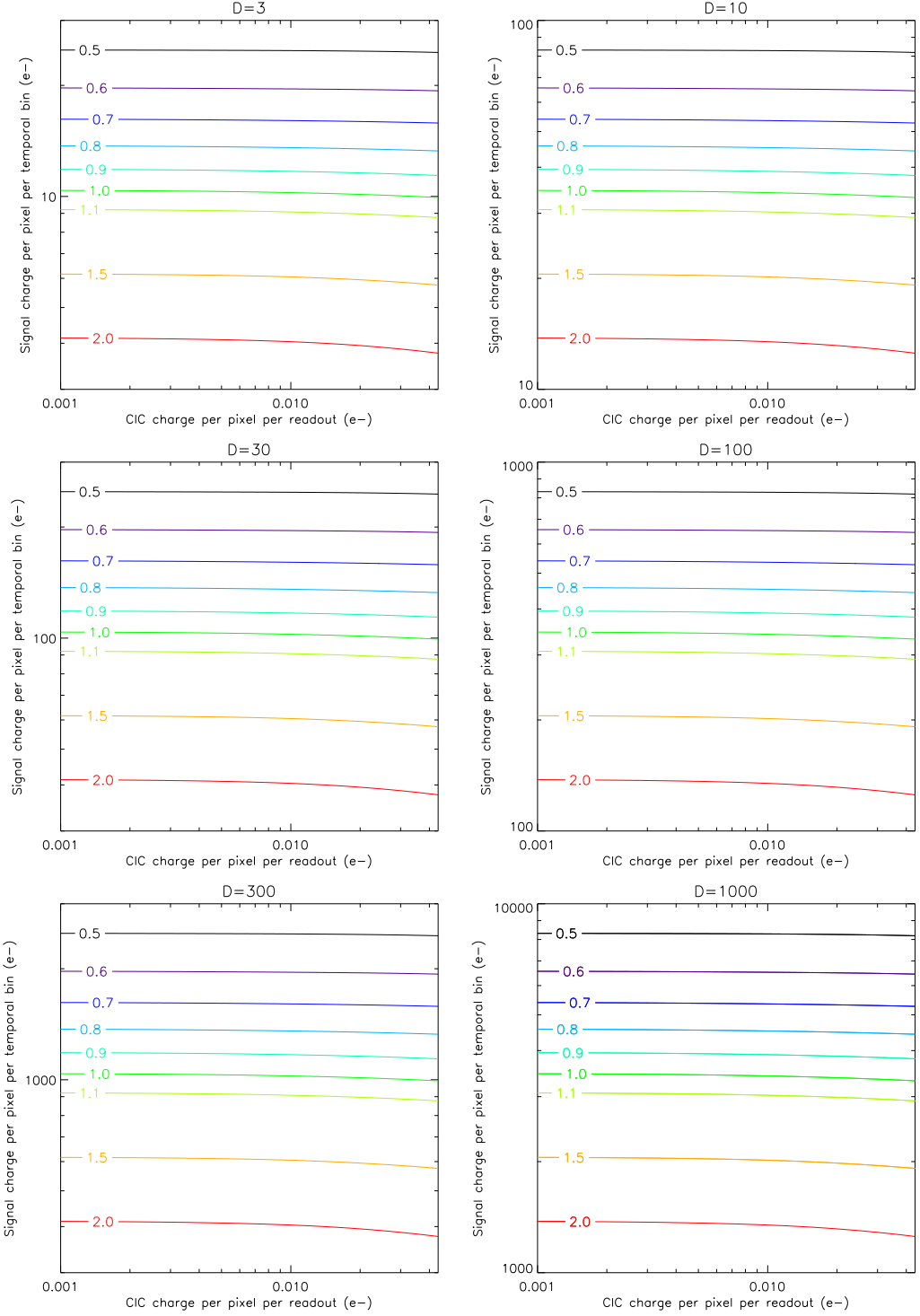


Figure 5.16: Comparing a photon counting EMCCD with a conventional CCD. For each single conventional CCD exposure of T s, D separate photon-counted images each of exposure time T/D s are summed together. The contours show $\text{SNR}_{\text{PPC}}/\text{SNR}_{\text{NORM}}$ for 6 values of D varying from 3 at top-left to 1000 at bottom-right. It was assumed that all the CIC was generated in the EM register, the read-noise in the conventional detector was $3e^-$ and the avalanche multiplication gain was 2000. The threshold has been optimised for each CIC and signal combination.

Part II

EMCCD Spectroscopic Observations

Chapter 6

The Nature of Cataclysmic Variables (CVs)

Having completed optimisation of the camera, it was then necessary to prove its operation with an actual astronomical observation. CVs were quickly identified as a class of object whose study could benefit greatly from the use of EMCCDs; they are faint, rapidly varying and spectroscopic observations are generally read-noise limited. In this chapter some of the key concepts in the astrophysics and evolution of CVs are introduced.

6.1 Introduction to CV systems

Cataclysmic Variables (CVs) are a class of binary star demonstrating a wide range of astrophysical processes. They consist of two stars orbiting about their mutual centre of gravity with periods ranging from a few minutes to >12 hours. Certain members of the class are thought to be progenitors of Type Ia Supernovae, although for the most part the large amplitude variability consists of smaller nova and dwarf nova outbursts. CVs contain a wide range of sub-classes, the common theme that unites them being that the primary star is a white dwarf (WD) accreting material from a less massive secondary generally termed the ‘donor’. Figure 6.1 shows how a CV would appear close up. In reality these objects are hundreds of light years distant and unresolvable as double stars. The fact that we have been able to infer their structure and appearance in such detail is a testament to the power of modern astronomical spectroscopy and high-time resolution photometry. Two excellent reviews of current knowledge on CVs are Hellier (2001) and Warner (1995).



Figure 6.1: Artists impression of a CV showing the secondary star donating material to the primary through a narrow gas stream. The primary is not directly visible in this representation, being drowned out by the light of the accretion disc that surrounds it. Courtesy of Mark Garlick (www.space-art.co.uk).

6.2 Origin of CVs

CV systems begin, as do most stars, as members of a gravitationally bound pair. Initial separations will typically be a few AU. More massive stars evolve more quickly and for those with a mass $<8M_{\odot}$ the WD generally represents the end point in stellar evolution. When stars exhaust the hydrogen in their cores their outer layers expand and cool producing a red giant star. The internal structure of the star then undergoes rapid evolution giving rise to instabilities that eventually result in the outer layers being ejected into space revealing the WD core composed of heavier elements, mainly carbon and oxygen. The WD is extremely dense, squeezing almost a solar mass of material into an object the size of the Earth. Its small surface area ensures that it takes many billions of years to cool down and fade from sight.

6.3 The common envelope phase

In the case of a binary star system in which one of the members reaches the red-giant stage, things are more interesting and further evolutionary processes can occur. As the more massive partner evolves into a red giant, its lighter partner continues on the main sequence (i.e. continues to burn hydrogen in its core). During the red-giant phase of the primary the secondary then finds itself orbiting within the primary's envelope which causes it to lose angular momentum through drag forces.

This braking process aids the ejection of the primary's envelope and can also result in an increase in the mass of the secondary as it captures the ejected material. At the end of this so-called 'Common Envelope' stage we find the secondary in a close orbit around the naked WD primary. The orbital separation will be $\sim 1R_\odot$, having started out at typically $\sim 100R_\odot$ (Hellier 2001).

6.4 Magnetic braking

There now commences a further phase of angular momentum loss as the secondary spirals towards the primary due to a phenomenon known as 'Magnetic Braking' (Schatzman 1962, Verbunt & Zwaan 1981, Rappaport et al. 1982). At this stage the component stars are sufficiently close to one another to become tidally locked in the same manner that the rotation of the Moon on its axis is locked to its orbital period around the earth. Any process that acts to reduce the spin angular momentum of the secondary will then necessarily reduce the system's total angular momentum. Magnetic braking is caused by the ionised stellar wind from the secondary. This wind tends to follow the magnetic field lines of the secondary star as it flows out into space. Since these field lines will be co-rotating with the star, ions will gradually acquire angular momentum as they move to ever increasing radii. This sling-shot effect carries away angular momentum at the expense of the star's rotational angular momentum. The tidal bulge raised on the secondary will then be slightly delayed in phase with respect to the orbital cycle and exert a gravitational torque on the primary producing a reduction in the orbital radius.

6.5 Mass transfer and the Roche lobe

Once the separation becomes sufficiently small, a new phase of evolution commences as the secondary star begins to completely fill its 'Roche lobe'. This is the region around the secondary within which material will be gravitationally bound to it. In a binary star system the lobe will be distorted into a teardrop shape by the gravity of the companion. As the stellar separation decreases due to magnetic braking the Roche lobe will approach the surface of the secondary star. The gravitational influence of the primary over the material in the very outer layers of the secondary grows steadily more significant until it equals the force binding that material to the secondary. The Roche lobe of the secondary is then filled.

The Roche lobe geometry of the CV SDSS J143317.78+101123.3 is shown in Figure 6.2. This plot shows the total potential Φ of a test particle in a frame-of-reference

that is co-rotating with the binary system with primary of mass M_1 and secondary of mass M_2 . It was calculated using the standard formula (e.g. Pringle 1981):

$$\Phi = -\frac{GM_1}{(x^2 + y^2 + z^2)^{1/2}} - \frac{GM_2}{[(x - a)^2 + y^2 + z^2]^{1/2}} - \frac{1}{2}\Omega^2[(x - \mu a)^2 + y^2], \quad (6.1)$$

where $\Omega = 2\pi/P_{orb}$ and $\mu = M_1/(M_1 + M_2)$. Here the x -axis connects the centres of the two stars and the y -axis lies in the direction of orbital motion of the secondary. The separation of the two stars is given by a and the orbital period by P_{orb} .

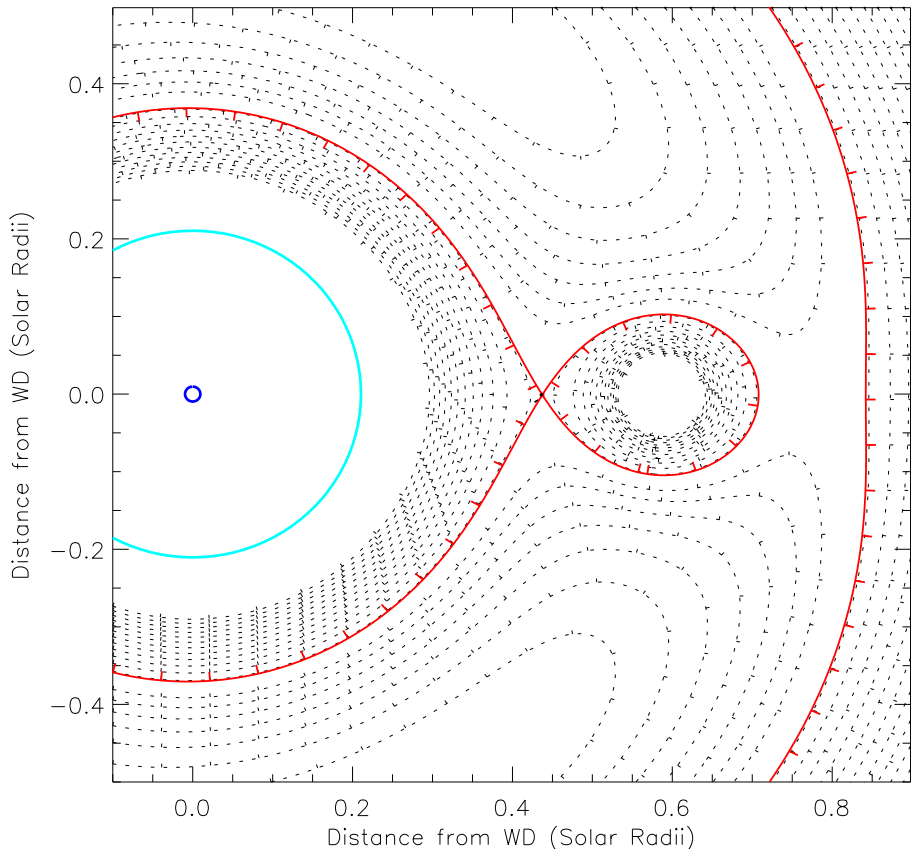


Figure 6.2: Equi-potential contours in the orbital plane of a CV. Calculated using the orbital parameters of SDSS J1433 given in table 7.1. The red contour shows the Roche lobes of the two stars. The secondary fills its Roche lobe whereas the primary (shown to scale as a small blue circle) lies well within its lobe. The turquoise circle shows the outer radius of the accretion disc. Contours closer to the stars are omitted for clarity. Coded by the author in IDL.

Any further reduction in orbital separation due to angular momentum loss, which causes a further shrinking in the size of the secondary's Roche lobe, then results in material spilling over from the secondary and becoming gravitationally bound to the primary (a physical expansion of the secondary star would have the same effect).

A narrow stream of gas passes through the point where the gravitational influence of the two stars is equal, known as the inner Lagrangian Point (L_1 , see Figure 6.3),

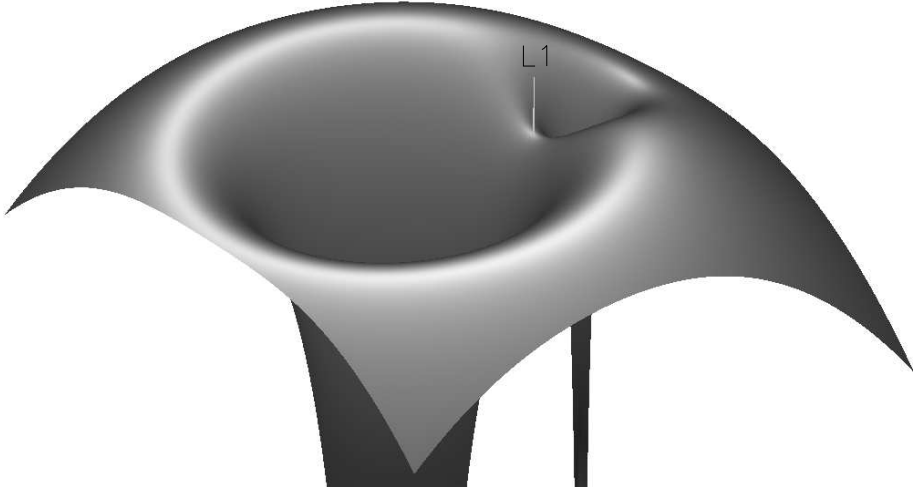


Figure 6.3: The Roche potential plotted for the system parameters of SDSS J1433 given in table 7.1. The surface shows the sum of the gravitational and rotational potentials. The saddle point between the potential wells of the binary components is known as the inner-Lagrangian point L_1 . Material from the secondary spills into the gravitational well of the primary via this point. Coded by the author in IDL.

and falls down into the gravitational well of the primary. Due to the conservation of angular momentum and the small size of the primary the transferred material does not directly impact the primary but instead moves in an elliptical orbit which loops back and collides with itself (Pringle 1981). The result is that a ring of accreted material forms around the primary. Viscous drag in the disc causes material to lose energy and gradually spiral down and impact the primary. Since angular momentum must be conserved, there is a corresponding outward movement of material, transforming the ring into a disc. Material at its outer edge can interact tidally with the donor shedding angular momentum in the process. Material from the accretion stream continues to impact the edge of the disc at high velocity producing a bright spot.

6.6 Emissions of CVs

The bright spot contributes a large fraction of the luminosity of the system. The bright spot and accretion disc emissions generally consist of the Balmer series emission lines of hydrogen superimposed upon a bright blue continuum. The WD primary contributes an additional continuum flux on which are superimposed pressure broadened absorption lines. The secondary is generally unobserved in the optical. Figure 7.1 shows a typical CV spectrum.

The majority of the optical emission from CVs is powered by the release of gravi-

tational potential energy as material spirals through the accretion disc and finally falls onto the primary star. Any variation in the accretion rate due to instabilities in the disc or through variations in the rate of gas flow from the secondary will cause variations in brightness. Additional modulations will occur as we observe the system at different orbital phases. In some cases we may even be lucky enough to observe the system at a very high inclination in which case it is possible to observe regular eclipses as the secondary passes in front of the accretion disc, bright spot and WD.

6.7 Orbital evolution and the period gap

For a secondary star on the main sequence, continued mass transfer will result in a reduction in the pressure at its centre. With less material pressing down on the core, the rate of nuclear reactions there will decrease. The star will respond by shrinking. The mass transfer will also cause a gradual accumulation of material on the surface of the WD. Accreted material, now bound to the WD rather than the donor, finds itself orbiting closer to the centre of gravity of the system. To conserve angular momentum the secondary is pushed out in its orbit and the period increases. The combination of a smaller secondary and an increased orbital radius means that the secondary's Roche lobe is no longer filled. The accretion rate should then drop off and the CV 'switch off'. However, magnetic braking continues to shed angular momentum and reduce the orbital separation. This shrinks the secondary's Roche lobe until it once again reaches the star's surface. Mass transfer will then continue but this time at a smaller orbital radius than before. Although explained here as a series of discrete processes, the movement to smaller orbital radii is of course a continuous process. The orbital period and hence the orbital separation of the CV continues to decrease in this way until it reaches approximately three hours. At this orbital period the secondary star will be left with a mass of approximately $0.3 M_{\odot}$. The star then becomes fully convective and it is believed that magnetic braking turns off and mass transfer stops (Robinson et al. 1981). The system thus reduces in luminosity and appears not as a CV but as a relatively inactive double star system.

The secondary continues to shrink further even though no mass transfer now occurs. This is because previous mass loss has occurred so rapidly that the star has not had time to reach equilibrium. If mass transfer were more leisurely the star would respond by cooling. There is a lot of heat to shed, however, and the thermal time constant of the star can be tens of millions of years. Once thermal equilibrium is finally established the secondary is well inside its Roche lobe.

In a close binary system there is, however, another mechanism for carrying off angular momentum. This is Gravitational Radiation (GR). Its effect (Paczyński, 1967) is

much weaker than that of magnetic braking but it continues to decrease the orbital separation of the stars once magnetic braking turns off at ~ 3 hours. Once the period reaches two hours the Roche lobe of the secondary touches its surface again, mass transfer resumes and the CV once again becomes observable. The histogram of CV periods in Figure 6.4 clearly shows a ‘period gap’: above three hours we see CV systems with large mass-transfer rates powered by magnetic braking, below two hours we see lower mass-transfer rate systems powered by GR. In between we see very few systems.

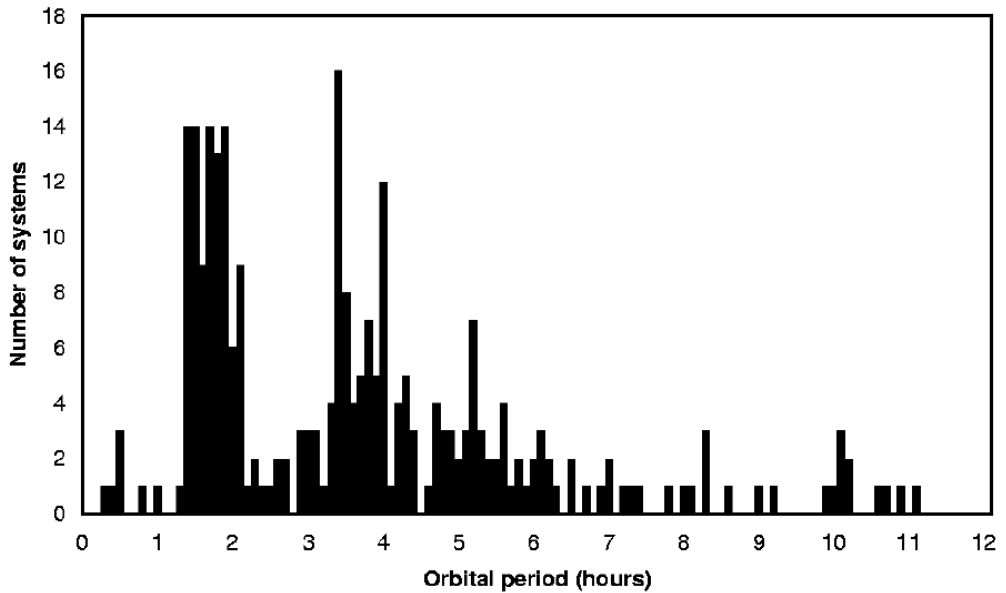


Figure 6.4: Histogram of observed CV periods showing the period gap between two and three hours (Ritter & Kolb 1998). Note also the very sudden decrease below periods of ~ 75 minutes (this is explained in Section 6.8).

6.8 Degenerate secondaries and the period bounce

In the case of the donor star not being on the main sequence, for example a WD or a brown dwarf (BD), further evolutionary variations are possible. Since WDs and BDs contain degenerate matter that does not obey ideal gas laws, any reduction in their mass due to mass transfer actually causes the star to expand and cool. Although mass transfer is a continuous process it is easier to describe what happens in a system with a degenerate secondary by imagining that mass transfer occurs in the form of discrete ‘blobs’ of material. Once a ‘blob’ is accreted, angular momentum conservation demands that the secondary moves out very slightly to a wider orbit. This will be accompanied by an expansion of both the secondary star and its Roche lobe. When gravitational wave losses bring the secondary back into contact with its Roche lobe and mass transfer continues, it will hence be at a slightly larger orbital

radius than before. The BD under consideration may either have formed as a BD or, alternatively, it could have started out as a main sequence star and transferred so much material to the primary that it is no longer able to support fusion at its core and subsequently *becomes* a BD. It has been calculated that a main sequence secondary star in a CV system will become degenerate at an orbital period of 78 minutes. Any further mass loss then results in a ‘period bounce’ , i.e. an increase in orbital period. We should therefore see no CVs with periods below this. This is backed up by observations as demonstrated in Figure 6.4. The handful of CVs with periods below 78 minutes are a special class of systems known as AM CVns in which the secondary is itself a white dwarf (Nelemans et al., 2001).

Beyond the ‘period bounce’, the steady increase in orbital radius causes a weakening in the GR emission from the system. Accretion rates steadily decrease and the system fades from view.

6.9 CVs as supernovae progenitors

Meanwhile at the surface of the WD an unstable situation can build up. The accreted material consisting of hydrogen and helium forms an extremely dense and hot layer at the WD surface. The material is highly compressed by the intense gravity of the WD and heated by the continual rain of accreted material from above. A point is reached where the conditions for thermonuclear fusion are satisfied and this hot layer then undergoes a thermonuclear flash as the material ignites. An expanding fireball is then visible to us as a nova explosion. After this event the system returns to normal and mass transfer continues. The process can thus recur many times with intervals believed to range from years up to $\sim 10,000$ years. If the nova does not remove all of the accreted material from the WD surface, and if the secondary star is able to continue supplying sufficient material, then the WD mass will increase until it reaches the Chandrasekhar limit ($1.4M_{\odot}$). At this point runaway carbon fusion in the core completely destroys the star in a Type Ia Supernova. These events provide an extremely valuable standard-candle for establishing cosmological distances; not only are they extremely bright (as bright as our galaxy) but all Type Ia supernovae will have progenitors of equal mass and therefore release the same amount of energy when they explode. Another evolutionary route to Type Ia supernovae has recently been proposed involving the merger of two white dwarfs (Pakmor et al. 2010).

6.10 Magnetic CVs

Another interesting variant of CVs can be found when the WD is highly magnetic. This prevents the formation of an accretion disc since accreted material in the vicinity of the WD has its motion dominated by magnetic rather than gravitational forces. Incoming material is forced to follow the magnetic field lines that guide it directly onto the magnetic poles of the WD. The gravitational energy of this accreting material is thus released suddenly rather than gradually in a slow spiral down through an accretion disc. The subsequent shock heating is more intense and the object emits X-rays. Such objects are known as ‘Polars’.

6.11 Eclipsing CVs

Because CVs have such small orbital separations there is a reasonable chance of the orbital inclination being high enough to produce eclipses. Eclipsing CVs are of great value to astronomers and several hundred have been observed so far (Ritter & Kolb 1998). They can of course be identified photometrically if the orbital period is short enough but it is also possible to identify high-inclination systems spectroscopically. The material in the accretion disc rotates at velocities of up to $\sim 4000 \text{ km s}^{-1}$. This produces a Doppler splitting of its emission, with one side of the disc being red-shifted and the opposite side blue-shifted (see Figure 7.1). If the observer happens to be close to the plane of the disc then its emission lines will appear to be split. This is shown in Figure 6.5 where the radial velocities of the disc material are colour-coded.

The outer wings of the emission correspond to material orbiting closer to the WD. As can be seen from Figure 6.11 this corresponds to a very small area of the disc as a whole. In contrast, the core emission which is mainly emitted by material at larger radii with a lower orbital velocity and lower Doppler shift, originates from a relatively large fraction of the disc area. Since the accretion disc and secondary star orbit within the same plane, an object that displays split spectral lines has a high probability of displaying eclipses when later observed photometrically. In non-eclipsing systems, it is very hard to pin-down certain key parameters such as the mass of the components and their orbital velocities. This is due to uncertainty about their inclination i . If instead we observe an eclipse then we can measure i assuming that we first have knowledge of the mass ratio of the binary system (Dhillon et al. 1991). Other important clues are obtained due to the fact that the secondary sequentially eclipses the disc, WD and bright spot. The light curve around eclipse is thus quite complex and if studied at high time resolution (e.g. Littlefair et al.

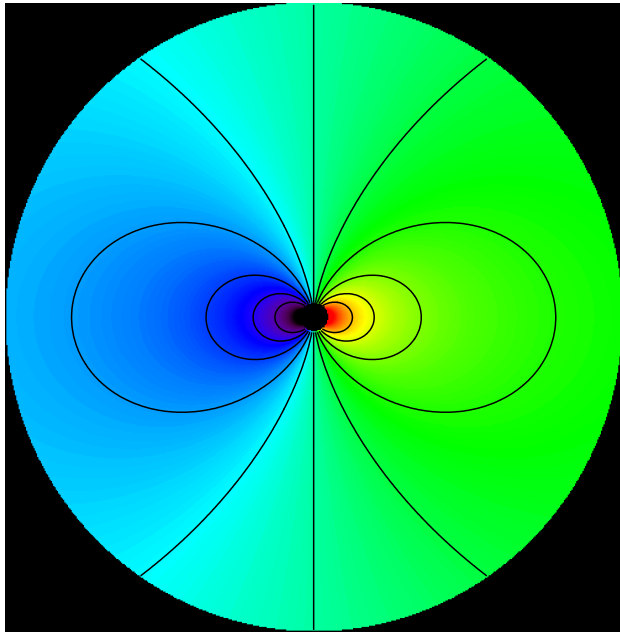


Figure 6.5: The Keplerian radial-velocity distribution of material in an accretion disc. The observer is within the plane of the diagram, at the bottom. The radial velocities are encoded using colours that show the Doppler shifts produced by the orbital motion. The orbital velocity of material in the disc varies between $\sim 900 \text{ km s}^{-1}$ at the outer edge to $\sim 4000 \text{ km s}^{-1}$ close to the WD. In reality this Keplerian velocity distribution will be modified by viscous forces and gas pressure within the disc material. Contours are spaced at intervals of 500 km s^{-1} (relative to the line of sight). Coded by the author in IDL.

2006) the timings can yield most of the system parameters: mass ratio, inclination, disc radius, component radii, masses, separation and period.

Given the large number of astrophysical phenomena that they display, it should now be apparent why CVs are of such interest to astronomers.

Chapter 7

EMCCD observations of the cataclysmic variable **SDSS J143317.78+101123.3**

The material in this chapter has been published in the paper by Tulloch et al. (2009). The majority of the observation was carried out by Pablo Rodríguez-Gil. I prepared the instrument and camera, planned the observations, reduced the data and carried out the data analysis with the assistance of Vik Dhillon.

To demonstrate the unique capabilities of QUCAM2, an object was chosen that would have been impossible to observe with a conventional detector. The eclipsing cataclysmic variable SDSS J143317.78+101123.3 (hereafter SDSS J1433) was identified as a suitable target. This object has been studied photometrically by Littlefair et al. (2008) using the ULTRACAM instrument (Dhillon et al. 2007) and by Szkody et al. (2007) but has never been the subject of high time-resolution spectroscopy. It was sufficiently faint ($g' = 18.5$) to put it beyond the reach of high time-resolution intermediate dispersion spectroscopy with a conventional detector on the WHT. Its orbital period of 78.1 min allows several orbits of data obtained in a night to be phase binned in order to improve the SNR.

SDSS J1433 was shown by Littlefair et al. (2008) to contain a brown-dwarf mass donor star; one of only 4 known cases. It was thus of considerable current interest and was fortuitously placed on the night that we had access to the telescope. Models show that up to 70% of all CVs in the Galaxy should have brown-dwarf secondary stars at the present time, yet not a single such object had been positively identified until the discovery by Littlefair et al. (2006) of a secondary star of mass $M_2 = 0.052 \pm 0.002 M_\odot$ in the CV SDSS J103533.03+055158.4. Another brown-dwarf mass donor has been discovered by Littlefair et al. (2007), SDSS J150722.30+523039.8 and

it now appears as if the missing population of post-period minimum CVs has finally been identified.

The results of Littlefair et al. (2008) and Littlefair et al. (2006) rely on an eclipse light-curve fitting technique applied to broad-band photometric data. The assumptions underlying this technique appear to be robust (see Littlefair et al. (2008) for a discussion), but the results are of such significance that it is important they are independently verified.

The motivation of these observations was to obtain time-resolved spectroscopy of the CV SDSS J143317.78+101123.3 (hereafter SDSSJ1433), with the aim of measuring the radial-velocity semi-amplitude of the white dwarf (K_W) and comparing this direct, dynamical measurement of K_W with that predicted by the light-curve model of Littlefair et al. (2008).

7.1 What is known already about SDSS J1433

The spectrum of SDSS J1433 is shown in Figure 7.1, taken from the Sloan Digital Sky Survey ¹ web page. The ULTRACAM results are shown in Table 7.1, copied directly from Littlefair et al. (2008).

Table 7.1: Previously known parameters for SDSS J1433 based upon photometric observations. From Littlefair et al. (2008)

Parameter	Value
Inclination i (degrees)	84.2 ± 0.2
Mass ratio q	0.069 ± 0.003
White dwarf mass M_W/M_\odot	0.868 ± 0.007
Secondary mass M_R/M_\odot	0.060 ± 0.003
White dwarf radius R_W/R_\odot	0.00958 ± 0.00008
Secondary radius R_R/R_\odot	0.109 ± 0.003
Separation a/R_\odot	0.588 ± 0.002
White dwarf radial velocity $K_W/\text{km s}^{-1}$	35 ± 2
Secondary radial velocity $K_R/\text{km s}^{-1}$	511 ± 2
Outer disc radius R_D/a	0.358 ± 0.001
White dwarf temperature T_W/K	12800 ± 200
Distance (pc)	246 ± 10

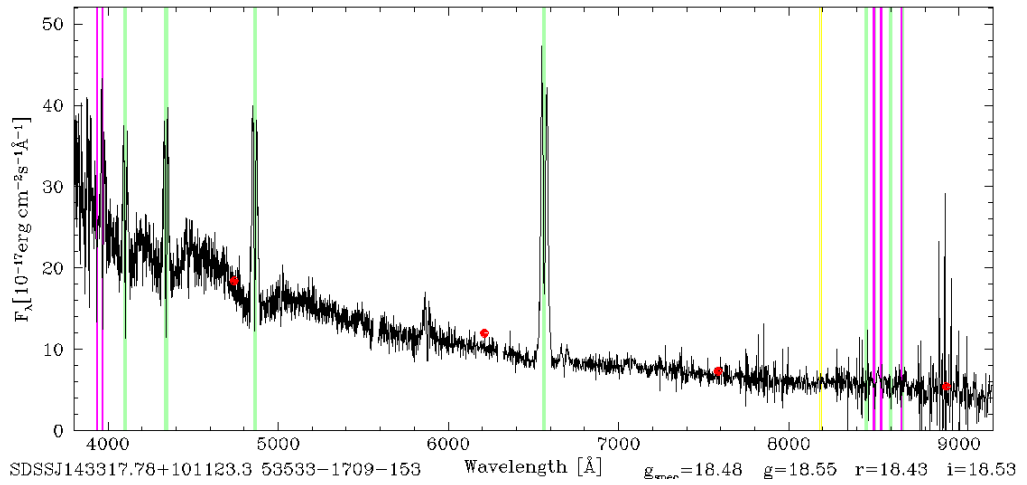


Figure 7.1: Spectrum of SDSS J1433 showing the double-peaked spectral lines typical of an eclipsing CV system. The vertical lines indicate the position of Balmer line emissions from hydrogen. Taken from the Sloan Digital Sky Survey web page.

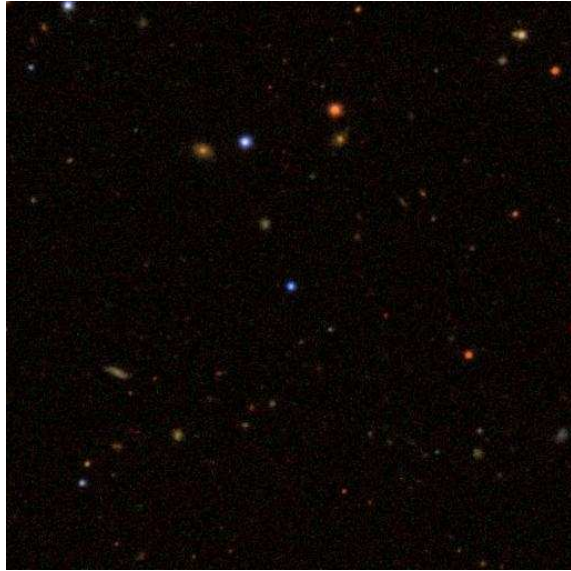


Figure 7.2: The finding chart for SDSS J1433. The target is the blue star at the centre of the image. The reference star was the brightest red star at top-middle. The image is 3.3 arcmin on each side with North up and East to the left. The field is within the constellation Boötes.

7.2 Observations and reduction

We observed SDSS J1433 using the red arm of the ISIS spectrograph on the WHT on April 16th 2008. Atmospheric conditions were variable with $\sim 1''$ seeing. We were severely limited by the presence of a nearly full moon. The sky brightness was in the region of $0.01 \text{e}^- \text{ pixel}^{-1}$ per second, similar to the continuum brightness of the

¹SDSS: <http://www.sdss.org/>

CV. Given the low predicted K_W of $35 \pm 2 \text{ km s}^{-1}$ it was decided to use the highest dispersion grating available (R1200R) giving a wavelength range of $6480\text{--}6700\text{\AA}$, sufficient only to include the H α and He I emission lines. It was decided to focus the observations on the H α emission line since it is the stronger line. A 1" slit was used giving a spectral resolution of 32 km s^{-1} (0.7\AA). In the spatial direction the detector was rather limited (~ 2 arcmin) but a suitable reference star was found about an arc-minute away and positioned on the spectrograph slit. The spatial separation of the two stars required that the full CCD frame was read out with no windowing. Spectra were taken in groups of eighty 30 second exposures. Seven groups in all were taken, interleaved with argon arc spectra for wavelength calibration, covering about 4 orbital periods. Flat fields using a tungsten lamp and several hundred bias frames were also taken at the end of the night. No flux standard was observed. This was justified because there was intermittent cloud, we only observed over a narrow wavelength range and we were only interested in extracting velocities from the data.

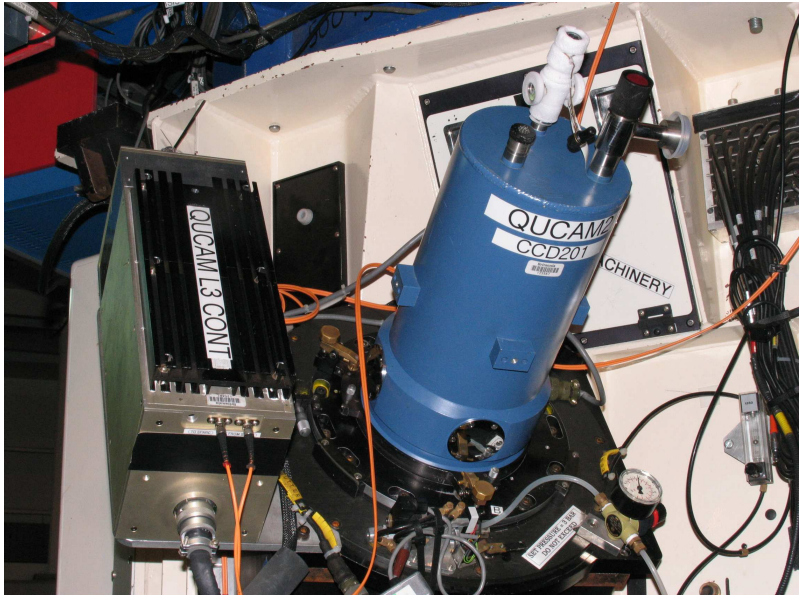


Figure 7.3: QUCAM2 mounted on the red arm of the ISIS spectrograph ready for observations. The camera controller is shown mounted close by on the left.

The spectra were extracted using a simple spatial bin across three windows within each frame covering the target, the reference star and the large area of sky between them. The sky-subtracted spectra were cast into 40 phase bins using the ephemeris of Littlefair et al. (2008), and then corrected for slit losses and transparency variations by dividing by the integrated flux in the comparison star spectra. The bias frames were not used in the reduction. The bias was determined instead from a measurement of the median pixel value in the sparsely illuminated science frames. With a conventional CCD the bias is normally determined from pixels in the underscan or overscan areas or through analysis of separate bias frames. In a weakly-illuminated

EMCCD image there are bias level pixels across the whole image since only a small fraction of pixels actually receive a photon. These bias pixels can be identified using a histogram, the peak of which corresponds to the bias level of the camera. The tungsten flat fields were also not used in the analysis. The reason for this was that, in error, only 5 were taken. This was insufficient to allow removal of pixel-to-pixel sensitivity variations and would in fact have only added noise to the data. It would have been better to have taken several hundred flat field frames on the night of the observation.

All of the extraction, bias and sky subtraction, header manipulation and binning in the spatial direction was performed using custom procedures written in IDL. The decision to bin the data off-chip allowed greater flexibility in the analysis. With a conventional CCD this would add a noise penalty since it would effectively increase the read-noise. In the case of an EMCCD where the read-noise is negligible there is no difference between binning on or off-chip.

The spectra were then loaded into the **MOLLY** package for further analysis. This package, written by Tom Marsh, is widely used for the analysis of large stacks of sequential spectra and was invaluable in the subsequent data analysis phase. Once loaded into **MOLLY**, the next stage was to identify the calibration arc lines using an arc map. About five lines were identified, selected so as to cover evenly and fully the image in the spectral direction. Each block of arc spectra had its arc lines identified. The pixel positions of these lines were then plotted as a function of time (obtained automatically from the image headers) using **MOLLY** and a two-term polynomial function fitted to the points. This polynomial interpolation then allowed wavelength calibration of any intermediate science frame by reading off the time stamp in its header and inserting it into the polynomial. The RMS scatter of the fits to the arc lines was typically 0.03\AA (corresponding to 1.4km s^{-1} at $\text{H}\alpha$). For this to work it was necessary to assume that the instrument flexure was smoothly varying with no sudden jumps. The wavelength calibration meant that the pixel positions of features in the spectra could be expressed with equal convenience in units of wavelength or velocity (about a given centre wavelength).

7.2.1 The average spectrum

Figure 7.4 shows the average of all of the 628 spectra that we obtained of SDSS J1433. The most prominent feature is the $\text{H}\alpha$ line, with a weaker feature due to $\text{He I } \lambda 6678$ also visible. The line parameters shown in Table 7.2 were measured from this figure. The average spectrum is typical of other eclipsing CVs below the period gap, e.g. WZ Sge (Skidmore et al., 2000).

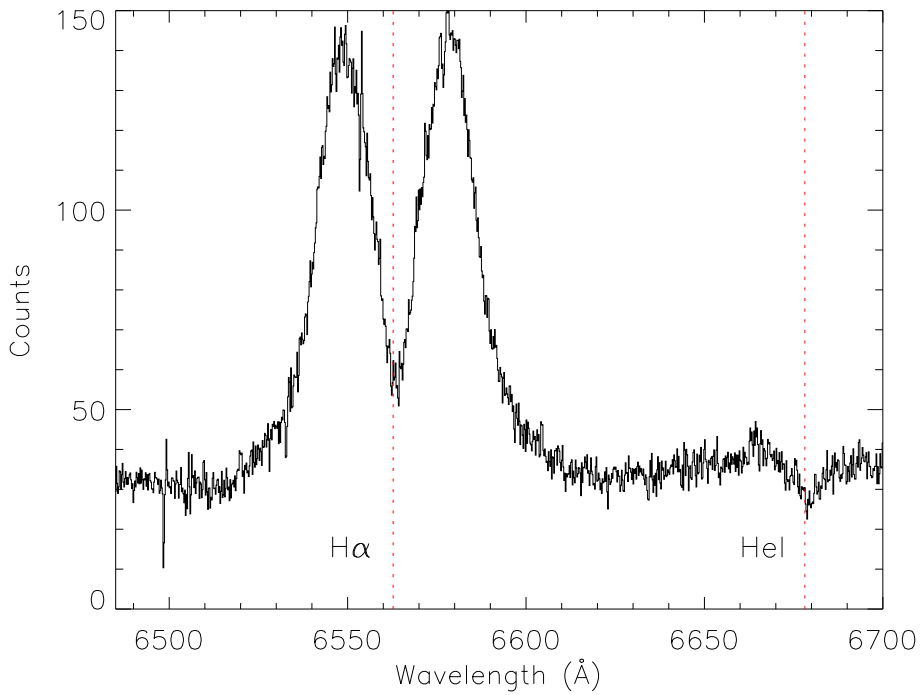


Figure 7.4: The average spectrum obtained by combining all 628 spectra taken during our observing run.

7.2.2 Continuum and H α light curves

We computed the light curve of the continuum by summing the flux in line-free portions of each spectrum. We then fitted and subtracted the continuum of each spectrum, and summed the residual flux in the H α emission line. The resulting light curves are shown in Figure 7.5.

Figure 7.5 shows that H α experiences broader eclipses than the continuum. The eclipse depth for H α is $\sim 50\%$, while for the continuum it is $\sim 75\%$. This is consistent with H α being emitted in the optically thin outer parts of the accretion disc and the hotter, optically thick, inner parts of the disc being responsible for the majority of the continuum emission. An orbital hump prior to eclipse is also apparent in the H α light curve, caused by the changing aspect of emission from the bright spot.

7.2.3 Trailed spectra and Doppler tomogram

The phase-binned, continuum-subtracted H α profile is shown as a trail in the lower panel of Figure 7.6. The primary eclipse around phase 0 is clearly seen, as is the rotational disturbance where the blue peak of the emission line is eclipsed prior to the red peak. The bright spot is clearly visible as an S-wave moving between the two peaks. The orbital modulation of the wings of the emission line can arguably

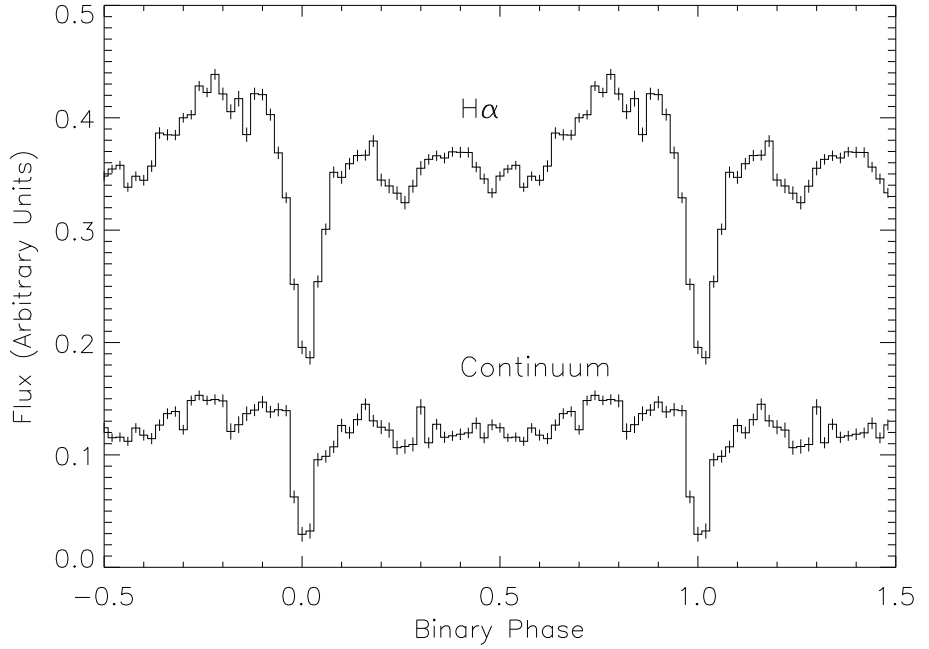


Figure 7.5: The light curves for the continuum and the H α emission line.

just be made out. There is also evidence for a ‘shadow’ on the blue edge of the S-wave around phase 0.25 which appears remarkably similar to the models of gas stream overflow computed by Hellier & Robinson (1994).

We computed the Doppler tomogram of the H α trail using Fourier-filtered back projection (see Marsh (2001) for a review). As expected, the dominant feature is the ring of emission representing the accretion disc which appears to be centred on the expected position of the WD. The bright spot lies on this ring at a velocity intermediate between the free-fall velocity of the gas stream and the Keplerian disc velocity along its path, as observed in some other CVs, e.g. U Gem (Marsh et al., 1990) and WZ Sge (Spruit & Rutten, 1998). There is no evidence for emission from the secondary star, nor for asymmetries in the disc emission due to, for example, spiral shocks.

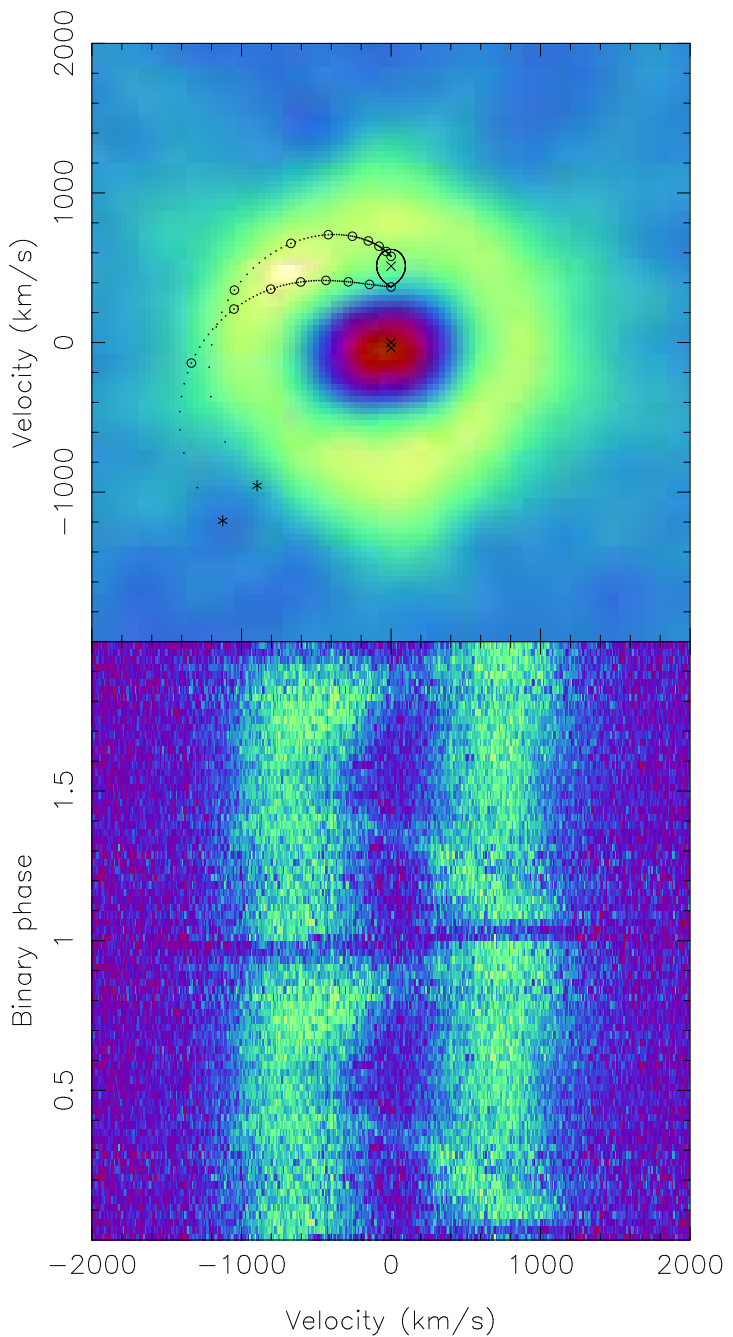


Figure 7.6: *Bottom:* the H α trailed spectrum, with two cycles plotted for clarity. *Top:* the Doppler map of H α . The three crosses represent the centre of mass of the secondary star (upper cross), the system (middle cross) and the WD (lower cross). The Roche lobe of the secondary star, the predicted gas stream trajectory and the Keplerian velocity of the disc along the stream are also shown, calculated assuming the system parameters given in Littlefair et al. (2008). The circular tick marks represent steps of 0.1 L₁ towards the WD. The asterisks represent the points of closest approach to the WD.

7.2.4 The diagnostic diagram

The WD primary star orbits with velocity K_W around the centre of mass of the system, resulting in Doppler shifting of the light it emits. If we imagine the simplified case of an ideal accretion disc centred on the WD with a perfectly axi-symmetric brightness distribution, then the velocity shift of the emission lines from the disc will be subject to the same modulation as the WD. If we measure the emission-line centroids and plot them as a function of orbital phase we should see a sine wave corresponding to the orbital motion of the WD. More realistically, however, if we include the light emitted by the bright spot, we can see that calculated line centroids will, rather than precisely following the WD, be perturbed in the direction of the bright spot. The resulting radial velocity (RV) curve will not only have an excessive amplitude but will also be offset in phase with respect to the true motion of the WD. It is thus important to exclude the bright spot contribution by only examining the light emitted in the wings of the line profile. These emissions correspond to material orbiting within the disc at small radii from the primary star, where they are only minimally contaminated by the bright spot at the outer edge of the disc. If the RV curve that we obtain using this technique has the correct phase offset relative to the primary eclipse then we can be confident of an accurate semi-amplitude measurement.

To measure the radial velocities of the wings of the H α emission line we used the double-Gaussian technique of Schneider & Young (1980). The best signal-to-noise ratio was obtained using a Gaussian width of 350 km s $^{-1}$ and the separation of the Gaussians was then varied between 1500 and 3000 km s $^{-1}$ in steps of 100 km s $^{-1}$ so as to explore annular regions of the accretion disc of decreasing radii. At each Gaussian separation the resulting radial velocities were fitted with a sine function. The phase offset (ϕ_0), semi-amplitude (K), systemic velocity (γ) and fractional error in the amplitude (σ_K/K) of the sine fits were then plotted against the Gaussian separation as a diagnostic diagram (Shafter et al., 1986), as shown in Figure 7.7. An example of the RV data and sine fit is shown in Figure 7.9, for a Gaussian separation of 2900 km s $^{-1}$.

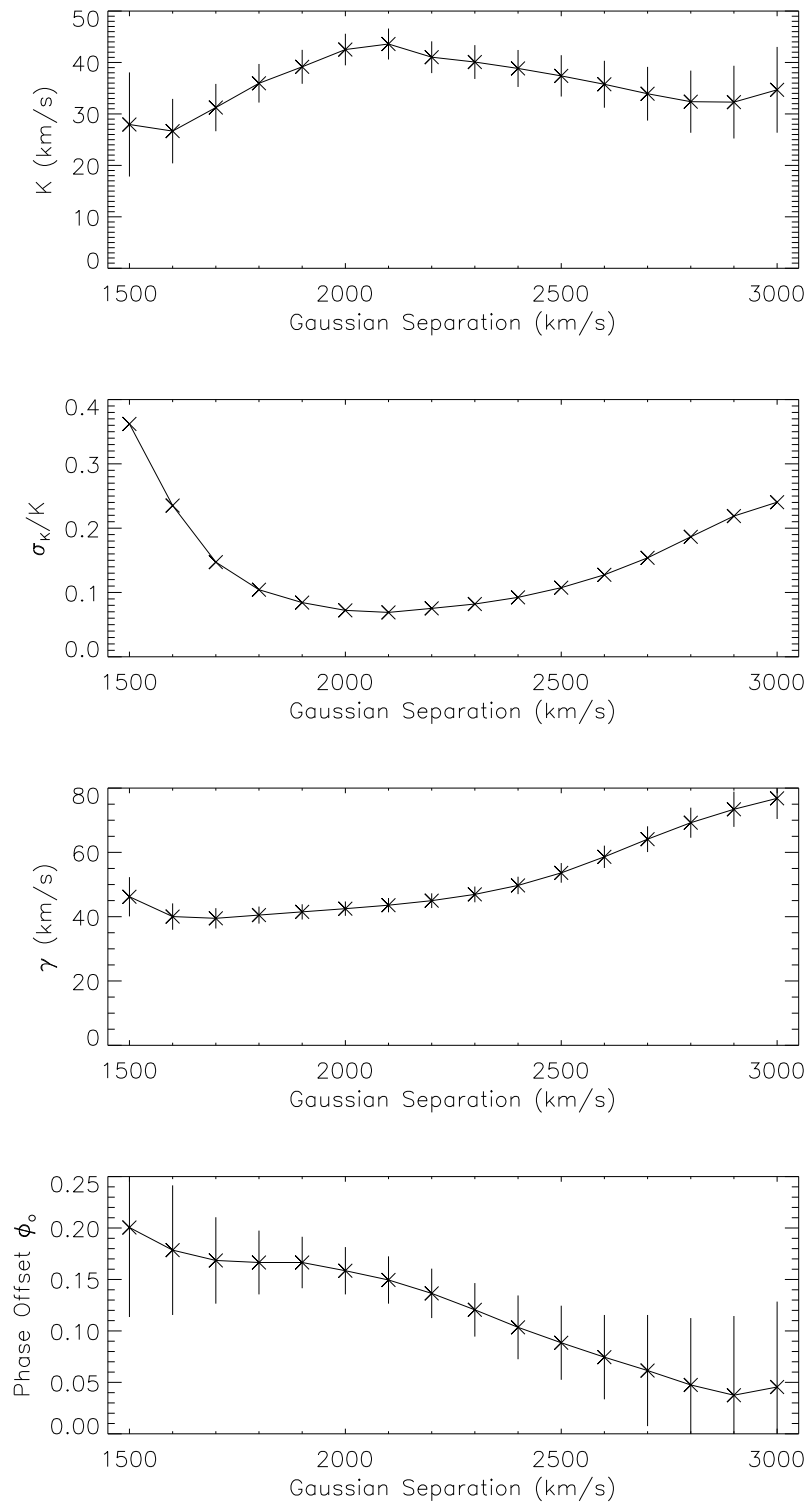


Figure 7.7: The diagnostic diagram for H α – see text for details.

The standard way of obtaining K_W from a diagnostic diagram is to use the value corresponding to where the σ_K/K curve is at a minimum. If we do this we find a value of $K_W = 44 \text{ km s}^{-1}$. However, it can be seen that the corresponding value of ϕ_0 is non-zero and declines towards zero at higher Gaussian separations. As pointed out by Marsh (1988), this highlights the main drawback of diagnostic diagrams – the derived K_W -value is noise dependent. The best solution is to use those data points corresponding to the highest Gaussian separations to extrapolate to a K_W -value whose corresponding $\phi_0 = 0$. This requires the construction of a ‘Light Centre’ diagram (Marsh, 1988).

7.2.5 The light centre method

At no point on the diagnostic diagram does the sine fit have a zero phase offset relative to the WD, although at the extremes of the H α wings it gets close. The light centre method, described by Marsh (1988), offers a way of extrapolating the data to estimate what the amplitude of the RV curve would be at $\phi_0 = 0$. Just as the Doppler map is a view of an emission line transformed into the velocity space of the CV, so the light centre diagram is a velocity space projection of the data plotted in the diagnostic diagram. Each position along the velocity axis of the diagnostic diagram shows the measured system parameters K_W , γ and ϕ_0 calculated on the basis of signal contained in a ring on the Doppler map with diameter equal to that velocity. If we then combine the K_W and ϕ_0 results, as shown in equations 7.1 and 7.2 , then the centres of these annuli (of varying velocity diameters) can be plotted on the Doppler map.

$$K_X = -K \sin \phi_0 \quad (7.1)$$

$$K_Y = -K \cos \phi_0 \quad (7.2)$$

The light centre diagram for SDSS J1433 is shown in Figure 7.8. Its axes are labeled, just as they are on the Doppler map, with velocities parallel-to (K_Y) and perpendicular-to (K_X) the line joining the two stars; however, the scales are very different so the light-centre diagram is really a zoomed-in view of the Doppler map in the region of the two crosses marking WD centre and system barycentre (see Figure 7.6). As the annuli increase in diameter the light centre tends to converge to the point at which $K_X=0$, $\phi=0$ and $K_W=K_Y$. No actual data point is plotted at $K_X=0$ since there simply was not enough signal present in the high velocity wings of the emission line. Instead, the last few data points are used to extrapolate a line that intersects the y -axis. The intercept point, which was found to be $34 \pm 4 \text{ km s}^{-1}$, was then taken as being equal to K_W . The error was estimated by examining a range of fits to the data excluding various data points at the extremes. It was found that the range of K_W values given by these varying fits was entirely consistent with the

formal error of the original fit that used all of data points bounded by a red box in Figure 7.8. The data points in the upper left-hand part of the plot are clearly pulled in the direction of the bright spot and have been excluded from the calculations.

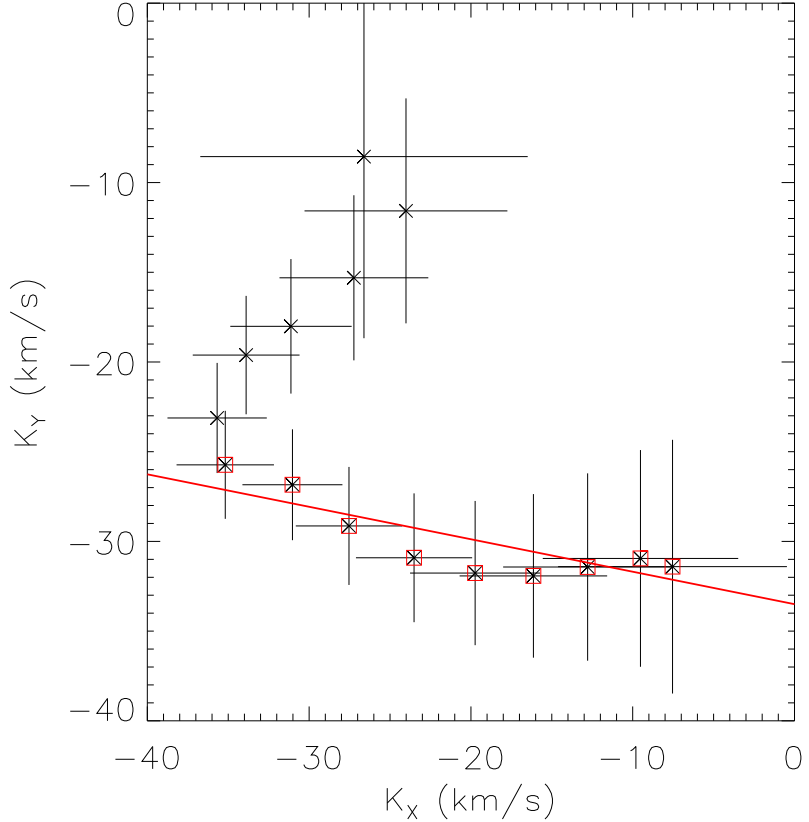


Figure 7.8: The light centre diagram for $\text{H}\alpha$, where $-K \sin \phi_0$ is plotted on the abscissa and $-K \cos \phi_0$ on the ordinate. A linear fit to the points marked by red squares is also shown, extrapolated to where it intercepts the y -axis. The smallest Gaussian separation corresponds to the top-most point and the largest to the right-most point.

The solution for K_W was then compared with one of the RV curves used to prepare the diagnostic diagram (Section 7.2.4). This is shown in Figure 7.9. Here the data points were measured using a Gaussian separation of 2900 km s^{-1} and the solid red line is a least square sine fit to that data. Also plotted is a dashed red line corresponding to the light centre solution.

7.2.6 Eclipse phase as a function of accretion disc radial velocity

Figure 7.10 shows how the phase of the eclipse minimum of the emission lines changes with the velocity of material within the accretion disc. The rotational disturbance

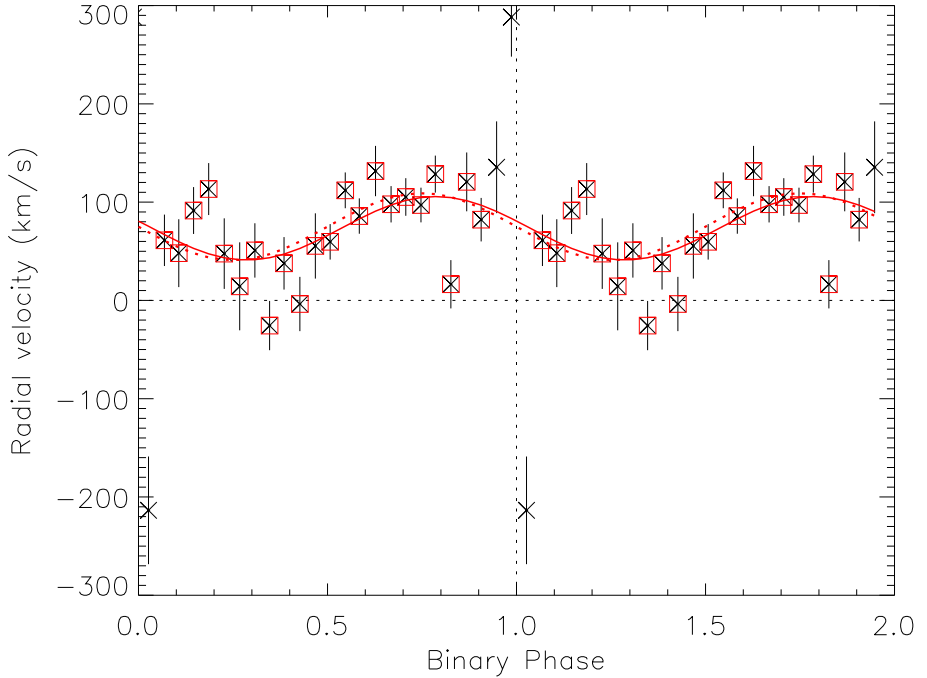


Figure 7.9: The measured RV data for a Gaussian separation of 2900 km s^{-1} and the resulting sine curve fit (solid line). Only data points marked by a square were included in the fit, i.e. the rotational disturbance around phase 0 was not taken into account. The dashed line shows the sine curve corresponding to the motion of the WD as derived from the light centre diagram.

around the primary eclipse is clearly visible. Young & Schneider (1980) used a similar graph to deduce the mass ratio of DQ Herculis. Their method was briefly investigated here but did not produce a sensible answer due to uncertainties about the disc structure parameter, a parameter describing the brightness distribution of the accretion disc.

7.3 Conclusions drawn from observations

The radial velocity amplitude K_W was measured using the light centre technique to be $34 \pm 4 \text{ km s}^{-1}$. The measured value of K_W is consistent with the predicted value of $K_W = 35 \pm 2 \text{ km s}^{-1}$ from the light-curve fitting technique of Littlefair et al. (2008). This result therefore confirms the validity and accuracy of the purely photometric technique of measuring masses; the presence of a brown-dwarf donor in SDSSJ1433, and by implication in SDSSJ1507, is thus dynamically confirmed. This result also demonstrates that the combination of a large-aperture telescope, an intermediate-resolution spectrograph and an EMCCD is uniquely capable of tackling this type of photon-starved observation.

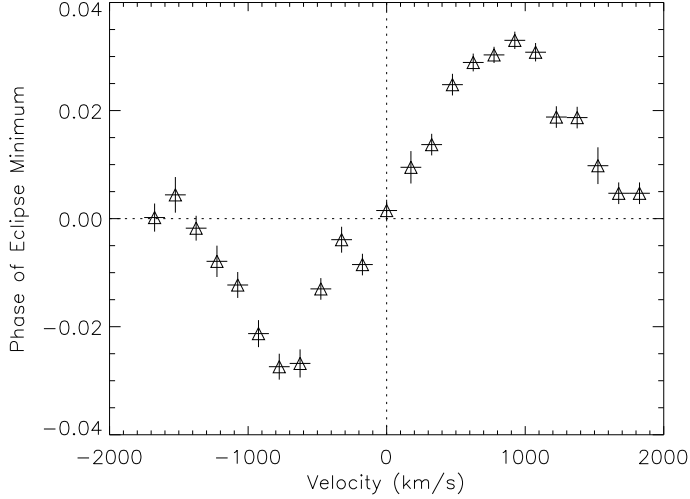


Figure 7.10: The phase of eclipse minimum as a function of velocity in the H α emission line.

Table 7.2: Full-width at zero intensity (FWZI), full-width at half maximum (FWHM), peak-to-peak separation and equivalent width of the H α emission line shown in Figure 7.4. The radial velocity semi-amplitude of the WD and the systemic velocity derived in Sections 7.2.4 and 7.2.5 are also listed.

FWZI	$5000 \pm 500 \text{ km s}^{-1}$
FWHM	$2200 \pm 200 \text{ km s}^{-1}$
Peak separation	$1300 \pm 200 \text{ km s}^{-1}$
Equivalent width	$147.2 \pm 0.5 \text{ \AA}$
K_W	$34 \pm 4 \text{ km s}^{-1}$
γ	$75 \pm 10 \text{ km s}^{-1}$

7.4 The SNR advantage gained by use of an EM-CCD

To give an idea of how these observations would have appeared had they been done using a conventional CCD, the raw spectra were degraded by adding read-noise artificially. One such spectrum is shown in Figure 7.11. The graphs show two 30s exposures that have been bias and sky subtracted. The right-hand graph is a genuine QUCAM2 spectrum in which the H α line centred on wavelength element 400 can clearly be seen. To extract this spectrum from the data frame required a window with a height of 10 pixels to be placed around the spectrum. These 10 rows were then binned in the spatial direction so as to include all of the signal into a 1D spectrum. The left-hand plot shows the same spectrum as it would have appeared using a conventional CCD with a read-noise of $3e^-$. Since the spectra required a

spatial binning factor of $\times 10$ it is assumed that some on-chip binning would have been performed with the conventional CCD. An observer anxious to maximise the SNR from a conventional CCD for these observations would probably have used an on-chip binning factor of $\times 3$. This would then leave a further factor of $\times 3$ to be performed off-chip so as to get all the flux into the 1D spectrum. The off-chip binning increases the read-noise from $3e^-$ to $\sqrt{3} \times 3 = 5.2e^-$ and it is this noise level that is added to the data to produce the left-hand plot. As pointed out in Chapter 5, the ability of EMCCDs to be noiselessly binned off-chip increases further their advantage over conventional CCDs. The improvement gained from the use of the EMCCD is very striking. The observation would clearly have been impossible with a conventional CCD. The exact SNR gain is not easy to quantify; depending not only on the conventional CCD's read-noise and binning factor but also on the time resolution required in the observations.

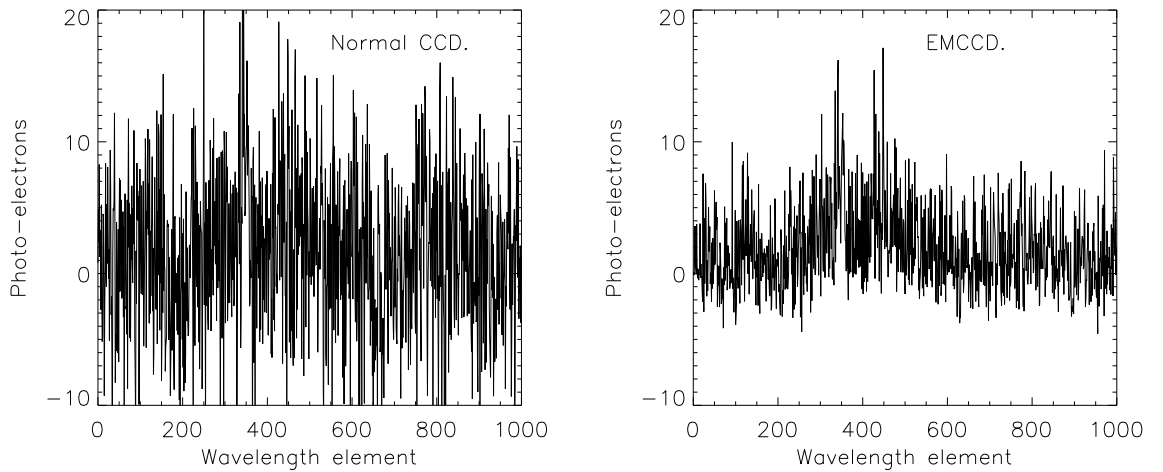


Figure 7.11: A single spectrum recorded with the EMCCD on the right and a simulated normal CCD with $3e^-$ read-noise on the left. The on-chip binning factor used with the normal CCD was $\times 3$. See text for details.

Chapter 8

Conclusions and future work

Chapters 2 and 3 have described the mechanical, electronic and software design of the QUCAM2 EMCCD. Subsequent use of the camera for astronomical observations have showed that the design was successful.

Horizontal charge transfer efficiency at the $100e^-$ and $250e^-$ level was found to be equally good through both the normal and the EM outputs (see Section 3.4.2). At the single electron level, however, the horizontal CTE through the EM register was found to be very poor (Section 5.1.1) producing a deferred charge of 9%.

The effectiveness of dither (Section 3.5.6) in the reduction of surface dark current was demonstrated, with the result that it allows the CCD to be used in non-inverted mode with an accompanying drop in parallel-area CIC. One important implication of this is that a Peltier cooled CCD operating at elevated temperatures may still permit non-inverted operation. In the Peltier regime high dark current and low parallel area CIC need not therefore be mutually exclusive.

In Chapters 4 and 5 techniques were described that allowed the noise generated in the image area, serial register and the EM register to be measured separately. Parallel-area CIC was minimised by using non-inverted operation. Serial-register CIC was minimised by a reduction in the serial-clock voltage swings. The limiting detector noise source has been identified as the EM-register CIC. The EM-register CIC could not, however, be reduced since any changes to the clock voltages would inevitably have changed the multiplication gain.

It has been demonstrated that high gain is necessary for both linear-mode operation and also photon-counting operation. In the former the higher multiplication gain can reduce the significance of the in-EM-register generated CIC (see Section 4.1.5). In the latter a high gain in combination with a low read-noise is essential to allow the use of a photon-counting threshold low enough to capture a large fraction of the photoelectron events (see Section 5.2.3).

In order to get maximum performance in photon-counting mode it is necessary to tune the exact threshold so as to include the maximum number of photoelectrons whilst rejecting the majority of the in-EM-register CIC events. By using a slightly elevated threshold, for example $0.1e^-$, we can detect $\sim 90\%$ of photoelectrons whilst rejecting $\sim 75\%$ (see Figures 5.10 and 5.11) of the in-EM-register CIC electrons. CIC is a bigger problem when photon counting than when operating in linear mode due to the ‘ K factor’ (see Equation 5.10). A CIC event generated midway along the EM register will only contribute a small fraction of the charge of a genuine photoelectron since it will not receive the full multiplication. It may still, however, be large enough to lie above the photon-counting threshold and be counted as a full electron. Its significance in photon-counting mode is therefore considerably greater than in linear mode. Using an optimum photon counting threshold can reject most of this CIC. Even so, in photon-counting mode we see more CIC than in linear mode and this restricts the lower end of the dynamic range.

It was shown that for photon counting to be effective the CIC charge in electrons per pixel should be below $0.003e^-$ and the EM gain should be high enough to push the effective read-noise below $0.025e^-$. Photon counting can then give a 10–20 % advantage across a narrow operational range where the signal per frame is below about $0.6e^-$ per pixel (see Figure 5.12). Above this signal level we encounter coincidence losses and it is then preferable to use the EMCCD in linear mode. As the signal increases further multiplication noise (Section 1.3.5) starts to become significant and above $\sim 9e^-$ per pixel it then becomes preferable to switch to the normal output. At higher signal levels photon-counting mode can still be used by operating the camera at higher frame rates than required for the desired temporal resolution and then binning together (or ‘blocking’) many photon-counted frames. This keeps the signal level in each frame low enough to avoid coincidence losses. The models described in Section 5.2.12 show that operating in this way does not degrade the maximum SNR advantage that can be obtained but merely moves the zone of optimum operation to higher (per temporal bin) signal levels.

There are two main factors that limit the astronomical applications of EMCCDs. Probably the most important is the current lack of large format devices. The CCD201, with its 13mm x 13mm imaging area is the largest off-the-shelf frame-transfer EMCCD available. This was not a big limitation for the astronomical observations described in Chapter 7 where only a single spectral line was observed. Additionally we were lucky enough to locate a suitable reference star close by our target object. The ISIS spectrograph, however, is normally used with 2k x 4k detectors measuring 30mm x 60mm and any future EMCCDs will need to be of this size for them to be considered as standard ISIS detectors. They will actually need to measure 4k x 4k pixels if we include the extra area required to implement the frame store: EMCCDs can only be fully exploited if they are of frame-transfer design.

Such a large detector will need to have multiple outputs if high frame rates are to be achievable. For example, if an EMCCD can be read out at 10Mpixel s^{-1} through a single port then a $2\text{k} \times 4\text{k}$ device can only be read out at $\sim 1\text{ frame s}^{-1}$. This is probably rather slow if photon-counting is to be exploited. The MOSFET amplifier at the output of the CCD201 is capable of between 13 and 20Mpixel s^{-1} according to the E2V data sheet. Assuming that this is a typical value for current EMCCD output amplifiers then to achieve frame rates of, say, 10Hz would probably require the manufacturers to develop new higher-speed amplifiers. As well as being expensive this will inevitably come with a noise penalty and it has been shown in Section 5.2.3 that read-noise cannot be ignored when operating an EMCCD. It would therefore make sense for any future large-format EMCCD to instead have multiple outputs to allow parallel processing of the pixels. Multiple outputs will in fact be essential if the user is to be given the option of using the EMCCD in conventional mode. Using conventional mode requires much lower pixel rates (in the region of 200kpix s^{-1}) if $2\text{--}3\text{e}^-$ of read-noise is to be achieved and if only a single output is available then readout times of many tens of seconds can be expected. One can envisage an EMCCD design where the horizontal register is segmented, with each segment containing both a conventional and an EM output amplifier.

The second limitation to the performance of EMCCDs is the presence of CIC. This is already very low in the cameras investigated. Making it lower still could expand considerably the range of illuminations over which an EMCCD can be operated in photon-counting mode. Since the CIC appears mainly in the EM register it would seem probable that a decrease in the required HV clock amplitudes could help in reducing this noise component.

The effectiveness of EMCCDs for high-time resolution, high-resolution spectroscopy has been demonstrated. In Chapter 7, a comparison was shown between an actual observation of a cataclysmic variable and a simulated observation of the same object using a conventional CCD. This comparison showed that the observation would only have otherwise been possible on a much larger telescope. For example, Ives et al. (2008) estimate that the performance gain when using an EMCCD, for what would previously have been a detector-noise limited observation, is equivalent to a factor of 1.7 in telescope aperture.

Recent developments in scientific grade CMOS (sCMOS) imaging devices from Andor, PCO and Fairchild could present serious competition to EMCCDs in certain imaging applications. These devices implement CDS video processing circuitry within every pixel of the detector. This not only allows very rapid gating of the sensitivity of the device, thus eliminating the need for a separate light-shielded frame store, but also allows very-low noise performance at very-high frame rates.

The manufacturers quote $< 2\text{e}^-$ at 30 frames per second from a 5.5Mpixel device¹. Unfortunately the extra circuitry reduces the fill-factor of the light sensitive regions of the pixels. This is partially compensated for by the use of microlenses that concentrate the light within the light-sensitive part of each pixel. These preclude, however, the use of an AR coating (which requires a plane surface for optimum performance) and the mean QE between 400nm and $1\mu\text{m}$ is only $\sim 35\%$ compared with $\sim 70\%$ for the CCD201. This large loss of QE means that the current sCMOS device can never outperform the SNR achievable with the CCD201 at any signal level or operational mode. However, future backside-illuminated designs with larger fill factors will almost inevitably be developed and so could offer some competition in high frame-rate photon-noise limited observations. For extremely faint imaging the non-negligible read noise of sCMOS means that an EMCCD will remain superior.

¹<http://www.scmos.com/>

Bibliography

- Basden A. G., Haniff C. A., Mackay C. D., 2003, MNRAS, 345, 985
- Boksenberg A., Burgess D. E., 1972, in Photo-Electronic Image Devices An image photon counting system for optical astronomy.. pp 835–849
- Boyle W., Smith G., 1970, Bell Syst. Technical Journal 49, Charge Coupled Devices. Bell Labs
- Burke B. E., Gajar S. A., 1991, IEEE Transactions on Electron Devices, 38, 285
- Daigle O., Gach J.-L., Guillaume C., Lessard S., Carignan C., Blais-Ouellette S., 2008, in SPIE Vol. 7014 of Conference Series, CCCP: a CCD controller for counting photons
- Dhillon V. S., Marsh T. R., Jones D. H. P., 1991, MNRAS, 252, 342
- Dhillon V. S., Marsh T. R., Stevenson M. J., Atkinson D. C., Kerry P., Peacocke P. T., Vick A. J. A., Beard S. M., Ives D. J., Lunney D. W., McLay S. A., Tierney C. J., Kelly J., Littlefair S. P., Nicholson R., Pashley R., Harlaftis E. T., O'Brien K., 2007, MNRAS, 378, 825
- Downing M., Finger G., Baade D., Hubin N., Iwert O., Kolb J., 2008, in SPIE Vol. 7015 of Conference Series, Detectors for AO wavefront sensing
- Hellier C., 2001, Cataclysmic Variable Stars. Springer, 2001
- Hellier C., Robinson E. L., 1994, ApJ, 431, L107
- Hynecek J., 2001, IEEE Transactions on Electron Devices, 48, 2238
- Ives D., 2007, Master's thesis, University of Bolton
- Ives D., Bezawada N., Dhillon V., Marsh T., 2008, in SPIE Vol. 7021 of Conference Series, ULTRASPEC: an electron multiplication CCD camera for very low light level high speed astronomical spectrometry
- Janesick J. R., 2001, Scientific Charge-Coupled Devices. SPIE Press, PO Box 10, Bellingham, WA

- Jenkins C. R., 1987, MNRAS, 226, 341
- Jerram P., Pool P. J., Bell R., Burt D. J., Bowring S., Spencer S., Hazelwood M., Moody I., Catlett N., Heyes P. S., 2001, in Blouke M. M., Canosa J., Sampat N., eds, SPIE Vol. 4306 of Conference Series, The LLCCD: low-light imaging without the need for an intensifier. pp 178–186
- Jorden P. R., Pool P., Tulloch S. M., 2004, in Amico P., Beletic J. W., Beletic J. E., eds, Scientific Detectors for Astronomy, The Beginning of a New Era Vol. 300 of Astrophysics and Space Science Library, Secrets of E2V Technologies CCDs. pp 115–122
- Law N. M., Mackay C. D., Baldwin J. E., 2006, AAP, 446, 739
- Littlefair S. P., Dhillon V. S., Marsh T. R., Gänsicke B. T., Southworth J., Baraffe I., Watson C. A., Copperwheat C., 2008, MNRAS, 388, 1582
- Littlefair S. P., Dhillon V. S., Marsh T. R., Gänsicke B. T., Baraffe I., Watson C. A., 2007, MNRAS, 381, 827
- Littlefair S. P., Dhillon V. S., Marsh T. R., Gänsicke B. T., Southworth J., Watson C. A., 2006, Science, 314, 1578
- Marsh T. R., 1988, MNRAS, 231, 1117
- Marsh T. R., 2001, in Boffin H. M. J., Steeghs D., Cuypers J., eds, Astrotomography, Indirect Imaging Methods in Observational Astronomy Vol. 573 of Lecture Notes in Physics, Berlin Springer Verlag, Doppler Tomography. pp 1–+
- Marsh T. R., 2008, in Phelan D., Ryan O., Shearer A., eds, Astrophysics and Space Science Library Vol. 351 of ASSL, High-Speed Optical Spectroscopy. pp 75–+
- Marsh T. R., Horne K., Schlegel E. M., Honeycutt R. K., Kaitchuck R. H., 1990, ApJ, 364, 637
- Nelemans G., Steeghs D., Groot P. J., 2001, MNRAS, 326, 621
- Paczyński B., 1967, Acta Astronomica, 17, 287
- Pakmor R., Kromer M., Röpke F. K., Sim S. A., Ruiter A. J., 2010, Nature, 463, 61
- Pringle J. E., 1981, ARAA, 19, 137
- Rappaport S., Joss P. C., Webbink R. F., 1982, ApJ, 254, 616
- Ritter H., Kolb U., 1998, AAPS, 129, 83

- Rixon G. T., Walton N. A., Armstrong D. B., Woodhouse G., Tulloch S. M., 2000, in Lewis H., ed., SPIE Vol. 4009 of Conference Series, UltraDAS: the high-performance data acquisition system at the Isaac Newton Group of Telescopes. pp 132–140
- Robbins M. S., Hadwen B. J., 2003, IEEE Transactions on Electron Devices, 50, 1227
- Robinson E. L., Barker E. S., Cochran A. L., Cochran W. D., Nather R. E., 1981, ApJ, 251, 611
- Schatzman E., 1962, Annales d'Astrophysique, 25, 18
- Schneider D. P., Young P., 1980, ApJ, 238, 946
- Shafter A. W., Szkody P., Thorstensen J. R., 1986, ApJ, 308, 765
- Skidmore W., Mason E., Howell S. B., Ciardi D. R., Littlefair S., Dhillon V. S., 2000, MNRAS, 318, 429
- Spruit H. C., Rutten R. G. M., 1998, MNRAS, 299, 768
- Szkody P., Henden A., Mannikko L., Mukadam A., Schmidt G. D., Bochanski J. J., Agüeros M., Anderson S. F., Silvestri N. M., Dahab W. E., Oguri M., Schneider D. P., Shin M.-S., Strauss M. A., Knapp G. R., West A. A., 2007, AJ, 134, 185
- Tubbs R., 2003, PhD thesis, University of Cambridge
- Tulloch S., 2006, in Beletic J. E., Beletic J. W., Amico P., eds, Scientific Detectors for Astronomy 2005 L3 CCD Wavefront Sensor Developments at the ING. pp 303–+
- Tulloch S. M., 2004, in Moorwood A. F. M., Iye M., eds, SPIE Vol. 5492 of Conference Series, Photon counting and fast photometry with L3 CCDs. pp 604–614
- Tulloch S. M., Rodriguez-Gil P., Dhillon V. S., 2009, MNRAS, 397, L82
- Verbunt F., Zwaan C., 1981, AAP, 100, L7
- Warner B., 1995, Cataclysmic Variable Stars. Cambridge University Press, Cambridge
- Young P., Schneider D. P., 1980, ApJ, 238, 955
- Zacharias N., Dorland B., Bredthauer R., Boggs K., Bredthauer G., Lesser M., 2007, in Society of Photo-Optical Instrumentation Engineers (SPIE) Conference Series Vol. 6690 of Society of Photo-Optical Instrumentation Engineers (SPIE) Conference Series, Realization and application of a 111 million pixel backside-illuminated detector and camera

Appendices

A. Listing of the simple model

```
FUNCTION Multiply,input_image,gain
; EM multiply a 2D image. Gain is the overall gain of EM register
; Assumes a 520 pixel gain stage
COMMON seeds,seed ; Global variable to store the random seed
IF (gain EQ 1) THEN RETURN,input_image
stages=520.0
gainPerStage=10^(ALOG10(gain)/stages)
packetSize=OUL ; The size of the pixel charge packet
sz=SIZE(input_image)
output_image=LONARR(sz[1],sz[2])
number_pixels=sz[1]*sz[2]
-----
FOR pix_count=0UL,number_pixels-1 DO BEGIN
; Loop through all the pixels in the image
packetSize=input_image[pix_count]
IF (packetSize NE 0) THEN BEGIN
FOR stage=1,stages DO BEGIN
; Run each pixel through the EM register
dice=RANDOMU(seed,packetSize)+1
; The "dice" variable is a vector of random numbers
; one random number for eaach electron in the pixel
; charge packet
success=WHERE((dice LE gainPerStage),count)
; The "count" variable is the number of the random numbers
; in "dice" that lie below the "gainperstage" i.e.
; the number of multiplication events that have occurred
; in the current EM stage.
packetSize=packetSize+count
ENDFOR
ENDIF
output_image[pix_count]=packetSize
ENDFOR
RETURN,output_image
END
```

B. Listing of the advanced model

```
FUNCTION SimulateCCD201final,InpImage,EMCIC,serialCIC,parallelCIC,Dark,$
Gain,RNoise,VIDsense,CTE_EM,CTE_N,S,DGP=dgp
;-----
; IDL Simulation of the CCD201
; SMT Jan 2009
;-----
;Input parameters:
;
;InpImage      Integer array containing photoelectrons, amplifier
;               at bottom left. This must correspond in width
;               to the physical image area of a CCD201
;               i.e. 1056 pixels. The height is a free parameter
;serialCIC     Serial cic, total contribution per pixel to image.
;EMCIC         EM-origin CIC, total contribution per pixel to image.
;parallelCIC   Parallel cic, total contribution per pixel to image.
;Dark          Dark current in image area. e per pixel.
;Gain          EM multiplication gain.
;RNoise        Read noise in ADU.
;VIDsense     Video processor sensitivity.
;CTE_EM        Probability of transfer per stage of EM register.
;CTE_N         Probability of transfer per stage of serial register.
;S             Seed for random number generation.
;/DGP          Optional keyword, if set then clears serial register
;               adjacent to store area after each line transfer.
;-----
; Returns : outputimage
; A long integer array corresponding to the output image in ADU.
; This image measures 1072 x (y-extent of input image).
; The first row will be empty of photo-charge due to the EM pipeline.
; First 16 columns will be serial underscan. No serial overscan.
;-----
; CAUTION : Takes about 7s per bias image row.
;-----
; Size of pipeline components--
length_node=1      ; output node
length_uscan=16    ; 16 stages closest to amp, no gain
length_EM=604      ; Amplification register
length_connect=468 ; Segment from image to amplification register
length_image=1056  ; Actual width of physical image columns
length_oscans=16   ; Serial overscan
lengthTotal=length_node+length_uscan+length_EM+length_connect+$
length_image+length_oscans
EMGain=Gain
scic_probability_per_transfer=serialCIC/$
(1.0D*(length_image+length_uscan+length_connect))
probability_of_gain_per_EM_stage=EXP(ALOG(EMgain*1.0D)/length_EM)-1
; The probability of CIC being generated per stage is actually
; =EMCIC*probability_of_gain_per_EM_stage/(1-1/Gain)
; Here an approximation is used.
```

```

EMcic_probability_per_transfer=EMCIC*probability_of_gain_per_EM_stage
pcic=parallelCIC
inputimage=LONG(REVERSE(InpImage))
seed=S
hcte_per_EM_stage=CTE_EM
hcte_per_NORM_stage=CTE_N
noise=RNoise
; Check parameters
sz=SIZE(inputImage)
IF (sz[1] NE 1056) THEN BEGIN
    PRINT,"Input Image of wrong width (must be 1056 pixels)"
    RETURN,0
ENDIF
; Add parallel CIC and dark current
IF (pcic NE 0.0) THEN inputImage+=$
RANDOMN(seed,sz[1],sz[2],POISSON=(pcic),/DOUBLE)
IF (Dark NE 0.0) THEN inputImage+=$
RANDOMN(seed,sz[1],sz[2],POISSON=(Dark),/DOUBLE)
imageY=sz[2]
imageX=1072
; height of output image same ----
outputimage=LONARR(imageX,imageY)
;-----
; Two pipeline arrays. First copied to second 1 pixel to left.
; During copy the effects of finite CTE and EM gain are considered
Pipeline=LONARR(lengthTotal)
PipelineTemp=Pipeline
true=1
false=0
deferred=0L
;-----
FOR y=0,imageY-1 DO BEGIN
PRINT,Y
; Do vertical transfer, ADDING (not replacing) row of image to what is
; already in serial register
Pipeline[length_oscans:length_image+length_oscans-1]+=inputImage[*,y]
; Optional dump gate clear of serial register.
IF keyword_set(DGP) THEN $
Pipeline[length_oscans:length_image+length_oscans-1]=0
FOR x=0,imageX-1 DO BEGIN
; Read out Serial register
;-----
FOR p=lengthTotal-1,1,-1 DO BEGIN
; Run along pipeline updating each element in turn.
; Updated values->temp array.
inEM=false
IF ((p GE length_connect+length_image+length_oscans) $
AND (p LT length_EM+length_connect+length_image+length_oscans))$ THEN inEM=true
IF (inEM EQ true) $
THEN hcte=hcte_per_EM_stage ELSE hcte=hcte_per_NORM_stage
input=LONG(Pipeline[p-1]+deferred)
; output = input from previous pixel allowing for non-perfect CTE

```

```

IF (input NE 0) THEN $
output=LONG(RANDOMN(seed,1,BINOMIAL=[input,hcte],/DOUBLE))$
ELSE output=0L
deferred=input-output
; For those that have transferred, has there been any multiplication?
IF ((inEM EQ true) AND (output NE 0))THEN BEGIN
    dice=RANDOMU(seed,output)
    success=WHERE((dice LE probability_of_gain_per_EM_stage),count)
    output+=count
ENDIF
PipelineTemp[p]=output
ENDFOR
-----
; Add the serial CIC into non-EM regions of the pipeline only
IF (scic_probability_per_transfer NE 0) THEN $
PipelineTemp[0:length_connect+length_image+length_oscans-1]+=$
LONG(RANDOMN(seed,length_connect+length_image+length_oscans,$
POISSON=scic_probability_per_transfer,/DOUBLE))
; Add the EM register CIC
IF (EMcic_probability_per_transfer NE 0) THEN $
PipelineTemp[length_connect+length_image+length_oscans:$
length_EM+length_connect+length_image+length_oscans-1]$+
+=LONG(RANDOMN(seed,length_EM,POISSON=$
EMcic_probability_per_transfer,/DOUBLE))
Pipeline=PipelineTemp
outputimage[x,y]=Pipeline[lengthTotal-1]
PipelineTemp=PipelineTemp*0
; end of serial loop
ENDFOR
; end of parallel loop
ENDFOR
; Account for video amplifier sensitivity in e/ADU
outputimage=outputimage*1.0/VIDsense
; Flip into familiar orientation
;outputimage=REVERSE(outputimage)
; add noise
outputimage+=LONG(ROUND(RANDOMN(seed,imageX,imageY)*(1.0*noise)))
RETURN, outputimage
END

```